

TRANSPORT PROPERTIES IN BILAYER GRAPHENE

BY

HASAN MOHAMMED HASAN ABDULLAH

A Thesis Presented to the
DEANSHIP OF GRADUATE STUDIES

KING FAHD UNIVERSITY OF PETROLEUM & MINERALS

DHAHRAN, SAUDI ARABIA

In Partial Fulfillment of the
Requirements for the Degree of

MASTER OF SCIENCE

In

PHYSICS

APRIL, 2014

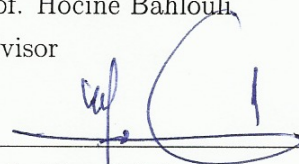
KING FAHD UNIVERSITY OF PETROLEUM & MINERALS
DHAHRAN 31261, SAUDI ARABIA

DEANSHIP OF GRADUATE STUDIES

This thesis, written by **HASAN MOHAMMED HASAN ABDULLAH** under the direction of his thesis advisor and approved by his thesis committee, has been presented to and accepted by the Dean of Graduate Studies, in partial fulfillment of the requirements for the degree of **MASTER OF SCIENCE IN PHYSICS**.



Prof. Hocine Bahlouli
Advisor




Prof. Ahmed Jellal
Member



Prof. Ibraheem Nasser
Member



Dr. Abdul-Aziz Al-Jalal.
Department Chairman



Prof. Salam A. Zummo
Dean of Graduate Studies

13/5/14

Date:



©Hasan Mohammed Hasan Abdullah

2014

This thesis is dedicated to

my mother and uncle Abdulelah who helped me making my
dreams true and my beloved wife who is the source of my
happiness

ACKNOWLEDGEMENTS

I kneel humbly to Almighty Allah (S.W.T) thanking him for giving me the patience and strength to finish this work. Without his help and guidance my efforts may have gone astray. I would like to thank all people who supported and helped me during my MSc research. First of all, my deep and sincere thanks are dedicated to my thesis advisor Prof. Hocine Bahlouli. He was the most important influence on the successful completion of my thesis. I am very thankful to his continued support, motivation, encouragement and constructive suggestions. He pushed me to develop my weakness and exploits my strength. He had greatest professional influence on my development as an independent researcher.

I also would like to express my gratitude and deep thanks to my committee members Prof. Ahmed Jellal, leader of theoretical physics group at Chouaib Doukkali University, El Jadida, Morocco, for his continued assistance, constructive instructions and for supporting me to handle challenging issues and to Prof. Ibraheem Nasser for his guidance, motivation, enthusiasm and for supporting me during all the time of my MSc study and the writing of this thesis.

I would like to use this opportunity to acknowledge Taiz University for supporting me financially during my MSc study and also KFUPM for providing me the opportunity to pursue my graduate study.

My deep appreciation goes also to the Physics Department at KFUPM, represented by the chairman Dr. Abdul-Aziz Al-Jalal for the assistance, support and guidance during My MSc study.

I also would like to acknowledge the material and scientific support of the Saudi Centre for Theoretical Physics (SCPT) for supporting my summer visit to Morocco to attend the graphene summer workshope.

At this point, I would like to express my deep gratitude to Dr. Ben Van Duppen, Antwerp University, Belgium, and Dr. Abderrahim El Mouhafid, Chouaib Doukkali University, El Jadida, Morocco for all useful discussions I had with them during the International Summer Workshop on Bilayer graphene in Morocco 2013.

Special thanks in this regard go to Prof. Mahioub Al-Buhairii, Dr. Sahar Ahmed Amin and Dr. Leila Abdul Jalil, Dr. Adwaa Abdu Ali , Dr Abeer Abdullah, Ms Wdha Awad, Ms Nahlaa and Ms Samar from Physics Department, Taiz University, Yemen for their continued supported during my BSc study.

Furthermore, I would like to thank my colleagues Talal Farhan, Anas Awad,

Rashad Ahmed, Ahmed Abdulgalil, Bashar Qasem and my roommate Fathi Mohammed, for their encouragements and moral support. I am also grateful to all my colleagues at the Physics department for their kindness that made the campus a very friendly working environment for me.

Finally, from the bottom of my heart a gratitude is given to my beloved parents, wife and all members of my family for their love, encouragement, patience, and continued prayers.

Contents

DEDICATION.	i
ACKNOWLEDGEMENTS.	ii
TABLE OF CONTENTS.	v
LIST OF FIGURES.	viii
LIST OF ABBREVIATIONS.	xv
Abstract (English).	xvi
Abstract (Arabic).	xvii
1 INTRODUCTION	1
1.1 Carbon and its Allotropes	5
1.1.1 Diamond	6
1.1.2 Graphite	7

1.1.3	Fullerene	7
1.1.4	Graphene	8
1.2	Fabrication of Graphene	9
1.2.1	Mechanical Exfoliation	9
1.2.2	Chemical Vapor Deposition	11
1.3	Applications of Graphene	14
1.3.1	Gas Sensors	14
1.3.2	LCD and Flexible Screen	15
1.3.3	THz Frequency Amplifiers	16
2	ELECTRONIC PROPERTIES OF GRAPHENE	18
2.1	Electronic Structure of Graphene	18
2.1.1	Tight Binding Model of Single layer Graphene	22
2.1.2	Continuum Approximation and Dirac-Weyl Hamiltonian	28
2.1.3	Effective Mass	30
2.1.4	Chirality and Helicity	31
2.1.5	Klein Tunneling	32
2.2	Bilayer Graphene	33
2.2.1	Tight Binding Model	34
2.2.2	Effective Two Band Hamiltonian	37

2.2.3	Trigonal Warping	40
2.2.4	Electric Field Effect	42
3	CONDUCTANCE AND SHOT NOISE IN GRAPHENE AND ITS BILAYERS	44
3.1	Introduction	44
3.2	Landauer-Büttiker Formula	46
3.3	Single Layer Graphene	47
3.4	Bilayer Graphene	49
4	BAND TUNNELING THROUGH DOUBLE BARRIER IN GRAPHENE BILAYER	55
4.1	Introduction	55
4.2	Theoretical Model	57
4.3	Transmission probabilities and conductance	66
4.4	Two band tunneling ($E < \gamma_1$)	69
4.5	Four band tunneling ($E > \gamma_1$)	77
4.6	Conductance	86
5	CONCLUSION	91
	Bibliography.	94
	Vitae.	107

List of Figures

1.1	Electronic configurations for carbon in the ground and excited states.	6
1.2	Some carbon allotropes: a. diamond; b. graphite; c. lonsdaleite; d-f. fullerenes(C_{60} , C_{540} , C_{70}); g. amorphous carbon; h. carbon nanotube	6
1.3	Graphene as the building block of the other carbon allotropes. . .	8
1.4	A comparison between graphene's superlative thermal, mechanical and electronic properties with other elements	10
1.5	(a) Scotch tap method to put some graphite flakes on the SiO_2 wafer. (b) AFM picture of an exfoliated SLG , BLG and TLG flake on 6H-SiC(0001). (c) Optical microscope picture of graphene residual on a wafer. (d) Golden wires stuck on graphene.	12
1.6	(a) Schematic view of CVD [50]. (b) Single crystal of graphene [47]. (c) Samsung's CVD set-up where the copper foil serves as a substrate. (d) A transparent ultralarge-area graphene film deposited on a polymer substrate, obtained by Samsung's method.	13
1.7	Schematic illustrate sensing gas X diluted in N_2 gas flows over graphene deposited on SiC substrate.	14

1.8	(a) Illustration for how much strong graphene is . (b) Transparency measurements on graphene and its bilayer . (c) Graphene-based touch panel with outstanding flexibility, assembled by Samsung. (d) Samsung's prototype of graphene-based touch screen	15
1.9	(a) Schematic view of a top-gated graphene transistor. (b) The cut-off frequency, at room temperature, of the transistor in (c) which is shown to be 155 GHz . (c) Cross-section TEM picture of a graphene transistor with a gate	17
2.1	Top: $2s, 2p_x$ and $2p_y$ form the sp^2 orbitals with trigonal symmetry in the xy - plane; Bottom: sp^2 and p_z orbitals form σ and π bonds .	20
2.2	(a) A single layer graphene lattice. (b) The first Brillouin zone in the reciprocal lattice.	21
2.3	Energy spectrum of single layer graphene in the first Brillouin zone.	27
2.4	Left: the first Brillouin zone in the reciprocal lattice; right: energy spectrum along the lines connecting the high symmetry points. . .	28
2.5	Energy spectrum of graphene monolayer around one of the Dirac points	30
2.6	Illustration of the Klein tunneling through a potential barrier: (a) Schematic diagram of a single layer graphene spectrum. (b) potential barrier with hight V_0 and width D	33
2.7	Bilayer graphene lattice structure	34
2.8	(a) Energy spectrum of Bilayer graphene in the first BZ along k_y intersecting the two Dirac Points K and K' at the corners and Γ at the center. (b) The low energy spectrum showing the trigonal warping at the Dirac point K . The spectrum in (a) and (b) obtained using Eq. 2.35)	36

2.9	A comparison between the energy spectrum obtained using Eq. 2.35 (Solid) Eq. 2.37 (Dashed). (a) with all hopping parameters $\gamma_1 = 0.381$ eV, $\gamma_3 = 0.38$ eV and $\gamma_4 = 0.14$ eV. (b) with $\gamma_1 = 0.381$ eV, $\gamma_3 = \gamma_4 = 0$ eV.	38
2.10	Left: The energy spectrum obtained from the four band model (Solid) Eq. 2.37 and the effective two band model (Dashed)Eq. 2.44. Right: Showing that trigonal warping cannot be obtained using the effective two band model (Blue dotted) Eq. 2.37. The blue dashed rectangle shows the region where the two band model is valid	40
2.11	Left column: (Top) 3D plot of the low energy spectrum (trigonal warping); (Bottom) eque-energy lines of the trigonal warping. Right column: The same as in the left column but with $\gamma_3 = \gamma_4 = 0$	41
2.12	Left: Energy spectrum of bilayer graphene placed in an electric potential (biased BLG) with $\delta = 0.2 \gamma_1$, blue dotted curves corresponding to the effective two band model, solid and dashed curves account for the four band model with and without $\gamma_{3,4}$, respectively. Right: energy spectrum of SLG with $\delta = \gamma_1 = 0$	43
3.1	Minimum conductivity of grapphene	45
3.2	Conductivity and Fano factor as a function of: (a) Fermi energy for a fixed aspect ratio of the graphene strip ; (b) the aspect ratio of the graphene strip at the Dirac point	48
3.3	Schematic of the electric potential applied to the bilayer graphene strip.	49
3.4	Energy bands and the different transmission probabilities corresponding to the different modes	51
3.5	Different transmission channels in bilayer graphene around the Dirac point ($E = 0$) with $b = 50l$	52

3.6	Density plot of the total transmission through the first mode $T^+ = T_+^+ + T_-^+$ (left) and through the second mode $T^- = T_-^- + T_+^-$ (right)	53
3.7	Total transmission probability as a function of the energy E and the transverse wave vector k_y with $b = 50 l$ and $V_0 = -50 \gamma_1$	53
3.8	(a) Conductivity and (b) Fano facto as a function of Fermi energy with $b = 50 l$ and $V_0 = -50 \gamma_1$	54
4.1	The parameters of a rectangular double barrier structure.	59
4.2	Energy spectrum: (a) in region 1 where $V_1 = V_3 = V_5 = 0$. (b) in region 2 for $\delta_2 = 0.2 \gamma_1$, $U_2 = (0.5, 1.2, 1.8) \gamma_1$ (red, dashed green, dotted blue). (c) in region 4 for $\delta_4 = 0.4 \gamma_1$, $U_4 = (0.8, 1.4, 2) \gamma_1$ (red, dashed green, dotted blue). The dashed horizontal lines in (b) and (c) represent the heights of the barriers U_2 and U_4 , respectively.	62
4.3	Schematic representation of different modes and the associated transmission and reflection probabilities.	63
4.4	Scheme representing the bands inside and outside the barriers for the same interlayer potential difference. (a) asymmetric for $U_2 < U_4$. (b) symmetric for $U_2 = U_4$	64
4.5	Transmission for normal incidence with $b_1 = b_2 = 10 nm$, and $\Delta = 0$ (blue dashed), $\Delta = 5 nm$ (green), $\Delta = 10 nm$ (red). (a) for $U_2 = U_4 = 0.4 \gamma_1$. (b) for $U_2 = 0.4 \gamma_1$ and $U_4 = 0.6 \gamma_1$. (c, d) for the same parameters as in (a, b), respectively, but with $\delta_2 = \delta_4 = 0.2 \gamma_1$	71

- 4.6 Density plot for transmission probability, for $\delta_2 = \delta_4 = 0$, versus: (a) E and ky for $U_2 = U_4 = 0.4 \gamma_1$, and $b_1 = b_2 = \Delta = 10 \text{ nm}$. (b) E and Δ with $ky = 0$ and $b_1 = b_2 = 10 \text{ nm}$. (c) E and ky with $U_2 = 0.4 \gamma_1$, $U_4 = 0.6 \gamma_1$ and $b_1 = b_2 = \Delta = 10 \text{ nm}$. (d) E and Δ with $U_2 = 0.4 \gamma_1$, $U_4 = 0.6 \gamma_1$, $ky = 0$ and $b_1 = b_2 = 10 \text{ nm}$. White and black dashed lines represent the band inside and outside the first barrier, respectively. . . . 72
- 4.7 Density plot for transmission probability, for $\delta_2 = \delta_4 = 0.2 \gamma_1$, versus: (a) E and k_y for $U_2 = U_4 = 0.4 \gamma_1$, and $b_1 = b_2 = \Delta = 10 \text{ nm}$. (b) E and Δ for the same parameters as in (a) but with $k_y = 0$. (c, d) for the same parameters as in (a, b), respectively, but for $U_2 = 0.4 \gamma_1$, $U_4 = 0.6 \gamma_1$. White and black dashed lines represent the band inside and outside the first barrier, respectively. 73
- 4.8 Density plot for transmission at normal incidence for $E = \frac{4}{5} U_2$ and $\delta_2 = \delta_4 = 0$. (a) $U_2 = U_4 = 0.4 \gamma_1$, $b_1 = 5 \text{ nm}$. (b) $U_2 = U_4 = 0.4 \gamma_1$, $\Delta = 3.36 \text{ nm}$. (c) $U_2 = 0.4 \gamma_1$, $U_4 = 0.6 \gamma_1$, $b_1 = 5 \text{ nm}$. (d) $U_2 = 0.4 \gamma_1$, $U_4 = 0.6 \gamma_1$, $\Delta = 4 \text{ nm}$. The dashed white and black lines in the left column represent the values of b_1 and b_2 , respectively, where the resonance occur. . . 75
- 4.9 Density plot for transmission at normal incidence for $E = \frac{4}{5} U_2$ and $\delta_2 = \delta_4 = 0.1 \gamma_1$. (a) $U_2 = U_4 = 0.4 \gamma_1$, $b_1 = 5 \text{ nm}$. (b) $U_2 = U_4 = 0.4 \gamma_1$, $\Delta = 3.7 \text{ nm}$. (c) $U_2 = 0.4 \gamma_1$, $U_4 = 0.6 \gamma_1$, $b_1 = 5 \text{ nm}$. (d) $U_2 = 0.4 \gamma_1$, $U_4 = 0.6 \gamma_1$, $\Delta = 4.3 \text{ nm}$. The dashed white and black lines in the left column represent the values of b_1 and b_2 , respectively, where the resonance occur. . . 76
- 4.10 Density plot for the transmission probability versus (a, b) k_y and the width of the two barriers ($b_1 = b_2 = L$) for $U_2 = U_4 = 0.6 \gamma_1$, $E = \frac{4}{5} U_4$ and $\Delta = 10 \text{ nm}, 15 \text{ nm}$, respectively. (c) k_y and Δ for the same parameters as in (a) and for $b_1 = b_2 = 10 \text{ nm}$. (d) ky and b_2 with $b_1 = 5 \text{ nm}$ and $\Delta = 10 \text{ nm}$ 78

4.11	Density plot for the transmission probability versus: (a, b) k_y and the width of the two barriers ($b_1 = b_2 = L$) for $U_2 = U_4 = 0.6 \gamma_1$, $E = \frac{4}{5} U_4$, $\delta_2 = \delta_4 = 0.1 \gamma_1$ and $\Delta = 10 \text{ nm}, 15 \text{ nm}$, respectively. (c) k_y and the width of the well Δ for the same parameters as in (a) and for $b_1 = b_2 = 10 \text{ nm}$. (d) k_y and b_2 with $b_1 = 5 \text{ nm}$ and $\Delta = 10 \text{ nm}$	79
4.12	Density plot for transmission and reflection probabilities with $U_2 = U_4 = 1.5 \gamma_1$, $b_1 = b_2 = 20 \text{ nm}$ and $\Delta = 10 \text{ nm}$. The dashed white and black lines represent the band inside and outside the barrier, respectively.	81
4.13	Density plot for transmission and reflection probabilities with $U_2 = 1.3 \gamma_1$, $U_4 = 1.5 \gamma_1$, $b_1 = b_2 = 20 \text{ nm}$ and $\Delta = 10 \text{ nm}$. The dashed white and black lines represent the band inside and outside the second barrier, respectively.	83
4.14	Density plot for transmission and reflection probabilities with $U_2 = U_4 = 1.5 \gamma_1$, $\delta_2 = \delta_4 = 0.2 \gamma_1$ and $b_1 = b_2 = \Delta = 10 \text{ nm}$. The dashed white and black lines represent the band inside and outside the second barrier, respectively.	84
4.15	Density plot for transmission and reflection probabilities with $U_2 = 1.3 \gamma_1$, $U_4 = 1.5 \gamma_1$, $\delta_2 = \delta_4 = 0.2 \gamma_1$ and $b_1 = b_2 = \Delta = 10 \text{ nm}$. The dashed white and black lines represent the band inside and outside the second barrier, respectively.	85
4.16	Conductance of the double barrier structure as a function of energy for $b_1 = b_2 = 20 \text{ nm}$. (a) $U_2 = U_4 = 1.5 \gamma_1$, $\Delta = 10 \text{ nm}$ (solid), $\Delta = 5 \text{ nm}$ (dotted) and $\delta_2 = \delta_4 = 0$. (b) $U_2 = U_4 = 1.5 \gamma_1$ and $\delta_2 = \delta_4 = 0.2 \gamma_1$. (c) $U_2 = 1.3 \gamma_1$, $U_4 = 1.5 \gamma_1$, $\Delta = 10 \text{ nm}$ and $\delta_2 = \delta_4 = 0$. (d) $U_2 = 1.3 \gamma_1$, $U_4 = 1.5 \gamma_1$, $\Delta = 10 \text{ nm}$ and $\delta_2 = \delta_4 = 0.2 \gamma_1$	87

4.17	The transmissions coefficients around the Dirac point for ($E = V = 1.5 \gamma_1$) and $b_1 = b_2 = 20 \text{ nm}$. (a) single barrier with $\Delta = 0$. (b) double barrier with $\Delta = 10 \text{ nm}$. (c, d) single and double barrier transmission for the same parameters as in (a, b), respectively, but for ($E = V = 5 \gamma_1$). Where $T = \sum_{s,n=\pm} (T_n^s)$	89
4.18	The conductance of the double barrier as a function of: (a) barriers's height V ($U_2 = U_4 = V$) for $E = 1.5 \gamma_1$, $b_1 = b_2 = 20 \text{ nm}$ and $\Delta = 10 \text{ nm}$. (b) b_2 for $V = 1.5 \gamma_1$, $E = 1.3 \gamma_1$, $b_1 = 20 \text{ nm}$ and $\Delta = 10 \text{ nm}$. (c) Δ for $V = 1.5 \gamma_1$, $E = 1.3 \gamma_1$ and $b_1 = b_2 = 20 \text{ nm}$	90

List of abbreviations

1D	:	one-dimensional
2D	:	two-dimensional
2DEG	:	two- dimensional electron gas
AFM	:	Atomic force microscopy
BLG	:	Bilayer graphene
BZ	:	Brillouin zone
CVD	:	chemical vapor deposition
HOPG	:	Highly ordered pyrolytic graphite
IT	:	Information technology
LCAO	:	Linear combination of atomic orbitals
LCD	:	liquid crystal displays
LLs	:	Landau levels
QHE	:	Quantum Hall effect
SLG	:	Single layer graphene
TB	:	Tight binding
TEM	:	Transmission electron microscopy
TLG	:	Trilayer graphene
TW	:	Trigonal warping

THESIS ABSTRACT

Name: Hasan Mohammed Hasan Abdullah.
Title: Transport Properties in Bilayer Graphene
Degree: MASTER OF SCIENCE.
Major Field: Physics.
Date of Degree: April, 2014.

Graphene is considered as a new promising material for IT-applications and most importantly it might replace silicon in the future. Bilayer graphene is the most important candidate for latter purpose since one can create a gap by applying an external electric field and even tune it. Resonant tunneling diode is one of the electronic devices used in IT-application which can be modelled by a double barrier structure. In this work, we calculate the conductance, transmission and reflection probabilities of electrons across asymmetric and symmetric double barrier in graphene bilayer taking into account the full four band energy spectrum. For energies less than γ_1 , the interlayer coupling, we have one channel for transmission which exhibits resonances, even for incident particles with energies less than the strength of barriers, depending on the double barrier geometry. In contrast, for higher energies, we obtained two propagating modes resulting from four possible ways for transmission. We computed the associated transmission probabilities and their contribution to the conductance and studied the effect of the double barrier geometry.

ملخص الرسالة Abstract (Arabic)

الاسم : حسن محمد حسن عبدالله

عنوان الرسالة : الخصائص الإنتقالية في الجرافين ثنائي الطبقة

الدرجة العلمية : ماجستير

التخصص : فيزياء

تاريخ التخرج : يونيو 2014

تعتبر مادة الجرافين من أهم المواد المكتشفة حديثاً، حيث يمكن أن تستبدل مادة السيليكون بها في المستقبل لاستخدامها في التطبيقات الإلكترونية. يعتبر الجرافين ثنائي الطبقة الأكثر ملائمة لهذا الغرض حيث يمكن تكوين فجوة في طيف الطاقة باستخدام مجال كهربائي. ثنائيات النفق الرنانة هي إحدى القطع الإلكترونية المستخدمة في العديد من التطبيقات التكنولوجية والتي يمكن أن تحاكي نظرياً بحاجزي جهد كهربائيين. قمنا في هذا البحث بدراسة الموصلة الكهربائية واحتمالية نفاذ وانعكاس الإلكترونات خلال حاجزين من الجهود الكهربائية المتماثلة وغير المتماثلة للجرافين ثنائي الطبقة. هناك احتمالية واحدة لنفاذ الإلكترونات عند الطاقات المنخفضة ($E < \gamma_1$) والتي تمتلك رنين حتى عندما تكون طاقة الجسيم الساقط أقل من ارتفاع حاجز الجهد. أما بالنسبة للطاقات العالية ($E > \gamma_1$) يوجد نمطين لإنتشار الموجات وبالتالي هناك أربعة احتمالات مختلفة

لنفاذ الإلكترونات خلال الحاجز الكهربائي. قمنا بحساب هذه الاحتمالات الأربعة لنفاذ الإلكترونات واحتمالات الانعكاس المصاحبة لها، ومن ثم استخدمت هذه الإحتماليات في حساب المواصلة الكهربائية كدالة في طاقة الإلكترونات الساقطة مع توضيح مساهمة كل احتمالية على حدة . كما قمنا بدراسة تأثير أبعاد حاجزي الجهد الكهربائي على هذه المواصلة.

Chapter 1

INTRODUCTION

Science develops constantly and improves our understanding of nature. In the 19th century, thermodynamics and electromagnetics were rapidly developed. However, the beginning of 20th century was the time of the most important achievements in physics when quantum mechanics and relativity were born. In 1928, Paul Dirac initiated the beginning of relativistic quantum mechanics by combining these two theories in one equation to describe particles that move at speeds close to the speed of light in contrast to quantum mechanics.

Until recently the application of the relativistic Dirac equation was limited to high energy physics. However, with the discovery of graphene in 2004, the story of graphene started with graphite, a material known for its use in pencil fabrication, in 1947 when P. R. Wallace was trying to theoret-

ically study the band structure of 3D graphite to understand the electronic properties of 3D graphite [1–3]. Later on, Semenoff [4] studied a graphene in a magnetic field as an analog of $(2 + 1)$ dimensional electrodynamics, the purpose was to describe anomaly in such system and he obtained the Landau level of this system at the Dirac point which is responsible for the anomalous integer quantum Hall effect that has been realized experimentally using graphene [5, 6]. In the '80s, many studies also investigated the possibility of a relativistic analog with graphene as a condensed matter system [7, 8].

The theoretical work concerning graphene was boosted again in the 90th by the discovery of carbon nanotubes [9]. During the last four decades of the last century, there were many experimental investigations on graphene and its fabrication. For example, free standing graphene [10], epitaxial graphene grown on metal [11–13] and intercalation of graphene [14] procedure well used experimentally. But due to thermal fluctuations, everyone was convinced that two dimensional crystals cannot exist. However, in the early days of the 20th century two scientific papers stated that graphene not only can be fabricated but also one can access its electronic properties using graphene flakes [15, 16]. This made graphene play a leading role similar to that of nanotubes, whose electronic properties were already considered outstanding. Then in 2004, a group of scientists in Manchester University, led by A. Geim and K. Novoselov, succeeded in producing a stable single layer of carbon atoms (Graphene) [17, 18]. In 2010, the Nobel Prize in Physics awarded jointly to A. Geim and K. Novoselov. *for their discovery of Graphene*.

In such material, carbon atoms are packed in a two-dimensional

hexagonal lattice connected to each other by covalent bonds. In the last few years, graphene has risen in the horizon as a new star in the condensed matter field as a result of its peculiar properties. Now, we will briefly go through some of them starting from single layer and then to bilayer graphene for in-depth reviews see [19–23]. Single layer graphene is the thinnest layer of graphite, with one atom thick, and therefor constitutes a perfect two dimensional (**2D**) crystal. This allowed researchers to investigate its charge carriers, which acts as two dimensional electron gas (**2DEG**) with a relativistic massless fermions. Apart from being the thinnest material, single layer graphene has a lot of interesting properties. For example, its mechanical robustness makes it a very strong material on the micro-scale, and a single graphene sheet is nearly considered impenetrable for gas molecules [24, 25].

Moreover, single layer graphene has attractive electronic properties useful for IT-applications, such as large mobility of its charge carriers, low optical absorption, gapless energy spectrum (and linear at low energies) and in contrast to the nanotubes, graphene has no backscattering of electrons and compared to the latter, it has a large contact region which makes it easier to build electrical contacts, this is very important for potential device applications.

Furthermore, electrons in graphene behave as massless relativistic fermions only at low energies. However, it is still possible to test many fundamental relativistic theories, such as Klein paradox. One of the most important discoveries in solid state is the quantum Hall effect (**QHE**) in 2D system [26] it turns out that graphene is the only material in which **QHE** is

realized even at room temperature [27].

Bilayer graphene, which is composed of two graphene layers on top of each other, also received a lot of attention due to its importance in applications. As for single layer graphene, the energy spectrum of bilayer graphene is gapless and quadratic at low energy and is completely different from any **2DEG** system. Latter on, scientists were able to open a band gap , and even tune it, in the energy spectrum of bilayer graphene by applying an external electric field on the two layers [28, 29]. In the single layer graphene, this is rather difficult due to the Klein tunneling.

In IT-applications, obtaining a band gap is essential to realize digital transistors. Another interesting phenomena is that zero field conductivity of single and bilayer graphene does not vanish in the limit of zero charge carriers, instead they have a minimum conductivity close to the conductivity quantum $\frac{e^2}{h}$ [18, 30]. Shot noise and conductance of single and bilayer graphene have been investigated theoretically many years ago for single and multiple electrostatic barriers with different shapes [31, 32]. In bilayer graphene those studies were restricted to energies and potential strength less than the inter-layer coupling γ_1 [33, 34].

In this work, we investigate the tunneling, shot noise and conductance through asymmetric double barrier structure. Through this chapter, we briefly review the carbon structure and its allotropes and how one can fabricate graphene, then, some applications of graphene are explored. In chapter 2, the theoretical background of tight binding of the single graphene and its continuum limit is explained. Furthermore, the special band struc-

ture due to the spacial symmetries in graphene are demonstrated. Next, we display the four band and two (effective) band Hamiltonian for bilayer graphene and implement them to show the band structure in the presence of an external electric field. In chapter 3 we will go through ballistic transmission and compute shot noise in graphene and its bilayer. In chapter 4 we present the theoretical model used in our calculation, then we will show our results with the discussion and compare these results with previous published work and point out the relevance of our findings to a systematic study of the transport properties in double barrier structures. We then conclude with chapter 5 by summarizing our finding and the possible future work.

1.1 Carbon and its Allotropes

One of the most common elements on the earth is carbon, it is found everywhere: our foods, clothes, cosmetics, gasoline,...etc. Its name "*Carbon*" comes from the Latin word *carbo* for *coal* and *charcoal*. What makes carbon an important element is its strong and stable bonds that can resist in difficult ambient conditions. It belongs to group fourteen on the periodic table. Its covalent bond has four electrons with two possible configurations: ground and excited state configuration $1s^2, 2s^2 \quad 2p^2$ as shown in Fig. 1.1 [35]. Generally, carbon is found in multi-atomic structure with different molecular configurations called allotropes. Such as: diamond, graphite and fullerenes as shown in Fig. 1.2 [Ref. Wikipedia].

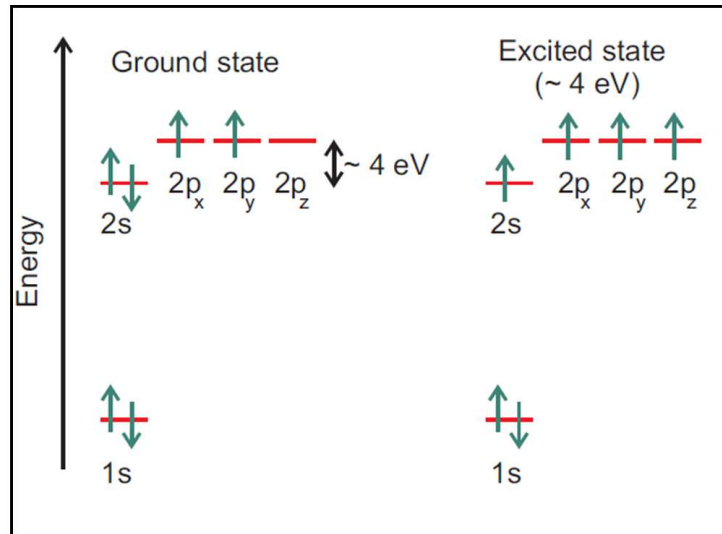


Figure 1.1: Electronic configurations for carbon in the ground and excited states.

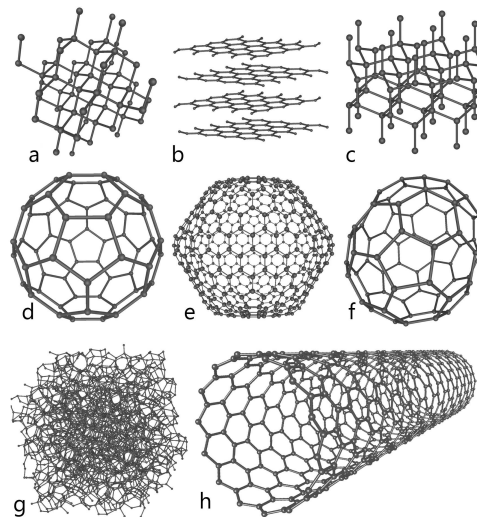


Figure 1.2: Some carbon allotropes: a. diamond; b. graphite; c. lonsdaleite; d-f. fullerenes(*C*₆₀, *C*₅₄₀, *C*₇₀); g. amorphous carbon; h. carbon nanotube

1.1.1 Diamond

The most famous allotrope of carbon is diamond. It has a faced center cubic structure; each carbon atom is bounded to four other neighbor atoms in

a tetrahedron arrangement which is responsible for many properties of diamond. It has a low electrical conductivity whereas its thermal conductivity is the highest, but due to its large band gap, it is considered an excellent insulator. Moreover, it is one of the hardest materials which makes it a good tool to be used in industrial drilling, cutting, and polishing.

1.1.2 Graphite

Graphite, one of the most common allotropes of carbon, build out of many stacked layers of carbon atoms; each one is bounded to three other atoms with strong covalent bonds forming a hexagonal lattice whereas the atoms in two adjacent layers are weakly bounded by van der Waals force, this form is used in pencils. A single layer of graphite is called graphene [36]. Among carbon allotropes, it is the most stable and unlike diamond, graphite is a very good conductor and it can be transformed into diamond at temperature well above 1700 K and at pressures in excess of 12 GPa [37].

1.1.3 Fullerene

Any molecules build up of carbon atoms in different forms, such as ellipsoid, hallow sphere (Spherical and cylindrical fullerenes are called buckyballs and carbon nanotube, respectively), or tube are called fullerenes. It has been discovered by researchers at Rice University in 1985. Regarding its structure,

it is similar to graphite but it may have pentagonal or heptagonal rings. In 1996, the Nobel Prize in Chemistry was awarded jointly to Robert F, Sir Harold, and Richard E. *for their discovery of fullerenes*.

1.1.4 Graphene

Among the carbon allotropes: diamond, graphite and fullerenes, graphene is considered as the building block for the previous allotropes, see Fig. 1.3 [38]. Graphene is a two dimensional one-atom layer of carbon atoms thick. Its

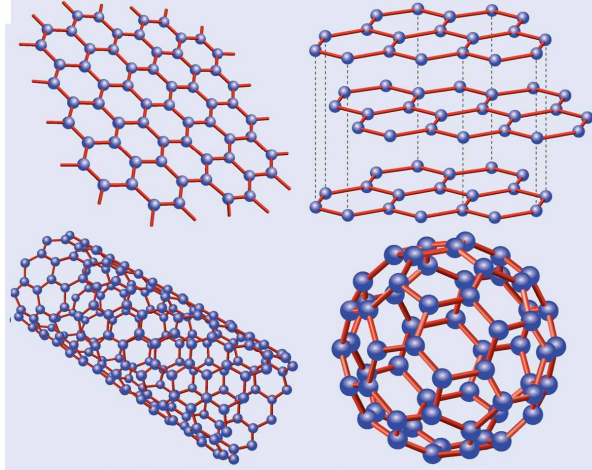


Figure 1.3: Graphene as the building block of the other carbon allotropes.

structure is hexagonal (honeycomb) arrangement of sp^2 - bounded carbon atoms [18]. Its exceptional, electronic, optical, thermal, and mechanical, properties have potential of applications. Consequently, it becomes a hot research topic in these days. For example, its thermal conductivity is 15 times larger than that of copper and its electron mobility is about 20 times larger

than that of GaAs. In addition, it is considered as one of the strongest materials with a Young's modulus of about 1 TPa, and about 200 times stronger than structural steel [39]. A comparison between mechanical, electronic and thermal properties of graphene and other elements is shown in Fig. 1.4 [39]. Next we will give a brief overview on the fabrication of graphene.

1.2 Fabrication of Graphene

graphene has been studied theoretically for decades, but it has not been realized in labs till 2004, because it was considered that two dimensional crystals cannot exist due to the thermal fluctuation. Surprisingly, the method used for the first time to isolate single layer graphite was simple, the Manchester group used mechanical exfoliation or, simply, the Scotch tape technique. Now, many methods have been attempted to fabricate graphene such as confinement controlled sublimation (epitaxial graphene) [40], chemical reduction of graphene oxide [41], and chemical vapor deposition (**CVD**) on transition metal substrates [42–44]. Here, we briefly present some of these techniques.

1.2.1 Mechanical Exfoliation

Mechanical exfoliation is the oldest method used to produce graphene in the famous experiment at the University of Manchester. In this method one

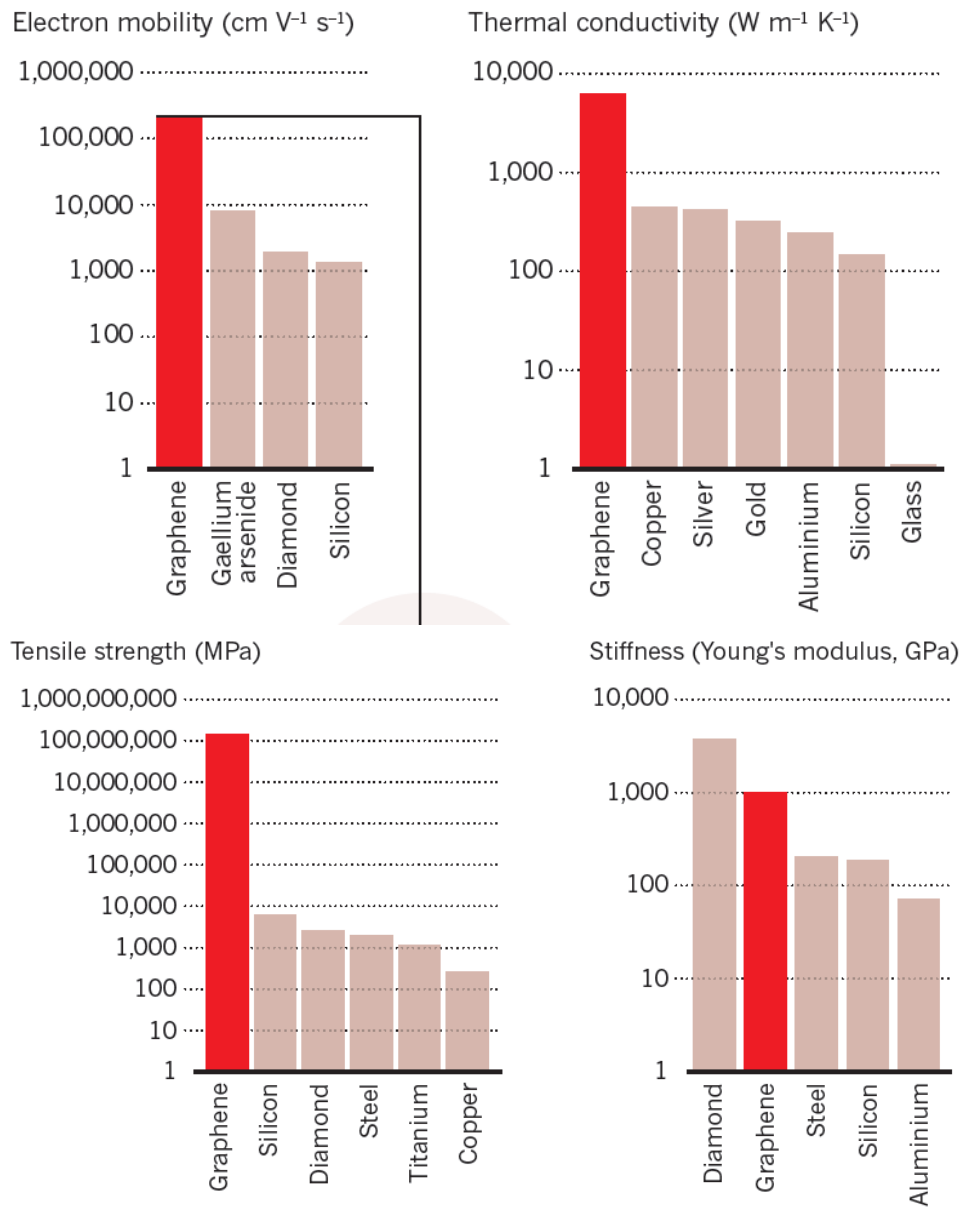


Figure 1.4: A comparison between graphene's superlative thermal, mechanical and electronic properties with other elements

starts with a thin graphite sample of a highly ordered pyrolytic graphite (**HOPG**), then ripping off layers of graphite using scotch tape, finally press-

ing the tape on a Si/SiO_2 substrate with a thickness of 300 nm to deposit the graphene samples. This means that one first puts the graphite sample on a piece of adhesive tape and by folding the tape repeatedly one splits the flake into many thinner flakes. Between these flakes there will occasionally be some single-layer microscopic parts. In Fig. 1.5 [45,46] we show the steps of this process. Now, we have layers of different thickness on the substrate which gives rise to a different reflection intensity, due to the interference between the layers and the graphene sample one can guess which regions are likely to consist of single, bilayer, or trilayer graphene using optical microscope. Furthermore, the results from the optical microscope observation can be verified using other methods such as Raman spectroscopy, atomic force microscopic Fig 1.5 (b), etc. This method is easy to implement, yields high-purity and high-quality graphene, and is rather inexpensive. However, it is impossible to use for mass production, unlike the other methods, and the size of the samples obtained from this method is limited, typically never larger than $100 \times 100 \mu m$, which is not suitable for industrial production.

1.2.2 Chemical Vapor Deposition

The chemical vapor deposition (**CVD**) technique is considered as a promising technique for graphene syntheses. In the past, experimentalists succeed in depositing a single-layer graphene, they did it by growing graphene by **CVD** of CH_4 molecules over large areas on copper substrates [47–49]. The idea

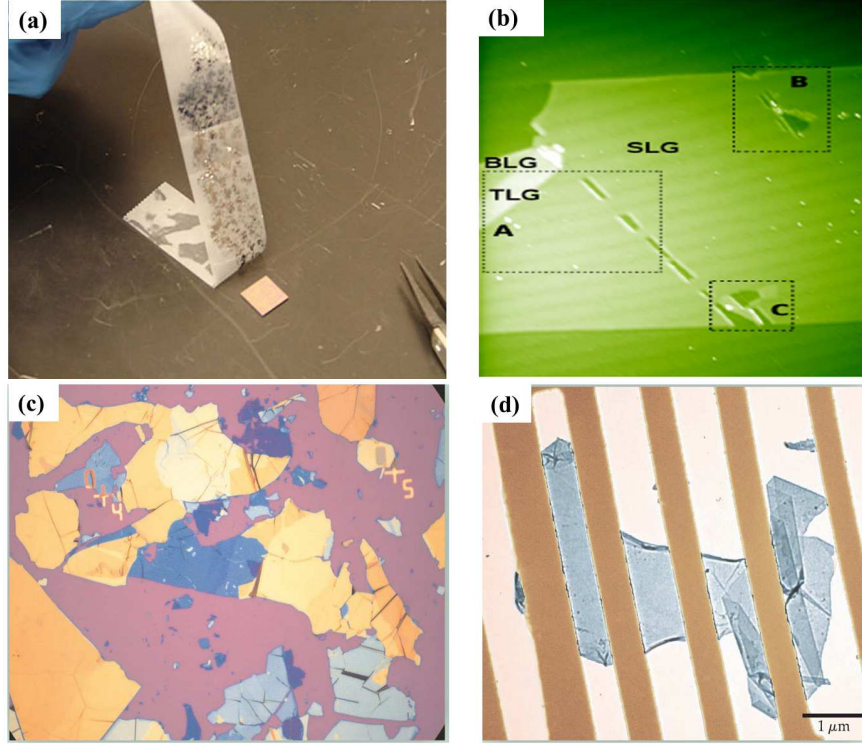


Figure 1.5: (a) Scotch tap method to put some graphite flakes on the SiO_2 wafer. (b) **AFM** picture of an exfoliated **SLG**, **BLG** and **TLG** flake on 6H-SiC(0001). (c) Optical microscope picture of graphene residual on a wafer. (d) Golden wires stuck on graphene.

behind this method is depicted in Fig.1.6 (a) [51], where a metal (Cu) and nonmetal (amorphous SiO_2/Si) substrate is used with remotely provided Cu vapor during the **CVD** process [50]. The copper substrate is put into a furnace under low vacuum and heated to around 1000 °C, hydrogen and methane gases then flow through the furnace. The hydrogen gas helps catalyzing the reaction between the surface of the substrate and methane, decomposing the latter in two H_2 and C-atom. Carbon atoms can easily move around because it is weakly bounded to the surface, thereby each carbon atom finds other

carbon atoms and attaches itself to them via covalent bonds.

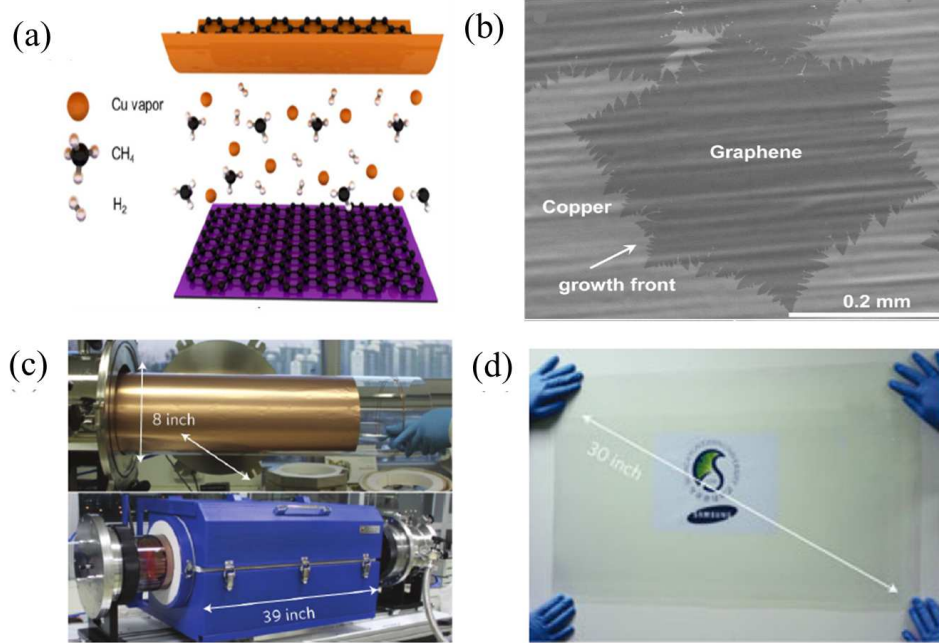


Figure 1.6: (a) Schematic view of **CVD** [50]. (b) Single crystal of graphene [47]. (c) Samsung's **CVD** set-up where the copper foil serves as a substrate. (d) A transparent ultralarge-area graphene film deposited on a polymer substrate, obtained by Samsung's method.

One of the advantages of **CVD** method is producing large single layer graphene sheet in contrast to micron size flakes from the mechanical exfoliation, see Fig. 1.6 (b), although during the process defects and grain boundaries are formed leading to lower mobility. Recently, Samsung used this method to fabricate large single graphene sheet of the order of meter in size, see Fig. 1.6 (c,d).

1.3 Applications of Graphene

1.3.1 Gas Sensors

For any detection methods, the most important goal is to achieve a high sensitivity level such that individual quanta, which is in the case of gas sensors are atoms or molecules, can be resolved. So far, such a resolution is beyond the ability of any detection method, including solid-state gas sensors. This limitation in solid-state gas sensors is attributed to the fluctuation due to defects and thermal motion of charges [52] resulting in intrinsic noise exceeding the signal from individual molecules, by several orders of magnitudes. In 2007 Ref [53] showed that when a gas molecule attaches to or detaches from graphene surface, electronic properties of graphene is affected in a measurable way. A typical sensor device layout is depicted in Fig. 1.7 [54].

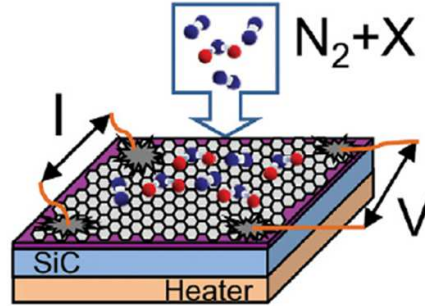


Figure 1.7: Schematic illustrate sensing gas X diluted in N_2 gas flows over garphene deposited on SiC substrate.

This means that individual molecule can be detected using micrometer-size graphene sensor since it can change the local carrier concentration in graphene resulting in step like changes in the resistance. The secret behind this high sensitivity is due to the fact that graphene is electronically an exceptional low-noise material, thereby it is considered a promising candidate for chemical detectors.

1.3.2 LCD and Flexible Screen

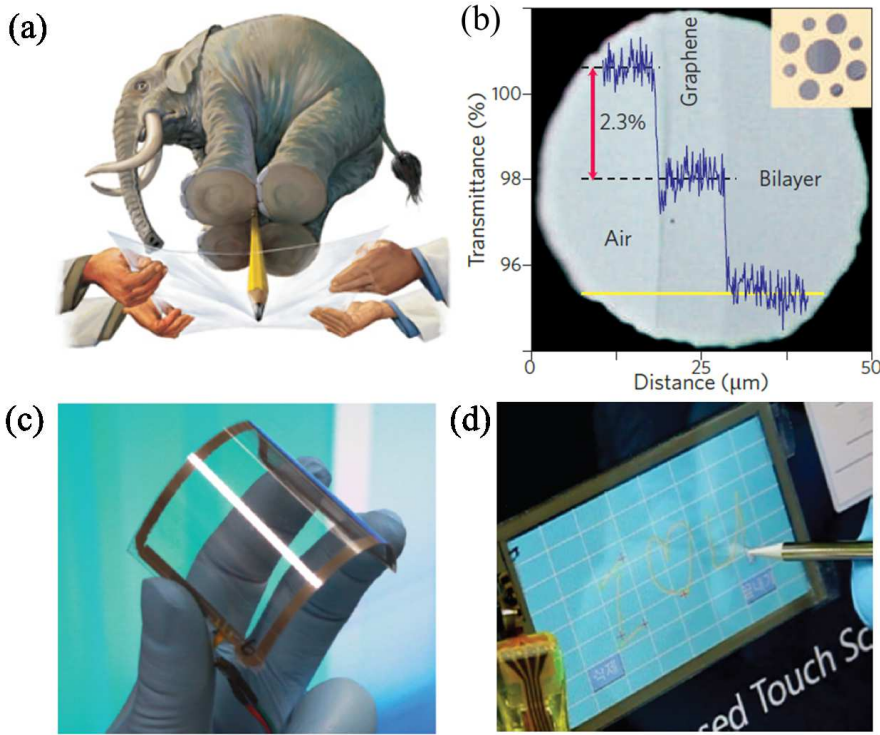


Figure 1.8: (a) Illustration for how much strong graphene is . (b) Transparency measurements on graphene and its bilayer . (c) Graphene-based touch panel with outstanding flexibility, assembled by Samsung. (d) Samsung's prototype of graphene-based touch screen

In 2010, Bonaccorso showed that graphene can be used as a very thin transparent electrode in optoelectronic and electronic devices [56]. Transparent electrodes play a crucial role as an essential element of many devices, such as light-emitting diodes, cellular phones, touch screen, and most importantly liquid crystal displays (**LCD**) [57]. What makes graphene an ideal candidate for transparent electrodes is its unique properties, such as atomic layer thickness, high chemical stability, mechanical strength Fig. 1.8 (a) [55], high charge mobility, low resistance, and most importantly high optical transparency. It absorbs 2.3% over a very large range of wavelengths, see Fig. 1.8 (b) [56]. In addition, adding only one percent of graphene to plastic makes it conductor while it remains transparent. Nowadays, the electronic devices are based on thin metal oxide films with Indium (Indium Tin Oxide). But Indium has many disadvantages, such as being expensive, toxic, brittle, and its supply is expected to finish in the next few years. Hence, graphene is promising candidate to replace old films, resulting in the fabrication of flexible **LCDs**, pure light emitting diodes and touch screens, see Fig. 1.8 (c,d) [51]. For more details, see Ref. [58].

1.3.3 THz Frequency Amplifiers

Recently, many companies, such as IBM and Nokia have put a lot of efforts in building graphene Field Effect Transistor (**FET**) as shown in Fig. 1.9 [59], see [60–64] for a review. The high quality ballistic transport in graphene is

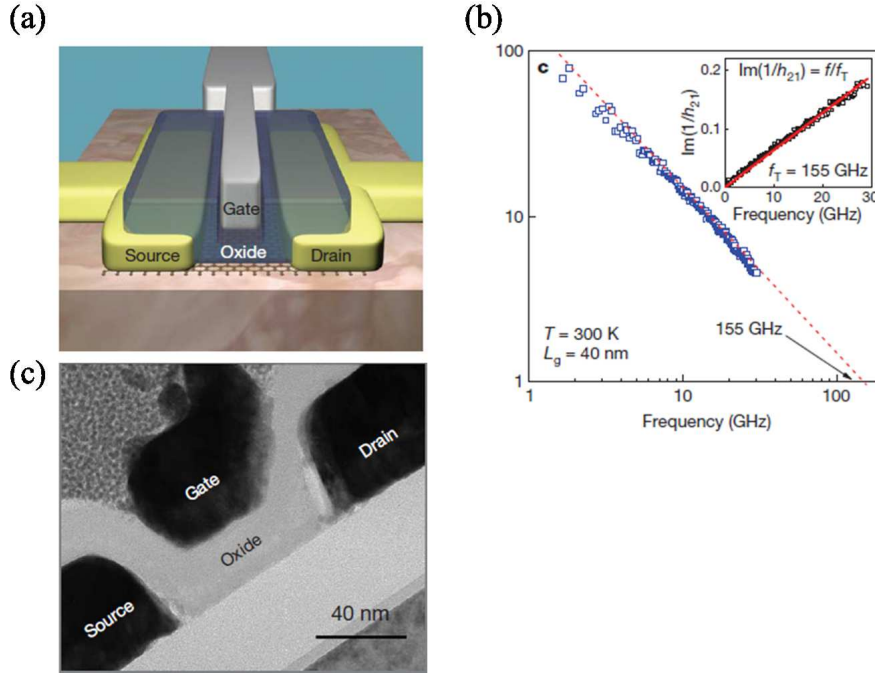


Figure 1.9: (a) Schematic view of a top-gated graphene transistor. (b) The cut-off frequency, at room temperature, of the transistor in (c) which is shown to be **155 GHz**. (c) Cross-section **TEM** picture of a graphene transistor with a gate .

the main driving force to fabricate transistors, since it allows to fabricate electronic devices without any heating problems. Furthermore, in contrast to carbon nanotubes (CNTs) graphene **2D** nature allows a large area of contact, leading to reduction in contact-resistance problems. Due to Klein tunneling, the realization of the new transistor made from graphene face a problem with an sufficient on/off ratio. However, this problem is less important for high frequency applications, such as frequency amplifiers [65] and transmitters [61] which have been already fabricated [66,67].

Chapter 2

ELECTRONIC PROPERTIES OF GRAPHENE

2.1 Electronic Structure of Graphene

The peculiar band structure of graphene is related to the hexagonal lattice which consists of carbon atoms. Each unit cell has two different atoms denoted by A and B (Note: both of them are carbon atoms but it means that we need two carbon atoms at different sites (A, B) in the unit cell to construct the Bravais lattice). Each atom has six electrons ordered in the $1s^2, 2s^2$ and $2p^2$ orbitals. These orbitals, of different atoms, are contributing to make bonds, like σ and π bonds, see Fig 2.1 [68]. σ is a three directional bond which is necessary to for a hexagonal lattice, in this bond every atom in

the unit cell participates with three orbitals $2s, 2p_x$ and $2p_y$ in the bonding, which is called sp^2 hybridization.

Thus, there are six orbitals in each unit cell yielding six bands, three of which appear in the valance band called σ , and the other three in the conduction band being referred to as σ^* . The σ bands have a filled shell which makes its contribution to the transport properties negligible, however, it is responsible for the robustness of the lattice. The last $2p_z$ orbitals form the π bonds in the lattice. In contrast to the σ bond, π bond has a half-filled shell and is weaker than σ bond, hence, the π bonds are important for the electronic behavior near the Fermi energy, where conduction or transport of electrons take place. Since we are interested in the transport properties we will concentrate on the π bands and ignore the other ones.

As we mentioned earlier, graphene has triangular Bravais lattice with two atoms in the unit cell denoted as A and B atoms, see Fig.2.2(a). The unit cell in graphene has the following lattice vectors:

$$a_1 = \frac{a}{2} \left(\sqrt{3}, 3 \right), \quad a_2 = \frac{a}{2} \left(\sqrt{3}, -3 \right) \quad (2.1)$$

with $a = 0.142 \text{ nm}$ is the carbon-carbon atom distance (*i.e.* between two neighbors atoms), which is different from the lattice constant (distance between the same atoms, either A or B atoms), which is given by $\sqrt{3}a$. These two vectors can be used to generate the positions of the A atoms in the lattice by $P_A = n_1 a_1 + n_2 a_2$ and for the B atoms by $P_B = m_1 a_1 + m_2 a_2 + \delta_1$, where

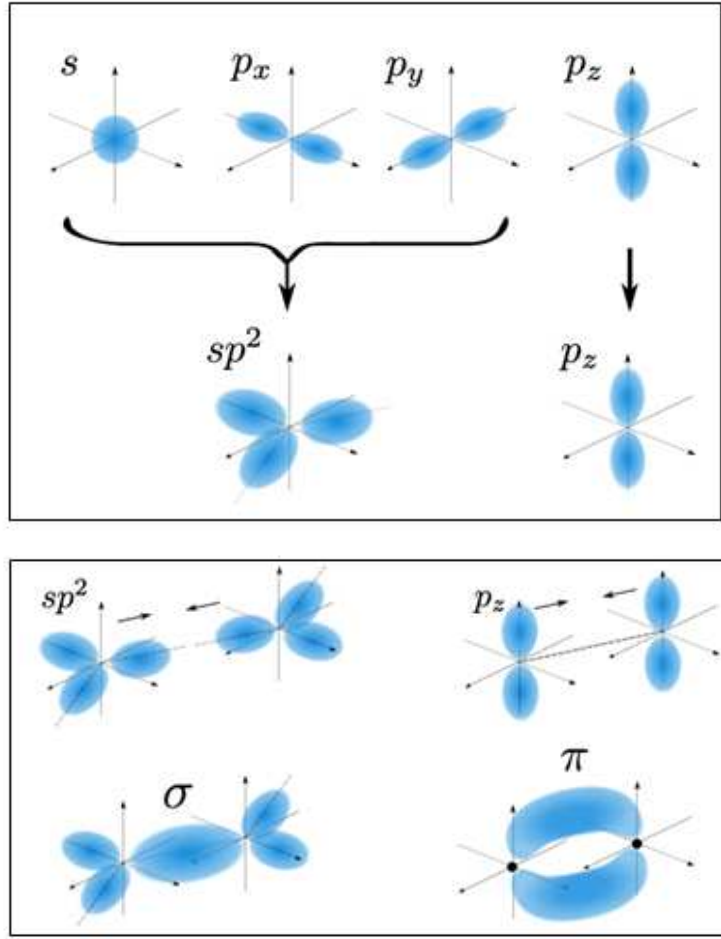


Figure 2.1: Top: $2s$, $2p_x$ and $2p_y$ form the sp^2 orbitals with trigonal symmetry in the xy - plane; Bottom: sp^2 and p_z orbitals form σ and π bonds .

n_i and m_j are integers and.

$$\delta_1 = \frac{a}{2} \left(1, \sqrt{3} \right), \quad \delta_2 = \frac{a}{2} \left(1, -\sqrt{3} \right), \quad \delta_3 = \frac{a}{2} (-2, 0) \quad (2.2)$$

The corresponding reciprocal lattice in the momentum (\mathbf{k}) space, see Fig.2.2(b), has lattice vectors

$$b_1 = \frac{2\pi}{3\sqrt{3}a} (\sqrt{3}, 3), \quad b_2 = \frac{2\pi}{3\sqrt{3}a} (\sqrt{3}, -3) \quad (2.3)$$

Like the Bravais lattice in the real space, the reciprocal lattice in the mo-

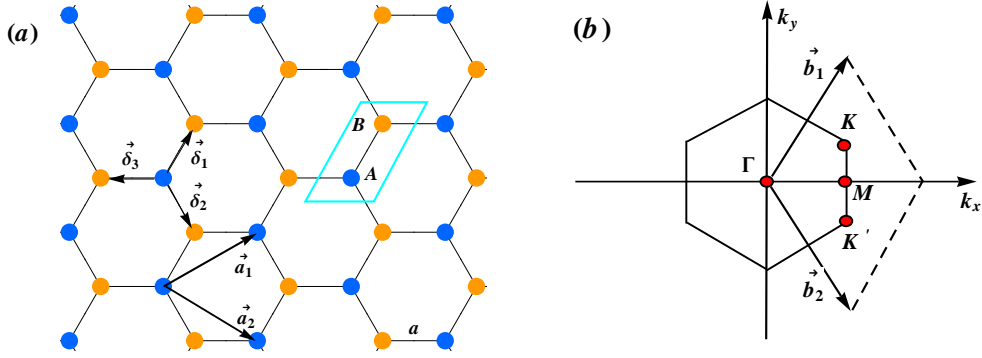


Figure 2.2: (a) A single layer graphene lattice. (b) The first Brillouin zone in the reciprocal lattice.

mentum space has trigonal structure and a hexagonal Brillouin zone (**BZ**). The four red points Γ , M , K and K' in the first **BZ** Fig.2.2(b) are called the points of high symmetry. The K and K' are called Dirac points. Now, we will employ the tight binding model (**TB**) to describe the band structure of graphene. Then, with the continuum approximation we will obtain the **TB** Hamiltonian which reduces to the Dirac-Weyl Hamiltonian.

2.1.1 Tight Binding Model of Single layer Graphene

Tight-binding model is used to study the band structure of solids where the electrons are strongly bounded to the atoms (localized electrons). The idea is to write down the wave function as a linear combination of the atomic orbitals ϕ_i , the so-called (**LCAO**) approximation [69, 70].

$$\Psi(\mathbf{r}) = \sum_i c_i \phi_i \quad (2.4)$$

where the sum runs over all orbitals in the crystal. Since π bond is the only important one as mentioned above, only one orbital wave function must be considered per atom. Furthermore, for a the hexagonal lattice of graphene, where the unit cell contains two atoms, the solution of the total wave function is a Bloch function which reads:

$$\Psi_k(\mathbf{r}) = C_A \Phi_k^A + C_B \Phi_k^B \quad (2.5)$$

Where

$$\Phi_k^j(r) = \frac{1}{\sqrt{N}} \sum_{n=1}^N e^{ik \cdot R_n^j} \phi(r - R_n^j), \quad j = A, B \quad (2.6)$$

are the Bloch functions which obey the Bloch theorem:

$$\Phi_k^j(r + R) = e^{ik \cdot R} \Phi_k^j(r) \quad (2.7)$$

and N is the number of unit cells in the crystal. Then, the expectation value for the energy is

$$\langle E \rangle = \frac{\int \Psi_k^*(r) H \Psi_k(r) dr}{\int \Psi_k^*(r) \Psi_k(r) dr} = \frac{\sum_{ij} C_i^* C_j H_{ij}}{\sum_{ij} C_i^* C_j S_{ij}} \quad (2.8)$$

Minimizing the energy (variational approach)¹ using $\frac{\partial E}{\partial C_i^*} = 0$, we obtain the secular equation as,

$$\sum_j H_{ij} C_j = E \sum_j S_{ij} C_j, \quad \forall i \quad (2.9)$$

where H_{ij} , S_{ij} are the transfer and overlap matrices which defined by:

$$H_{ij} = \int \Phi_k^{i*}(r) H \Phi_k^j(r) dr = \langle \Phi_k^i | H | \Phi_k^j \rangle \quad (2.10)$$

$$S_{ij} = \int \Phi_k^{i*}(r) \Phi_k^j(r) dr = \langle \Phi_k^i | \Phi_k^j \rangle \quad (2.11)$$

Eq. 2.9 is a system of equations which can be written as a general eigenvalue equation $HC = ESC$ or:

$$\begin{pmatrix} H_{AA} & H_{AB} \\ H_{BA} & H_{BB} \end{pmatrix} \begin{pmatrix} C_A \\ C_B \end{pmatrix} = E \begin{pmatrix} S_{AA} & S_{AB} \\ S_{BA} & S_{BB} \end{pmatrix} \begin{pmatrix} C_A \\ C_B \end{pmatrix} \quad (2.12)$$

¹Note: this variational approach is equivalent to the Schrodinger equation $H|\Psi_k\rangle = E|\Psi_k\rangle$, $|\Psi_k\rangle = \sum_i C_i |\Phi_k^i\rangle$ and by multiplying both sides by $\langle \Phi_k^j |$ leads to $\sum_i C_i \langle \Phi_k^j | H | \Phi_k^i \rangle = E \sum_i C_i \langle \Phi_k^j | \Phi_k^i \rangle$

the components of these matrices can be found as follows:

$$\begin{aligned}
H_{AA} &= \int (\Phi_k^A)^* H \Phi_k^A(r) dr \\
&= \frac{1}{N} \int \left(\sum_{n'=1}^N e^{-ik \cdot R_{n'}^A} \phi(r - R_{n'}^A) \right) \left(H \sum_{n=1}^N e^{ik \cdot R_n^A} \phi(r - R_n^A) \right) dr \\
&= \frac{1}{N} \sum_{n'=1}^N \sum_{n=1}^N \int (\phi(r - R_{n'}^A) H \phi(r - R_n^A)) dr \\
&= \begin{cases} 0, n \neq n' \\ \varepsilon_0, n = n' \end{cases}
\end{aligned} \tag{2.13}$$

Since $H\phi(r - R_n^A) = E\phi(r - R_n^A)$ is independent of the cell number. ε_0 is the on-site energy of the A atoms. The last integral is zero for $n \neq n'$ which means there is no hopping between A atoms in different unit cells. Similarly for the component H_{BB} . On the other hand

$$\begin{aligned}
H_{AB} &= \int (\Phi_k^A)^*(r) H \Phi_k^B(r) dr \\
&= \frac{1}{N} \int \left(\sum_{n'=1}^N e^{-ik \cdot R_{n'}^A} \phi(r - R_{n'}^A) \right) \left(H \sum_{n=1}^N e^{ik \cdot R_n^B} \phi(r - R_n^B) \right) dr \\
&= \frac{1}{N} \sum_{n'=1}^N \sum_{n=1}^N e^{ik \cdot (R_n^B - R_{n'}^A)} \int (\phi(r - R_{n'}^A) H \phi(r - R_n^B)) dr \\
&= \gamma_0 f(k)
\end{aligned} \tag{2.14}$$

where the sum in n runs over all B atoms in the crystal ²(i.e. over all the unit cells) and taking into account the nearest neighbor interaction, the sum in n'

$${}^2 \sum_{n=1}^N \sum_{n'=1}^N = \sum_{n=1}^N \sum_{<n'>}^3 = N \sum_{<n'>}^3$$

runs over the three nearest neighbor atoms to the atom B in each unit cell ($n' = 1, 2, 3$) as depicted in Fig 2.2(a). The coupling between first nearest neighbors γ_0 , which assumed to be the same for any two nearest neighbors. The geometrical factor $f(k)$ and γ_1 are defined as:

$$\gamma_0 = \int (\phi(r - R_n^A) H \phi(r - R_n^B)) dr \quad (2.15)$$

$$f(k) = \sum_{n'=1}^3 e^{ik \cdot \delta_{n'}} \quad (2.16)$$

where, $\delta_{n'} = (R_n^B - R_n^A)$. repeating the same steps above, we find

$$H_{BA} = H_{AB}^* = \gamma_0 f^*(k) \quad (2.17)$$

Similarly, the overlap matrix has the elements:

$$S_{BA} = S_{AB}^* = s f^*(k), \quad S_{AA} = S_{BB} = 1 \quad (2.18)$$

where $s = \int (\phi(r - R_n^A) \phi(r - R_n^B)) dr$ is the overlap integral . Hence, the eigenvalue equation in Eq.2.12 becomes

$$\begin{pmatrix} \varepsilon_0 & \gamma_0 f(k) \\ \gamma_0 f^*(k) & \varepsilon_0 \end{pmatrix} \begin{pmatrix} C_A \\ C_B \end{pmatrix} = E \begin{pmatrix} 1 & s f \\ s f^* & 1 \end{pmatrix} \begin{pmatrix} C_A \\ C_B \end{pmatrix} \quad (2.19)$$

to find a solution to this equation the energy should satisfy $\det[H - Es] = 0$ which leads to

$$\begin{vmatrix} \varepsilon_0 - E & (\gamma_0 - Es)f \\ (\gamma_0 - Es)f^* & \varepsilon_0 - E \end{vmatrix} = 0 \Rightarrow (\varepsilon_0 - E)^2 = (\gamma_0 - Es)^2 |f(k)|^2 \quad (2.20)$$

and this gives

$$E_{\pm} = \frac{\varepsilon_0 \pm \gamma_0 |f(k)|}{1 \pm s |f(k)|} \quad (2.21)$$

where $\gamma_0 \approx 0.3eV$ and $s = 0.38$ [71]. with

$$\begin{aligned} f(k) &= \sum_{j=1,2,3} e^{ik \cdot \delta_j} \\ &= - [e^{ik \cdot \delta_1} + e^{ik \cdot \delta_2} + e^{ik \cdot \delta_3}] \\ &= - \left[e^{i \frac{a}{2} (k_x + \sqrt{3} k_y)} + e^{i \frac{a}{2} (k_x - \sqrt{3} k_y)} + e^{i a k_x} \right] \\ &= - e^{i \frac{a}{2} k_x} \left[2 \cos\left(\frac{\sqrt{3}}{2} a k_y\right) + e^{-3i \frac{a}{2} k_x} \right] \end{aligned} \quad (2.22)$$

where, $\delta_1 = \frac{a}{2}(1, \sqrt{3})$, $\delta_2 = \frac{a}{2}(1, -\sqrt{3})$ and $\delta_3 = \frac{a}{2}(-2, 0)$ then,

$$|f(k)| = \sqrt{\left[4 \cos^2\left(\frac{\sqrt{3}}{2} a k_y\right) + 1 + 4 \cos\left(\frac{\sqrt{3}}{2} a k_y\right) \cos\left(\frac{3}{2} a k_y\right) \right]} \quad (2.23)$$

Since ε_0 causes a shift in the energy spectrum, we can put it zero without affect the physics, and because the influence of s is small around the Dirac points, which is the region we are interested in, we can neglect it then the

energy becomes

$$E_{\pm} = \pm\gamma_0|f(k)| \quad (2.24)$$

which is shown in Fig.2.3. Remember this spectrum is in the first Brillouin zone in the reciprocal lattice, the red hexagonal shape at zero energy in Fig.2.3. In Fig.2.4 we show the first Brillouin zone of the honeycomb lattice

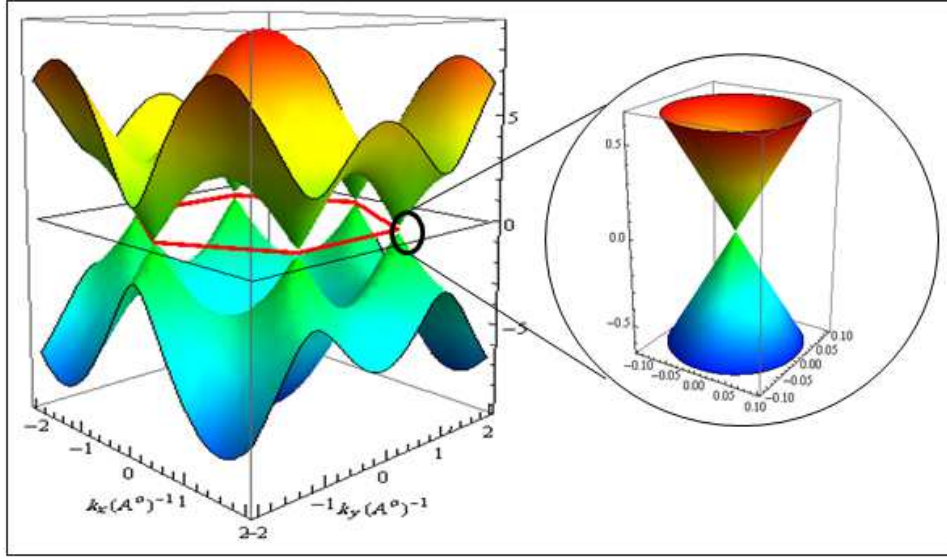


Figure 2.3: Energy spectrum of single layer graphene in the first Brillouin zone.

of graphene with the high symmetry points and how the spectrum look like along the lines connecting these points (K and K' are called Dirac points).

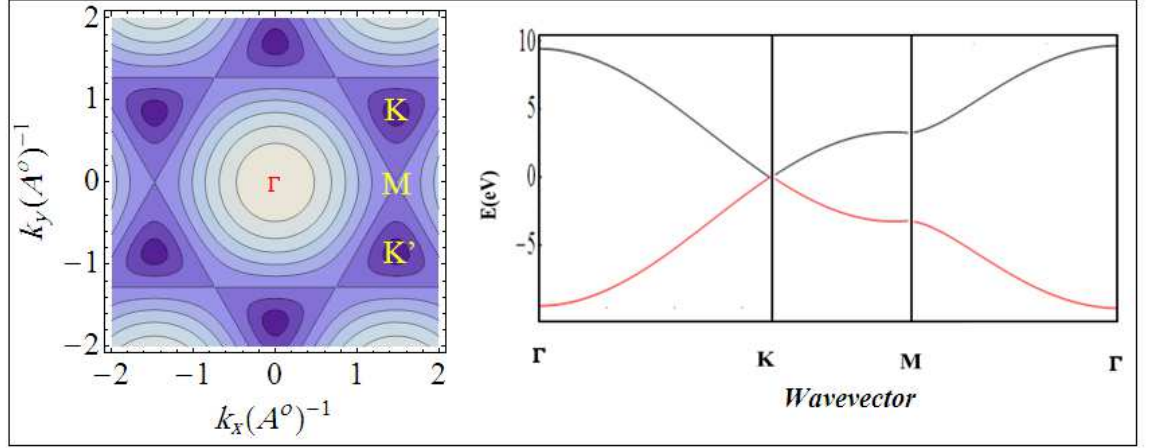


Figure 2.4: Left: the first Brillouin zone in the reciprocal lattice; right: energy spectrum along the lines connecting the high symmetry points.

2.1.2 Continuum Approximation and Dirac-Weyl Hamiltonian

Since we are interested in the transport properties of graphene, which take place near the Fermi energy ($E_F = 0$), it is convenient to expand the Hamiltonian above (Eq.2.19) near the Fermi energy according to $\mathbf{k}=\mathbf{K}+\mathbf{q}$. this can be done using Taylor expansion in the first order which reads:

$$f(k_x, k_y) \simeq f\left(\frac{2\pi}{3a}, \frac{2\pi}{3\sqrt{3}a}\right) + \frac{d}{dk_x} f\left(\frac{2\pi}{3a}, \frac{2\pi}{3\sqrt{3}a}\right) \left(k_x - \frac{2\pi}{3a}\right) + \frac{d}{dk_y} f\left(\frac{2\pi}{3a}, \frac{2\pi}{3\sqrt{3}a}\right) \left(k_y - \frac{2\pi}{3a}\right) \quad (2.25)$$

it is easy to show that

$$\left. \begin{aligned} f\left(\frac{2\pi}{3a}, \frac{2\pi}{3\sqrt{3}a}\right) &= 0 \\ \frac{d}{dk_x} f\left(\frac{2\pi}{3a}, \frac{2\pi}{3\sqrt{3}a}\right) &= \frac{3}{4}\gamma_0 a(\sqrt{3} - i) \\ \frac{d}{dk_y} f\left(\frac{2\pi}{3a}, \frac{2\pi}{3\sqrt{3}a}\right) &= \frac{3}{4}\gamma_0 a(1 + i\sqrt{3}) \end{aligned} \right\} \quad (2.26)$$

Now, according to $k_x = \frac{2\pi}{3a} + q_x$ and $k_y = \frac{2\pi}{3\sqrt{3}a} + q_y$ Eq.2.25 becomes

$$f(q_x, q_y) = \frac{3}{4}\gamma_0 a \left[(\sqrt{3} - i)q_x + (1 + i\sqrt{3})q_y \right] \quad (2.27)$$

this equation can be simplified further to take the following form

$$f(q_x, q_y) = \frac{3}{2}\gamma_0 a (q_x + iq_y) e^{-i\frac{\pi}{6}} \quad (2.28)$$

the extra phase $\frac{\pi}{6}$ can be absorbed in the wave function and the Hamiltonian around the Dirac points becomes

$$H = v_F \begin{pmatrix} 0 & (p_x - ip_y) \\ (p_x + ip_y) & 0 \end{pmatrix} \quad (2.29)$$

where, $v_F = \frac{3}{2\hbar}\gamma_0 a \simeq 10^6 \frac{m}{s}$ and $p_{x,y} = \hbar q_{x,y}$. Finally, Eq.2.29 can be written as

$$H_K = v_F \boldsymbol{\sigma} \cdot \mathbf{p} \quad (2.30)$$

Here, $\boldsymbol{\sigma} = (\sigma_x, \sigma_y)$ Pauli Matrices. Hence, Eq.2.30 is exactly the Dirac-Weyl equation with c (velocity of light) $\rightarrow v_F$. The eigenvalues of the Hamiltonian in Eq.2.30 are $E = \pm v_F |P| = \pm v_F \hbar \sqrt{k_x^2 + k_y^2}$ which is shown in Fig.2.5. So

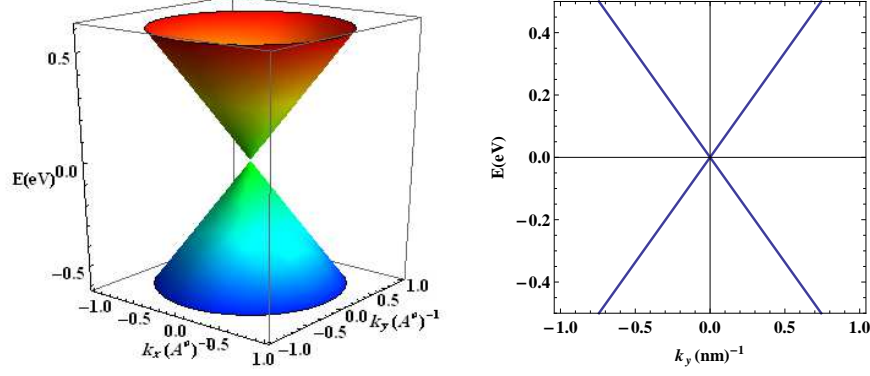


Figure 2.5: Energy spectrum of graphene monolayer around one of the Dirac points

the low energy excitations about the K point in graphene are not described by the Schrödinger equation, but instead by this equation. In a similar way we can expand around the K' point and find the following equation:

$$H_{K'} = v_F \boldsymbol{\sigma}' \cdot \mathbf{p} \quad (2.31)$$

where $\boldsymbol{\sigma}' = (-\sigma_x, \sigma_y)$. Note that this is not exactly the same as the Eq.2.30.

2.1.3 Effective Mass

In graphene, the concept "effective mass" [72] of particle is often a challenge because particles in graphene behave like massless fermions. In other words,

graphene has a linear dispersion relation around the Dirac points K and K' . This leads to divergence in the most commonly used theoretical expression of the effective mass in solid state physics $m^* = \left(\frac{\partial^2 E}{\partial p^2}\right)^{-1}$, with $p = \hbar k$ and k is the crystal momentum [73, 74]. The reason behind this conflict is that the latter definition is only valid for the parabolic spectrums $E(p)$, whereas graphene has a linear spectrum, and for non-parabolic spectrum there are other approaches [75, 76]. Recently, *V. Ariel* and *A. Natan* [77] derived a general formula of the effective mass for parabolic and non-parabolic spectrum:

$$m^*(E, k) = \hbar^2 k \left(\frac{\partial E}{\partial k} \right)^{-1} \quad (2.32)$$

Accordingly, graphene effective mass is given by

$$m^*(E, k) = \frac{\hbar k}{v_f} \quad (2.33)$$

this means that particles in graphene have an effective mass which is linearly dependent on the momentum, this was confirmed experimentally by cyclotron resonance measurements in graphene [19].

2.1.4 Chirality and Helicity

If an object cannot be mapped into its mirror image by only translation and rotation, we say it is chiral object, such as the famous Möbuis and Helix. Many other objects which exhibit chirality are gloves, human

body and shoes. On the other hand, helicity is the projection of the spin of the particle on its momentum direction (direction of motion). For massless particle, like fermions in graphene around one of the Dirac points, helicity and chirality are the same. In graphene, the helicity operator (or chirality) can be defined using the pseudospin $\boldsymbol{\sigma}$ of the sublattice

$$h_\xi = \xi \frac{\boldsymbol{\sigma} \cdot \mathbf{p}}{|\mathbf{p}|} \quad (2.34)$$

Where Here, $\xi = +, -$ for the point K and K' , respectively.

2.1.5 Klein Tunneling

Klein tunneling (or paradox) was first obtained by *Oskar Klein* in 1929 when he applied Dirac equation to the problem of electron scattering from **1D** potential barrier. He showed that for normal incidence electrons unimpededly tunnel (full transmission) through the barrier even when it approaches infinity. In graphene, Klein tunneling also holds for normal incidence, but here it is a consequence of the chirality conservation, see Fig.2.6 [78]. Assume that an electron is travelling in the positive x-direction, using the Heisenberg equation one can find its velocity (or velocity operator) as $v_x \approx i \frac{[H, x]}{\hbar} = \sigma_x$, and the change in velocity is given by $\frac{dv_x}{dt} \approx i \frac{[H, \sigma_x]}{\hbar} = 2\sigma_z k_y$. Hence, for a normal incidence ($k_y = 0$) the velocity is constant of motion and therefore backscattering is forbidden.

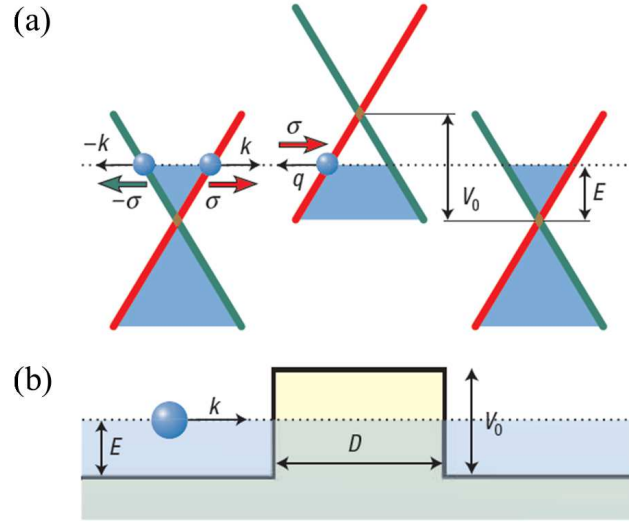


Figure 2.6: Illustration of the Klein tunneling through a potential barrier: (a) Schematic diagram of a single layer graphene spectrum. (b) potential barrier with height V_0 and width D .

2.2 Bilayer Graphene

Bilayer graphene has many special properties due to its lattice structure, leading to the peculiar band structure that we will discuss in details in this section. Bilayer graphene lattice consists of two single layers graphene, with layer spacing $d = 0.334 \text{ nm}$, stacked upon each other such that A atoms in the first layer are connected to the B atoms in the second layers (Bernal stacking [79]), see Fig. 2.7. Where γ_0 is the coupling between two nearest neighbors carbon atoms in the same layer ($A_i \leftrightarrow B_i$), γ_1 denotes the direct interlayer coupling between the atoms ($A_2 \leftrightarrow B_1$), γ_3 describes the interlayer coupling between the atoms ($B_2 \leftrightarrow A_1$) and γ_4 characterizes the interlayer coupling between ($A_1 \leftrightarrow A_2$) as well as ($B_1 \leftrightarrow B_2$). For typical values of

these parameters in bilayer graphene, $\gamma_0 = 3.16$ eV, $\gamma_1 = 0.381$ eV, $\gamma_3 = .38$ eV, $\gamma_4 = 0.14$ eV [80], see [81–83] for other determination methods of the electronic structure of bilayer graphene, such as infrared spectroscopy and Raman scattering. As in the single layer graphene lattice, bilayer graphene

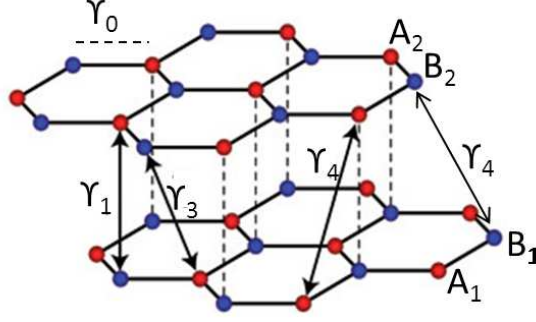


Figure 2.7: Bilayer graphene lattice structure

has a triangular Bravais lattice as well as reciprocal lattice and a hexagonal **BZ**. The calculation of the electronic structure using the **TB** is similar to the one of the single layer graphene.

2.2.1 Tight Binding Model

In bilayer graphene, the unit cell contains four inequivalent carbon atoms, therefore we have four $2p_z$ orbitals wave function. Consequently, the bilayer **TB** Hamiltonian is a 4×4 matrix, which can be seen as two single layer Hamiltonian on the diagonal and the other elements represent the hopping

between atoms in different layers.

$$H = \begin{pmatrix} \varepsilon_{A_1} & -\gamma_0 f(k) & \gamma_4 f(k) & -\gamma_3 f^*(k) \\ -\gamma_0 f^*(k) & \varepsilon_{B_1} & \gamma_1 & \gamma_4 f(k) \\ \gamma_4 f^*(k) & \gamma_1 & \varepsilon_{A_2} & -\gamma_0 f^*(k) \\ -\gamma_3 f(k) & \gamma_4 f^*(k) & -\gamma_0 f(k) & \varepsilon_{B_2} \end{pmatrix} \quad (2.35)$$

where the new **TB** parameters defined as:

$$\begin{aligned} \gamma_1 &= \langle \phi_{A_2} | H | \phi_{B_1} \rangle \\ \gamma_3 &= -\langle \phi_{A_1} | H | \phi_{B_2} \rangle \\ \gamma_4 &= \langle \phi_{A_1} | H | \phi_{A_2} \rangle = \langle \phi_{B_1} | H | \phi_{B_2} \rangle \\ \varepsilon_{A_i} &= \langle \phi_{A_i} | H | \phi_{A_i} \rangle \\ \varepsilon_{B_i} &= \langle \phi_{B_i} | H | \phi_{B_i} \rangle \end{aligned} \quad (2.36)$$

where ε_{A_i} and ε_{B_i} , $i = 1, 2$ (first and second layers) represent the on-site energy. We see that the hopping matrix element ($H_{A_2, B_1} = H_{B_1, B_2} = \gamma_1$) does not contain the factor $f(k)$, which represent the in-plane hopping. This is because γ_1 involves a direct or vertical bond, in contrast to $\gamma_{3,4}$ (characterize none vertical bond) which involve in-plan orbital components so that they are associated with the factor $f(k)$. In Fig. 2.8 (a) we show the energy spectrum in the first **BZ** along the k_y axis where it intersects with the two Dirac points K and K' at the corners, and at the center with the point Γ . The energy spectrum around the K point is showing in the inset of Fig.

2.8 (a). The colors (Green and red) in Fig. 2.8 will help us identifying the different propagating modes in Chapter 4. See [85–89] for more details on **TB** of **BLG**. As we mentioned earlier, we are interested in the band structure

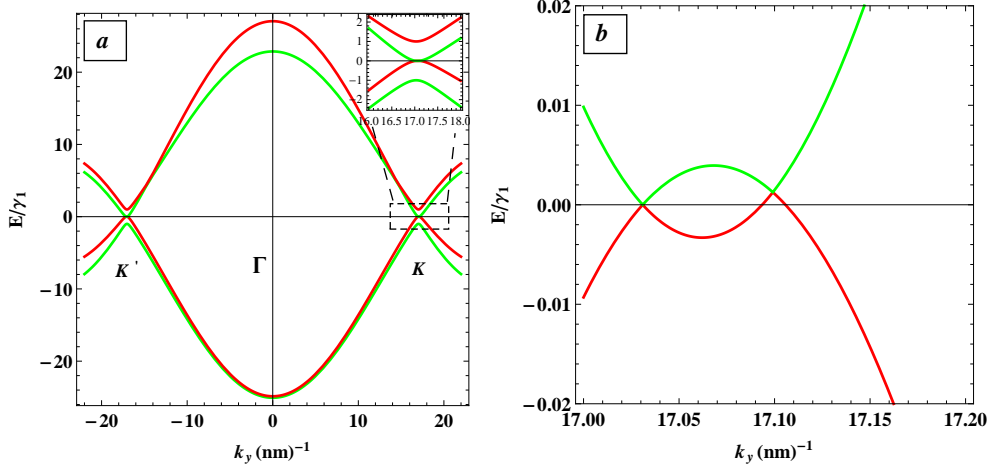


Figure 2.8: (a) Energy spectrum of Bilayer graphene in the first **BZ** along k_y intersecting the two Dirac Points K and K' at the corners and Γ at the center. (b) The low energy spectrum showing the trigonal warping at the Dirac point K . The spectrum in (a) and (b) obtained using Eq. 2.35)

around the Dirac points. Therefore it is useful to expand the Hamiltonian Eq. 2.35 around one of the Dirac points, say K point. This can be done by expanding the factor $f(k)$ around the Dirac point, see Eqs. 2.25,2.26,2.27, which leads to:

$$H = \begin{pmatrix} \varepsilon_{A_1} & v_F \pi^\dagger & -v_4 \pi^\dagger & v_3 \pi \\ v_F \pi & \varepsilon_{B_1} & \gamma_1 & -v_4 \pi^\dagger \\ -v_4 \pi & \gamma_1 & \varepsilon_{A_2} & v_F \pi^\dagger \\ v_3 \pi^\dagger & -v_4 \pi & v_F \pi & \varepsilon_{B_2} \end{pmatrix} \quad (2.37)$$

where $v_{3,4} = \frac{3}{2\hbar}\gamma_{3,4}a$ are related to the hopping parameters, $\pi = \xi p_x + ip_y$ and $\pi^\dagger = \xi p_x - ip_y$. Here, $\xi = +, -$ for the point K and K' , respectively. Without the skew parameters γ_3 and γ_4 , the corresponding spectrum of Eq. 2.37 is

$$E_\pm^s = \frac{1}{2} \left[\pm s\gamma_1 + s\sqrt{\gamma_1^2 + 4p^2} \right] \quad (2.38)$$

where the \pm sign is negative for the inner bands, which touched at K point, and positive for the outer bands, $s = \pm$ determines whether the energy band corresponds to the conduction band ($s = +$) or the valence band ($s = -$). The corresponding spectrum of the original Hamiltonian (Eq. 2.35) (Solid curves) around the K point and its approximated one (Eq. 2.37) (Dashed curves) are shown in Fig. 2.9, with all interlayer coupling parameters γ_1, γ_3 and γ_4 in Fig. 2.9 (a), and with only γ_1 in Fig. 2.9 (b). It shows a good agreement for the latter one even for high energy, whereas for the first one a good agreement obtains at low energy. Therefore, the latter Hamiltonian (2.37) will be used further in this work.

2.2.2 Effective Two Band Hamiltonian

It is useful when studying the low energy transport properties to describe the system with an effective Hamiltonian. Such Hamiltonian can be obtained as follows. Considering only the direct interlayer coupling γ_1 and an interlayer

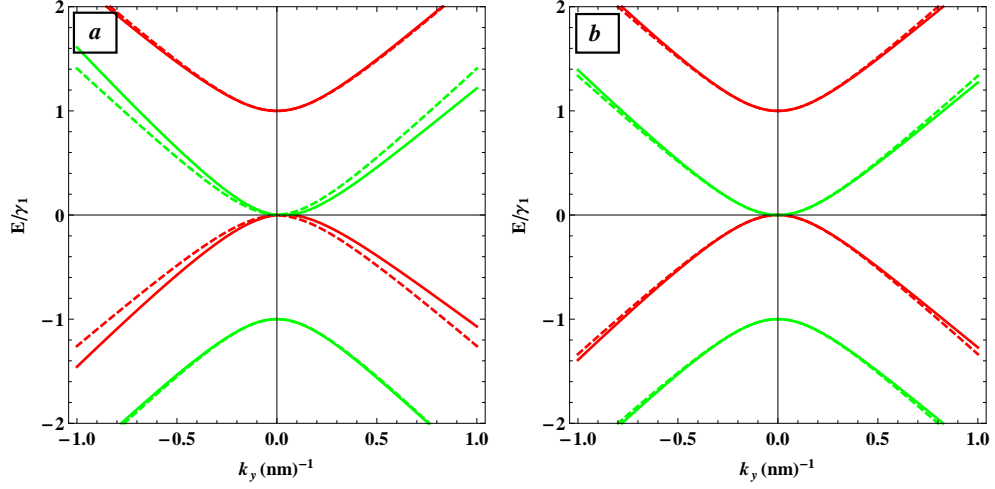


Figure 2.9: A comparison between the energy spectrum obtained using Eq. 2.35 (Solid) Eq. 2.37 (Dashed). (a) with all hoping parameters $\gamma_1 = 0.381$ eV, $\gamma_3 = 0.38$ eV and $\gamma_4 = 0.14$ eV. (b) with $\gamma_1 = 0.381$ eV, $\gamma_3 = \gamma_4 = 0$ eV.

potential difference δ , the Hamiltonian then reads

$$H = \begin{pmatrix} \delta & v_F \pi^\dagger & 0 & 0 \\ v_F \pi & \delta & \gamma_1 & 0 \\ 0 & \gamma_1 & -\delta & v_F \pi^\dagger \\ 0 & 0 & v_F \pi & -\delta \end{pmatrix} \quad (2.39)$$

with the following change in columns and rows $C_3 \rightarrow C_1$ then $R_3 \rightarrow R_1$, the latter Hamiltonian can be written as

$$H = \begin{pmatrix} -\delta & \gamma_1 & 0 & v_F \pi^\dagger \\ \gamma_1 & \delta & v_F \pi & 0 \\ 0 & v_F \pi^\dagger & \delta & 0 \\ v_F \pi & 0 & 0 & -\delta \end{pmatrix} = \begin{pmatrix} H_{11} & H_{12} \\ H_{21} & H_{22} \end{pmatrix} \quad (2.40)$$

where H_{ij} is a 2×2 block. Using Schur determinant identity

$$\text{Det}[H - E] = \text{Det}[H_{11} - E] \cdot \text{Det}[H_{22} - E - H_{12}(H_{11} - E)^{-1}H_{21}] = 0 \quad (2.41)$$

and with $H_{11} - E \rightarrow H_{11}$ for $E \ll \gamma_1$ [90], one obtain

$$\begin{aligned} H &= \text{Det}[H_{22} - H_{12}(H_{11})^{-1}H_{21}] \\ &= \begin{pmatrix} \delta + \frac{\delta\pi^\dagger\pi}{(-\gamma_1^2 - \delta^2)} & \frac{\gamma_1\pi^{\dagger 2}}{(-\gamma_1^2 - \delta^2)} \\ \frac{\gamma_1\pi^2}{(-\gamma_1^2 - \delta^2)} & -\delta - \frac{\delta\pi\pi^\dagger}{(-\gamma_1^2 - \delta^2)} \end{pmatrix} \end{aligned} \quad (2.42)$$

For $\delta \ll \gamma_1$, $(-\gamma_1^2 - \delta^2) \rightarrow -\gamma_1^2$, the effective Hamiltonian becomes

$$H_{eff} = \frac{1}{2m} \begin{pmatrix} 0 & \pi^{\dagger 2} \\ \pi^2 & 0 \end{pmatrix} + \delta \left[\sigma_z - \frac{v_F^2}{\gamma_1^2} \begin{pmatrix} \pi^\dagger\pi & 0 \\ 0 & -\pi\pi^\dagger \end{pmatrix} \right] \quad (2.43)$$

where, $m = \frac{\gamma_1}{2v_F^2}$ is the effective mass of electrons in bilayer graphene. An effective Hamiltonian that also takes trigonal warping (v_3) into account can be obtained in the same manner. The same result can be obtained using Green function to derive the effective Hamiltonian [88].

$$H_{eff} = \frac{1}{2m} \begin{pmatrix} 0 & \pi^{\dagger 2} \\ \pi^2 & 0 \end{pmatrix} + v_3 \begin{pmatrix} 0 & \pi^\dagger \\ \pi & 0 \end{pmatrix} + \delta \left[\sigma_z - \frac{v_F^2}{\gamma_1^2} \begin{pmatrix} \pi^\dagger\pi & 0 \\ 0 & -\pi\pi^\dagger \end{pmatrix} \right] \quad (2.44)$$

This effective Hamiltonian is applicable for energy range $|E| < \frac{\gamma_1}{4}$ [88].

We show, in Fig. 2.10, a comparison between the spectrum obtained from the full Hamiltonian (Eq. 2.37) and the two band Hamiltonian (Eq. 2.44),

the spectrum on the left includes only γ_1 and on the right includes trigonal warping v_3 , which will be discuss in the next section.

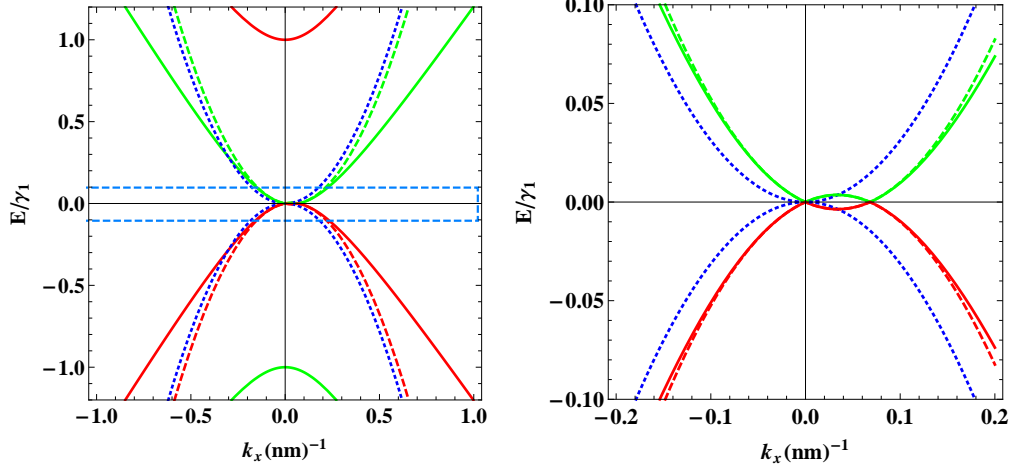


Figure 2.10: Left: The energy spectrum obtained from the four band model (Solid) Eq. 2.37 and the effective two band model (Dashed)Eq. 2.44. Right: Showing that trigonal warping cannot be obtained using the effective two band model (Blue dotted) Eq. 2.37. The blue dashed rectangle shows the region where the two band model is valid

2.2.3 Trigonal Warping

Trigonal warping (**TW**) is arising from the skew parameter γ_3 , it affects the band structure of **BLG** at the low energy $|E| < 1 \text{ meV}$ [91] whereas at the high energy its effect is negligible. The Dirac cone (K point) is splitting into four cones due to the **TW**, three legs and one at the centre, see Fig. 2.11. The left and right columns show the band structure at low energy with and without **TW**, respectively. It has a great influence on the transport properties of **BLG**. For example, although conductivity is not depend on the

strength of the **TW**, it is 3 times as large as without it [92]. Recently, there are many studies on the transport properties of **BLG** take into account the **TW** effect, see [93–96].

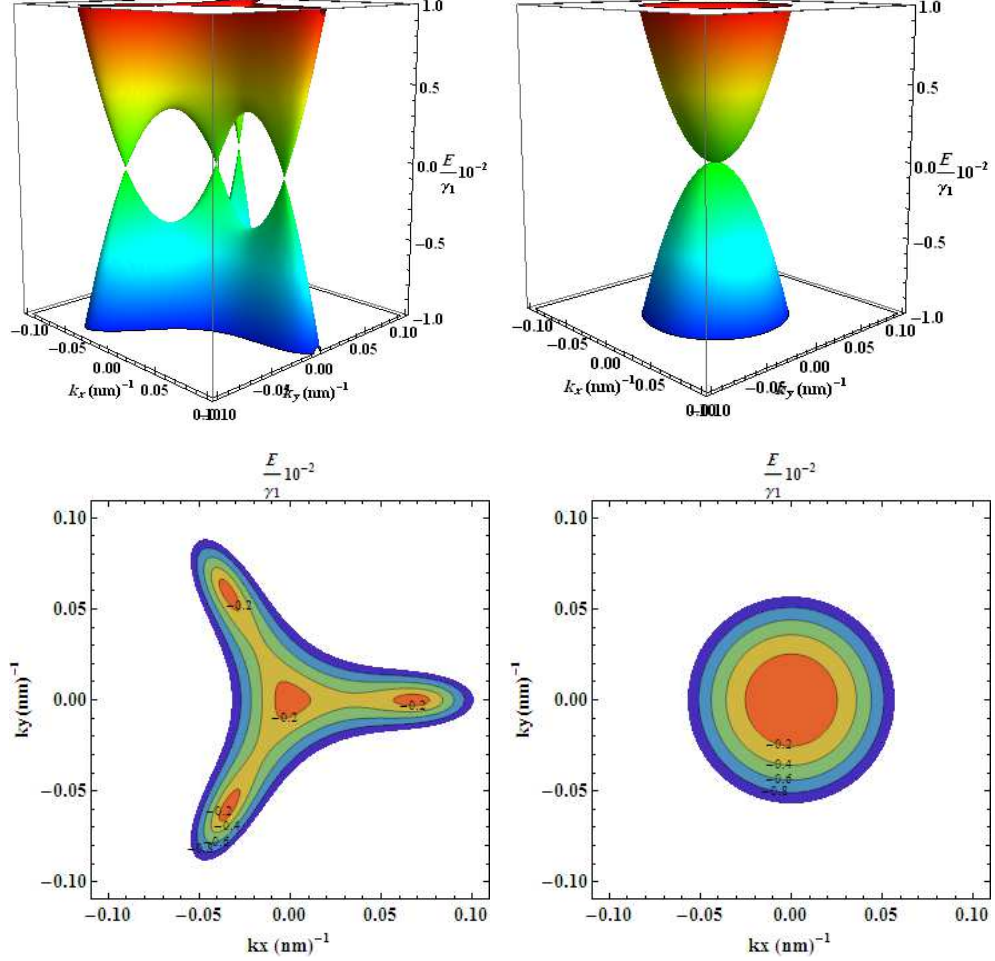


Figure 2.11: Left column: (Top) **3D** plot of the low energy spectrum (trigonal warping); (Bottom) equi-energy lines of the trigonal warping. Right column: The same as in the left column but with $\gamma_3 = \gamma_4 = 0$.

2.2.4 Electric Field Effect

In **BLG** the on-site energy can be considered as an extra degree of freedom when it is different between the two layers. This can be implemented by adding an extra potential difference term on the diagonal of the Hamiltonian, see Eq. 2.39. The pristine graphene is considered as a metal, hence it can not replace silicon. One method to open an energy gap in the spectrum of **BLG** is to apply an external electric potential [97]. Then, the corresponding spectrum in this case is

$$E_{\pm}^s = s \left[k_x^2 + k_y^2 + \delta^2 + \frac{\gamma_1^2}{2} \pm \sqrt{(k_x^2 + k_y^2)(4\delta + \gamma_1^2) + \frac{\gamma_1^4}{4}} \right] \quad (2.45)$$

In Fig. 2.12, we show the spectrum of the full and two band Hamiltonian on the left and as a spatial case when $\gamma_1 = \delta = 0$ we recover the **SLG** spectrum on the right.

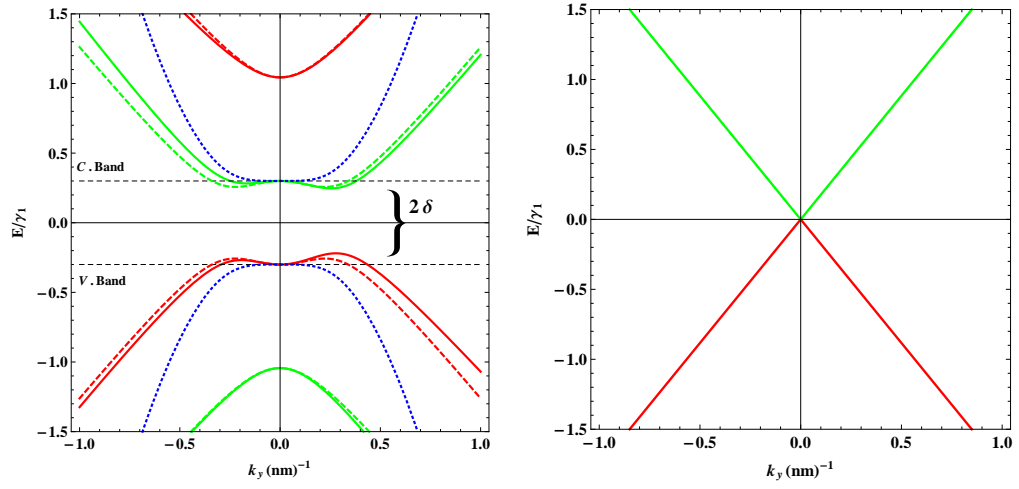


Figure 2.12: Left: Energy spectrum of bilayer graphene placed in an electric potential (biased **BLG**) with $\delta = 0.2 \gamma_1$, blue dotted curves corresponding to the effective two band model, solid and dashed curves account for the four band model with and without $\gamma_{3,4}$, respectively. Right: energy spectrum of SLG with $\delta = \gamma_1 = 0$

Chapter 3

CONDUCTANCE AND SHOT NOISE IN GRAPHENE AND ITS BILAYERS

3.1 Introduction

One of the remarkable transport measurements in graphene is the high electron mobility at the room temperature. Experimental measurements of conductance show that it is symmetric in energy, so that the mobility for electrons and holes are nearly the same [18]. Moreover, the dominant mechanism of scattering in graphene is due to defects, and therefore mobility is

independent of temperature [5, 6]. It is really surprising that in the case of

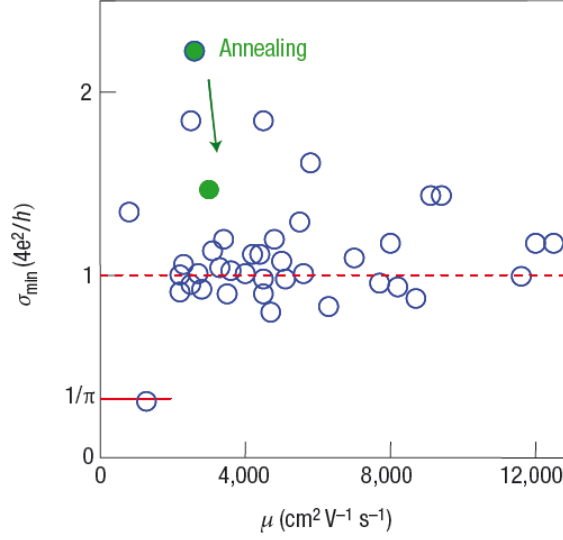


Figure 3.1: Minimum conductivity of graphene .

vanishing carrier density, near the Dirac points, graphene still has a finite minimum conductivity which is of the order of the conductivity quantum $\frac{4e^2}{h}$ [5]. There are many considerations and theories that describe the minimum conductivity of graphene [98] – [104]. Yet, the origin of the minimum conductivity is still ambiguous. Most theories say that minimum conductivity is $\frac{4e^2}{\pi h}$, which is π smaller than the experimental value, see Fig. 3.1 [18]. This disagreement between theory and experiment is well known as "*mystery of missing a π* " and it is unclear whether it is attributed to the limited resolution of the experimental equipments or to theoretical approximations.

3.2 Landauer-Büttiker Formula

The conductance of a single quantum channel is given by $G = g \frac{e^2}{h} T$, where T is the electron transmission probability and g represents the spin and valley degeneracy which is $g = 4$ in graphene. For biased system, the current fluctuation (shot noise) for a single channel, due to the charge discretization, is given by $\langle (\delta I)^2 \rangle = 2e \langle I \rangle (1 - T)$. Then, for multichannel conductor, the shot noise can be obtained by summing over all transmission channels

$$S_I = \frac{2e^3 |V|}{h} \sum_{n=0}^{N-1} T_n (1 - T_n) \quad (3.1)$$

The Poissonian noise induced by random and independent electrons, such as in tunnel junction, is found at low transparency $T_n \ll 1$

$$S_I = S_P = \frac{2e^3 |V|}{h} \sum_{n=0}^{N-1} T_n = 2e \langle I \rangle \quad (3.2)$$

Fano factor (F) is defined as the ratio of a measured shot noise to the Poissonian shot noise, it is the regular way to quantify the shot noise of a system.

$$F = \frac{S_I}{S_P} = \frac{\sum_{n=0}^{N-1} T_n (1 - T_n)}{\sum_{n=0}^{N-1} T_n} \quad (3.3)$$

Therefore, in the ballistic regime (i.e. $T_n \rightarrow 1$) $F = 0$, while at small transparency (i.e. $T_n \rightarrow 0$) $F = 1$ and $F = 1/3$ for diffusive systems. For a sample with width W and length L and in the limit $W \gg L$ the summation above can be replaced by an integral [105–107]. Therefore the Landauer-Büttiker

formula for the conductance and Fano Factor can be written as [108]

$$\mathbf{G} = G_0 \frac{L_y}{2\pi} \int_{-\infty}^{+\infty} dk_y T \quad (3.4)$$

$$\mathbf{F} = \frac{\int_{-\infty}^{+\infty} dk_y T(1 - T)}{\int_{-\infty}^{+\infty} dk_y T} \quad (3.5)$$

where L_y is the width of the sample in the y -direction and $G_0 = \frac{4e^2}{h}$, the factor 4 is due to the valley and spin degeneracy in graphene. Shot noise and conductance in graphene has been studied theoretically many years ago [30, 101] and conclude that the evanescent waves are responsible for the transport at the Dirac point, see also [109–111]. In the next two sections, we briefly present the conductivity and the fano factor of single layer graphene and its bilayer.

3.3 Single Layer Graphene

J. Tworzydło [101], used graphene strip with length L and width W connected by two electrodes, which can be modelled experimentally by heavily-doped graphene lead, to study the shot noise and conductivity. By solving Dirac equation in the desired regions and matching the solutions at the interfaces taking into account the infinite mass boundary conditions [112], he obtained the transmission probability, Fano factor and conductivity. In Fig. 3.2 (a) [101], the conductivity and Fano factor are plotted as a function of

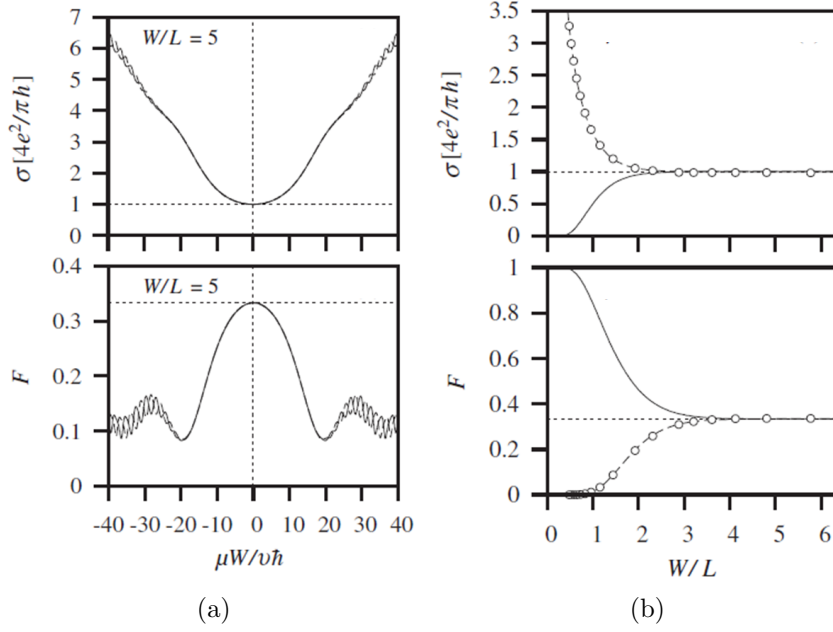


Figure 3.2: Conductivity and Fano factor as a function of: (a) Fermi energy for a fixed aspect ratio of the graphene strip ; (b) the aspect ratio of the graphene strip at the Dirac point

the Fermi energy which modelled here by the electric potential energy μ . It appears that conductivity has a minima at the Dirac point ($\mu = 0$) which corresponds to a maxima in the Fano factor. These two quantities depend on the graphene strip geometry as depicted in Fig. 3.2 (b) [101] and both reach a universal value $\sigma_{min} = \frac{G_0}{\pi}$ and $F_{max} = \frac{1}{3}$ for a wide and short graphene strip (i.e $W/L \geq 4$).

Recently, researchers study also conductance and shot noise for non-squared potential [113] and the influence of a magnetic field [114]. Moreover, a negative differential conductance in graphene has been reported [115].

3.4 Bilayer Graphene

Since we are interested in the graphene bilayer, we will go through this section in more details to calculate the transmission probability, conductivity and Fano factor. We use here the same setup in [105]. Assuming a graphene sheet in the $x - y$ plane contains three different regions, with two heavily doped contact regions for $x > b$ and $x < 0$. Between these two contact regions is a weakly doped strip with length b and width W . The doping in these three regions induce a potential profile, see Fig. 3.3, of the form

$$V(x) = \begin{cases} -V_0 & , x < 0 \text{ or } x > b \\ 0 & , b > x > 0 \end{cases} \quad (3.6)$$

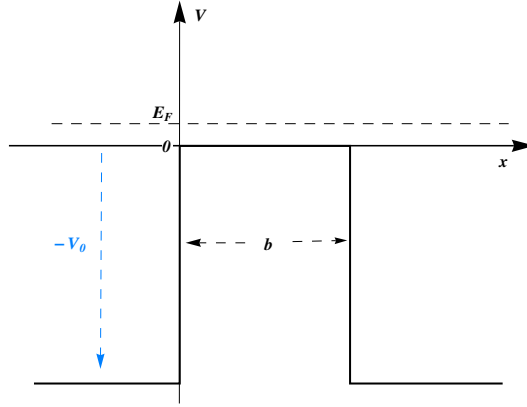


Figure 3.3: Schematic of the electric potential applied to the bilayer graphene strip.

Bilayer graphen is governed by 4×4 Hamiltonian which can be written as

$$H = \begin{pmatrix} V & v_F \pi^\dagger & 0 & 0 \\ v_F \pi & V & \gamma_1 & 0 \\ 0 & \gamma_1 & V & v_F \pi^\dagger \\ 0 & 0 & v_F \pi & V \end{pmatrix} \quad (3.7)$$

where $\pi = p_x + ip_y$, $\pi^\dagger = p_x - ip_y$ are the in-plan momenta and its conjugate with $p_{x,y} = -i\hbar\partial_{x,y}$. Since the momentum in the y -direction is a conserved quantity (i.e. $[H, p_y] = 0$) the wave function of the system can be written as

$$\psi(x, y) = e^{ik_y} \begin{pmatrix} \phi_{A_1} \\ \phi_{B_1} \\ \phi_{A_2} \\ \phi_{B_2} \end{pmatrix} \quad (3.8)$$

and when the Hamiltonian above acts on this wave function, it leads to four coupled differential equations that can be decoupled and one can obtain the full solution, see next chapter for more details. After decoupling the four resulting equations one obtain

$$\left[\frac{d^2}{dx^2} + k_\pm^2 \right] \phi_{B1} = 0 \quad (3.9)$$

with

$$k_x^\pm = \left[-k_y^2 + \frac{\epsilon^2}{l^2} \pm \frac{\epsilon}{l^2} \right]^{1/2} \quad (3.10)$$

Here $l = \frac{\hbar v_F}{\gamma_1}$, for real value of k_x^\pm we have two propagating modes k^+ and k^- . Then, the corresponding energy spectrum of bilayer graphene is given by

$$E_\pm^s = \pm \frac{1}{2} \left[1 + s \sqrt{1 + (2lk_x)^2 + (2lk_y)^2} \right]^{1/2} \quad (3.11)$$

In Fig. 3.4, we show the energy bands and the different transmission probabilities corresponding to the different modes. Details about how to calculate

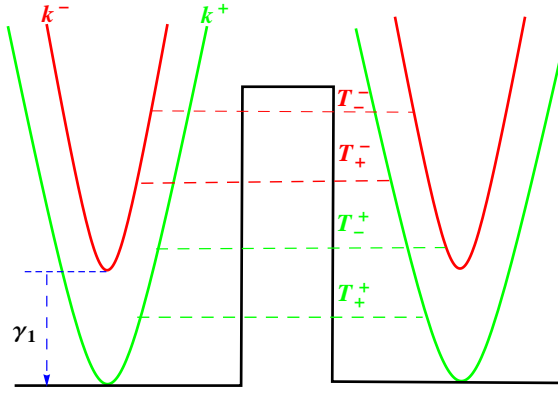


Figure 3.4: Energy bands and the different transmission probabilities corresponding to the different modes

these transmission probabilities will be provided in the next chapter. Here we will show directly the results of the transmission, conductivity and Fano factor using our approach which are exactly the same as in [105] for this system. In Fig. 3.5 (a,b,c,d) we show the different transmission channels and the total transmission probability in Fig. 3.5 (e) which calculated in [105]. The total transmission through the different channels ($T^+ = T_+^+ + T_-^+$ and $T^- = T_+^- + T_-^-$) are shown in Fig. 3.6 and the total transmission probability of the two channel is shown in Fig.3.7. Finally, we show the conductivity

and Fano factor as a function of the Fermi energy in Fig. 3.8. Comparing to the single layer graphene, conductivity of the bilayer is twice as much as the single layer $\sigma_{bilayer} = 2\sigma_{single} = 2G_0/\pi$ while the Fano factor is the same for both $F_{bilayer} = F_{single} = 1/3$.

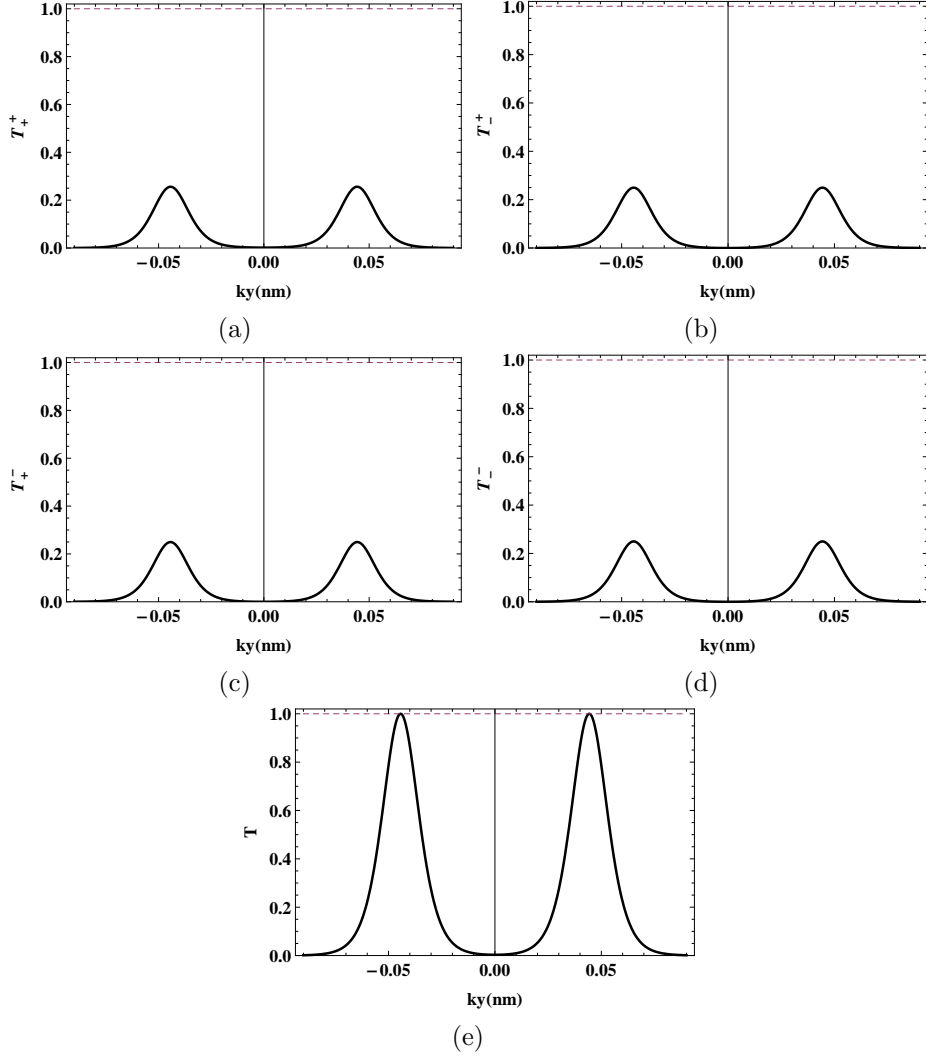


Figure 3.5: Different transmission channels in bilayer graphene around the Dirac point ($E = 0$) with $b = 50l$

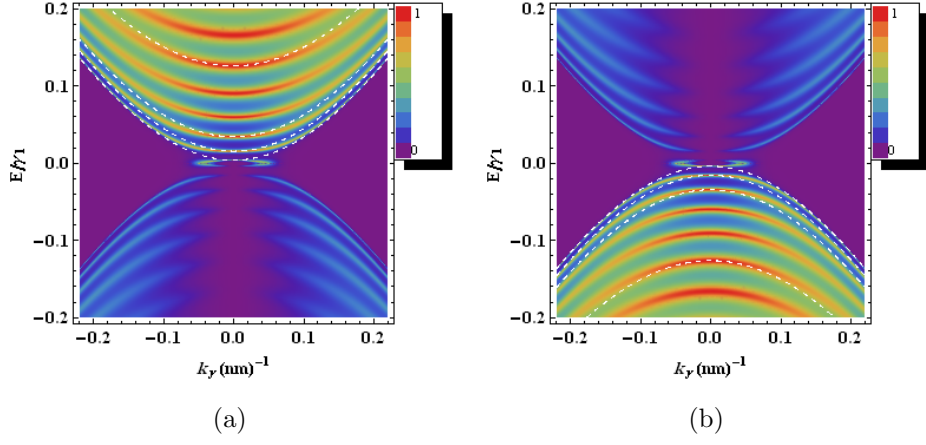


Figure 3.6: Density plot of the total transmission through the first mode $T^+ = T_+^+ + T_-^+$ (left) and through the second mode $T^- = T_-^- + T_+^-$ (right)

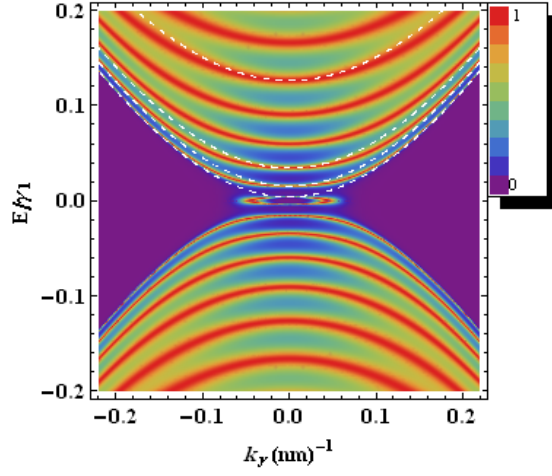


Figure 3.7: Total transmission probability as a function of the energy E and the transverse wave vector k_y with $b = 50 \text{ } l$ and $V_0 = -50 \gamma_1$.

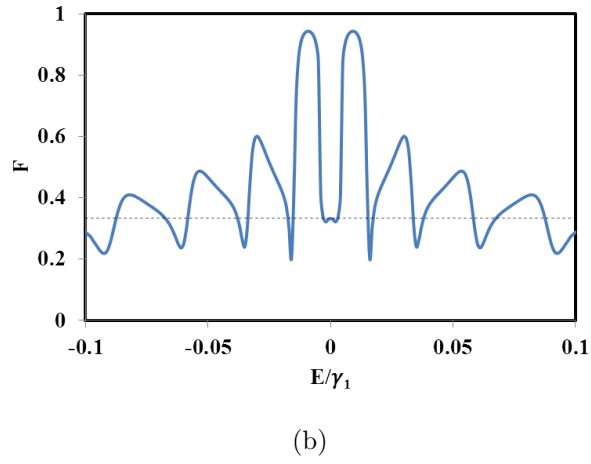
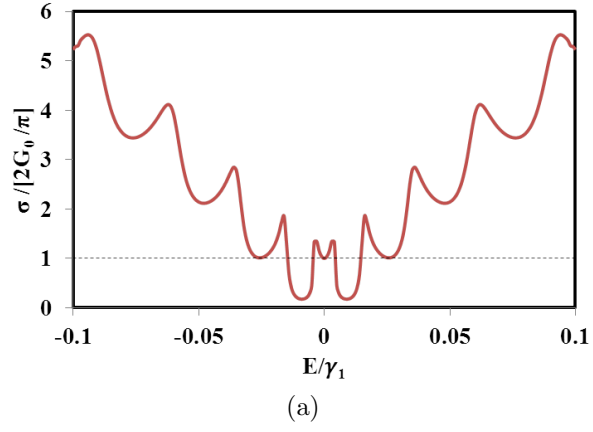


Figure 3.8: (a) Conductivity and (b) Fano factor as a function of Fermi energy with $b = 50 \, l$ and $V_0 = -50 \, \gamma_1$.

Chapter 4

BAND TUNNELING THROUGH DOUBLE BARRIER IN GRAPHENE BILAYER

4.1 Introduction

The most important application of graphene is to possibly replace silicon in IT-applications. But the biggest obstacle is to create a gap and control the electron mobility in graphene taking into account the so called

Klein tunneling which makes the task more complicated [78, 118]. However, one can create an energy gap in the spectrum in many different ways, such as by coupling to substrate or doping with impurities [119, 120] or in bilayer graphene by applying an external electric field [28, 29, 121].

Bilayer graphene is two stacked (Bernal stacking [79]) monolayer graphene sheets, each with honeycomb crystal structure, with four atoms in the unit cell, two in each layer. In the first Brillouin zone, the tight binding model for bilayer graphene [70] predicted four bands, two conduction bands and two valance bands, each pair is separated by an interlayer coupling energy of the order $\gamma_1 \approx 0.4$ [122]. At the Dirac points, one valance band and one conduction band touch at zero energy, whereas the other bands are split away from the zero energy by γ_1 [88]. Further details about band structure and electronic properties of bilayer graphene can be found in the literature [19, 91, 123–129].

Tunneling of quasiparticles in graphene, which mimics relativistic quantum particles such as Dirac fermions in quantum electrodynamics (*QED*), plays a major role in scattering theory which allows us to develop a theoretical framework that allows us to investigate different physical phenomena that are not present in the non relativistic regime, such as the Klein-paradox [78, 118]. In monolayer garphene, there were many studies on the tunneling of electrons through different potential shapes [32, 130–132] while the study of tunneling electrons in bilayer graphene has been restricted to energies less than the interlayer coupling parameter γ_1 so that only one channel dominates transmission and the two band model is valid [33, 34, 105, 133].

Recently, tunneling of electrons in bilayer graphene has been studied using the four band model for a wide range of energies, even for energies larger than γ_1 [134]. Electron transport measurements can be used effectively to probe the nature of current carriers in graphene devices.

In this chapter, we investigate the band tunneling and conductance through square double barrier using the four band model in bilayer graphene. It is organized as follows. In section 2, we establish a theoretical framework using the four band model leading to four coupled differential equations. In section 3, by using the transfer matrix at boundaries together with the incident, transmitted and reflected currents we end up with eight transmission and reflection probabilities as well as the corresponding conductance. We deal with two band tunneling and analyze their features with and without the interlayer potential difference, in section 4. We do the same job in section 5 but by considering four band energy and underline the difference with respect to other case. In section 6, we show the numerical results for the conductance and investigate the contribution of each transmission channel.

4.2 Theoretical Model

In monolayer graphene, the unit cell has inequivalent atoms (usually called A and B). Bilayer graphene on the other hand is a two stacked monolayer graphene (Bernal stacking) and hence has four atoms in the unit cell. The relevant Hamiltonian near the K point (the boundary of the Brillouin zone),

can be found using the nearest-neighbor tight binding approximation [19]

$$H = \begin{pmatrix} V^+ & v_F\pi^\dagger & -v_4\pi^\dagger & v_3\pi \\ v_F\pi & V^+ & \gamma_1 & -v_4\pi^\dagger \\ -v_4\pi & \gamma_1 & V^- & v_F\pi^\dagger \\ v_3\pi^\dagger & -v_4\pi & v_F\pi & V^- \end{pmatrix} \quad (4.1)$$

where $v_F = \frac{\gamma_0}{\hbar} \frac{3a}{2} \approx 10^6 \text{ m/s}$ is the fermi velocity of electrons in each graphene layer, $a = 0.142 \text{ nm}$ is the distance between adjacent carbon atoms, $v_{3,4} = \frac{v_F\gamma_{3,4}}{\gamma_0}$ represent the coupling between the layers, $\pi = p_x + ip_y$, $\pi^\dagger = p_x - ip_y$ are the in-plan momenta and its conjugate with $p_{x,y} = -i\hbar\partial_{x,y}$. $\gamma_1 \approx 0.4 \text{ eV}$ is the interlayer coupling term and V^+, V^- are the potentials on the first and second layer, respectively. The skew parameters, $\gamma_3 \approx 0.315 \text{ eV}$ and $\gamma_4 \approx 0.044 \text{ eV}$ have negligible effect on the band structure at high energy [88, 91]. Recently, it was shown that even at low energy these parameters have also negligible effect on the transmission [134], hence we neglect them in our calculations.

Under the above approximation and for double barrier potential configuration in Figure 4.1 our previous Hamiltonian (4.1) can be written as follows in each potential region where we define regions as follows: $j = 1$ for $x \leq a$, $j = 2$ for $a < x \leq b$, $j = 3$ for $b < x \leq c$, $j = 4$ for $c < x \leq d$ and $j = 5$ for $x > d$

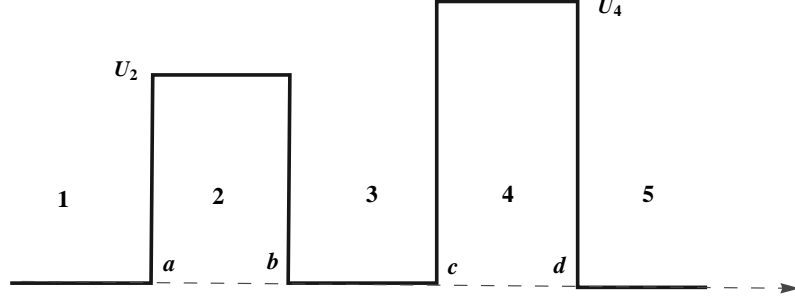


Figure 4.1: The parameters of a rectangular double barrier structure.

so that in the j -th region we have

$$H_j = \begin{pmatrix} V_j^+ & \nu_F \pi^\dagger & 0 & 0 \\ \nu_F \pi & V_j^+ & \gamma_1 & 0 \\ 0 & \gamma_1 & V_j^- & \nu_F \pi^\dagger \\ 0 & 0 & \nu_F \pi & V_j^- \end{pmatrix} \quad (4.2)$$

We define the potential on the first and second layer by $V_j^\pm = U_j \pm \delta_j$, where U_j is the barrier strength and δ_j is the electrostatic potential in the j -th region

$$V_j^\pm = \begin{cases} 0, & j = 1 \\ U_2 \pm \delta_2, & j = 2 \\ 0, & j = 3 \\ U_4 \pm \delta_4, & j = 4 \\ 0, & j = 5 \end{cases} \quad (4.3)$$

(U_2, δ_2) and (U_4, δ_4) are the barrier potential and the electrostatic potential in regions 2 and 4, respectively.

The eigenstates of (4.2) are four-components spinors $\psi^j(x, y) = [\psi_{A_1}^j, \psi_{B_1}^j, \psi_{A_2}^j, \psi_{B_2}^j]^\dagger$, here \dagger denotes the transpose of the row vector. For a double barrier we need to obtain the solution in each regions as shown in Figure 4.1. Since we have basically two different sectors with zero (1, 3, 5) and nonzero potential (2, 4), a general solution can be obtained in the second sector and then set the potential V_j^\pm to zero to obtain the solution in the first sector. To simplify the notation we introducing the length scale $l = \frac{\hbar v_F}{\gamma_1} \approx 1.76 \text{ nm}$ allows us to define the following dimensionless quantities: $E' = \frac{E}{\gamma_1}$ and $V'_j = \frac{V_j}{\gamma_1}$. Since the momentum along the y -direction is a conserved quantity, i.e $[H, p_y] = 0$, and therefore we can write the spinors as

$$\psi^j(x, y) = e^{iky} [\phi_{A_1}^j, \phi_{B_1}^j, \phi_{A_2}^j, \phi_{B_2}^j]^\dagger \quad (4.4)$$

Now injecting (4.2) and (4.4) in the eigenvalue equation $H_j \psi_j = E'_j \psi_j$, dropping the prime from now on to avoid cumbersome notation, we obtain

$$\begin{pmatrix} U_j + \delta_j & \frac{l}{\hbar} \pi^\dagger & 0 & 0 \\ \frac{l}{\hbar} \pi & U_j + \delta_j & 1 & 0 \\ 0 & 1 & U_j - \delta_j & \frac{l}{\hbar} \pi^\dagger \\ 0 & 0 & \frac{l}{\hbar} \pi & U_j - \delta_j \end{pmatrix} \begin{pmatrix} \phi_{A_1}^j \\ \phi_{B_1}^j \\ \phi_{A_2}^j \\ \phi_{B_2}^j \end{pmatrix} e^{iky} = E_j \begin{pmatrix} \phi_{A_1}^j \\ \phi_{B_1}^j \\ \phi_{A_2}^j \\ \phi_{B_2}^j \end{pmatrix} e^{iky} \quad (4.5)$$

This gives four coupled differential equations

$$-il \left[\frac{d}{dx} + ky \right] \phi_{B1}^j = (\epsilon_j - \delta_j) \phi_{A1}^j \quad (4.6)$$

$$-il \left[\frac{d}{dx} - ky \right] \phi_{A1}^j + \phi_{A2}^j = (\epsilon_j - \delta_j) \phi_{B1}^j \quad (4.7)$$

$$-il \left[\frac{d}{dx} + ky \right] \phi_{B2}^j + \phi_{B1}^j = (\epsilon_j + \delta_j) \phi_{A2}^j \quad (4.8)$$

$$-il \left[\frac{d}{dx} - ky \right] \phi_{A2}^j = (\epsilon_j + \delta_j) \phi_{B2}^j \quad (4.9)$$

where k_y is the wave vector along the y -direction and we have set $\epsilon_j = E_j - U_j$.

It is easy to decouple the first equations to obtain

$$\left[\frac{d^2}{dx^2} + (k_j^s)^2 \right] \phi_{B1}^j = 0 \quad (4.10)$$

where the wave vector along the x -direction is

$$k_j^s = \left[-k_y^2 + \frac{\epsilon_j^2 + (\delta_j)^2}{l^2} + s \frac{1}{l^2} \sqrt{\epsilon_j^2(1 + 4(\delta_j)^2) - (\delta_j)^2} \right]^{1/2} \quad (4.11)$$

where $s = \pm$ denotes the propagating modes which will be discussed latter on. Now for each region one can end up with corresponding wave vector according to Figure 4.1. Indeed, for regions 1, 3 and 5 we have $V_j^\pm = 0$ and then we can obtain

$$k_0^s = \left[-k_y^2 + \frac{\epsilon^2}{l^2} + s \frac{\epsilon}{l^2} \right]^{1/2} \quad (4.12)$$

with $\epsilon = \epsilon_1 = \epsilon_3 = \epsilon_5$, as well as the energy

$$E_{\pm}^s = \pm \frac{1}{2} \left[-s + \sqrt{1 + (2lk_0^s)^2 + (2lk_y)^2} \right] \quad (4.13)$$

However generally, for any region we can deduce energy from previous analysis as

$$\epsilon_{\pm,j}^s = \pm \frac{1}{\sqrt{2}} \left[1 + 2l^2[(k_j^s)^2 + k_y^2] + 2(\delta_j)^2 - s\sqrt{1 + 4l^2[(k_j^s)^2 + k_y^2](1 + 4(\delta_j)^2)} \right]^{1/2} \quad (4.14)$$

The corresponding energy spectrum of the different regions is shown in Figure 4.2. Associated with each real k_0^s , the wave vector of the propagating wave in

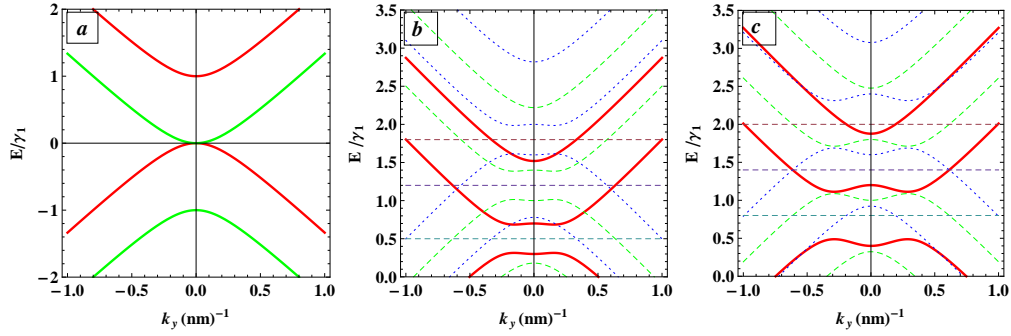


Figure 4.2: Energy spectrum: (a) in region 1 where $V_1 = V_3 = V_5 = 0$. (b) in region 2 for $\delta_2 = 0.2 \gamma_1$, $U_2 = (0.5, 1.2, 1.8) \gamma_1$ (red, dashed green, dotted blue). (c) in region 4 for $\delta_4 = 0.4 \gamma_1$, $U_4 = (0.8, 1.4, 2) \gamma_1$ (red, dashed green, dotted blue). The dashed horizontal lines in (b) and (c) represent the heights of the barriers U_2 and U_4 , respectively.

the first region, there are two right-going (incident) propagating mode and two left-going (reflected) propagating mode. For $\gamma_1 > E > 0$, k_0^+ is real while k_0^- is imaginary, and therefore the propagation is only possible using k_0^+ mode. However when $E > \gamma_1$, both k_0^{\pm} are real and then the propagation

is possible using two modes k_0^+ and k_0^- . In Figure 4.3 we show these different modes and the associated transmission probabilities through double barrier structure. Figure 4.4 presents different cases: (a) asymmetric double barrier

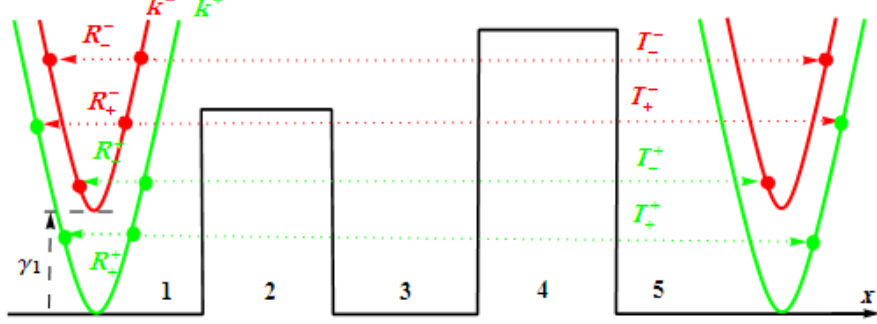


Figure 4.3: Schematic representation of different modes and the associated transmission and reflection probabilities.

structure for $U_2 < U_4$, $\delta_2 = \delta_4$ and (b) symmetric for $U_2 = U_4$, $\delta_2 = \delta_4$. It is interesting to note that the Ben results [134] can be recovered from our results by considering the case (b) by letting $b = c$ in our double barrier. The different channels of transmission and reflection in Figure 4.3 can be mapped into all cases in Figure 4.4 since they are related to the band structure on the both sides of the barriers. However, the effect of the different structure of the two barriers should appear in the transmission and reflection probabilities. The solution of (4.10) can be written as a linear combination of plane waves

$$\phi_{B1}^j = a_1 e^{ik_j^+ x} + a_2 e^{-ik_j^+ x} + a_3 e^{ik_j^- x} + a_4 e^{-ik_j^- x} \quad (4.15)$$

where a_m ($m = 1, 2, 3, 4$) are coefficients of normalization. Substituting (4.15)

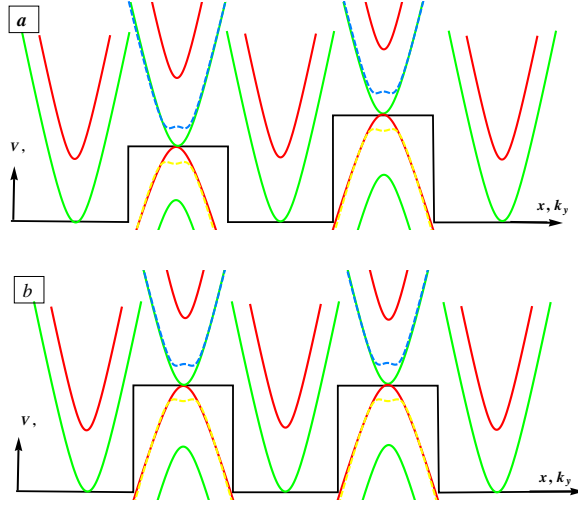


Figure 4.4: Scheme representing the bands inside and outside the barriers for the same interlayer potential difference. (a) asymmetric for $U_2 < U_4$. (b) symmetric for $U_2 = U_4$.

into (4.6 -4.9) we obtain the rest of the spinor components:

$$\phi_{A1}^j = a_1 A_-^+ e^{ik_j^+ x} - a_2 A_+^+ e^{-ik_j^+ x} + a_3 A_-^- e^{ik_j^- x} - a_4 A_+^- e^{-ik_j^- x} \quad (4.16)$$

$$\phi_{A2}^j = a_1 \rho^+ e^{ik_j^+ x} + a_2 \rho^+ e^{-ik_j^+ x} + a_3 \rho^- e^{ik_j^- x} + a_4 \rho^- e^{-ik_j^- x} \quad (4.17)$$

$$\phi_{B2}^j = a_1 \zeta_+^+ e^{ik_j^+ x} - a_2 \zeta_-^+ e^{-ik_j^+ x} + a_3 \zeta_+^- e^{ik_j^- x} - a_4 \zeta_-^- e^{-ik_j^- x} \quad (4.18)$$

where $A_\pm^s = \frac{l(k_j^s \pm ik_y)}{\epsilon_j - \delta_j}$, $\rho^s = (\epsilon_j - \delta_j) \left[1 - \frac{l^2((k_j^s)^2 + k_y^2)}{(\epsilon_j - \delta_j)^2} \right]$ and $\zeta_\pm^s = \frac{\epsilon_j - \delta_j}{\epsilon_j + \delta_j} \rho^s A_\pm^s$.

Now, we can write the general solution

$$\psi^j(x, y) = G_j M_j(x) C_j e^{ik_y y} \quad (4.19)$$

in terms of the matrices

$$\begin{aligned}
G_j &= \begin{pmatrix} A_-^+ & -A_+^+ & A_-^- & -A_+^- \\ 1 & 1 & 1 & 1 \\ \rho^+ & \rho^+ & \rho^- & \rho^- \\ \zeta_+^+ & -\zeta_-^+ & \zeta_+^- & -\zeta_-^- \end{pmatrix}, C_j = \begin{pmatrix} a_1 \\ a_2 \\ a_3 \\ a_4 \end{pmatrix} \\
M_j(x) &= \begin{pmatrix} e^{ik_j^+ x} & 0 & 0 & 0 \\ 0 & e^{-ik_j^+ x} & 0 & 0 \\ 0 & 0 & e^{ik_j^- x} & 0 \\ 0 & 0 & 0 & e^{-ik_j^- x} \end{pmatrix}
\end{aligned} \tag{4.20}$$

Since we are using the transfer matrix, we are interested in the normalization coefficients, the components of C , on the both sides of the double barrier. In other words, we need to specify our spinor in region 1

$$\phi_{A1}^1 = \delta_{s,1} A_-^+ e^{ik_0^+ x} - r_+^s A_+^+ e^{-ik_0^+ x} + \delta_{s,-1} A_-^- e^{ik_0^- x} - r_-^s A_+^- e^{-ik_0^- x} \tag{4.21}$$

$$\phi_{B1}^1 = \delta_{s,1} e^{ik_0^+ x} + r_+^s e^{-ik_0^+ x} + \delta_{s,-1} e^{ik_0^- x} + r_-^s e^{-ik_0^- x} \tag{4.22}$$

$$\phi_{A2}^1 = \delta_{s,1} \rho^+ e^{ik_1^+ x} + r_+^s \rho^+ e^{-ik_0^+ x} + \delta_{s,-1} \rho^- e^{ik_0^- x} + r_-^s \rho^- e^{-ik_0^- x} \tag{4.23}$$

$$\phi_{B2}^1 = \delta_{s,1} \zeta_+^+ e^{ik_0^+ x} - r_+^s \zeta_-^+ e^{-ik_0^+ x} + \delta_{s,-1} \zeta_+^- e^{ik_0^- x} - r_-^s \zeta_-^- e^{-ik_0^- x} \tag{4.24}$$

as well as region 5

$$\phi_{A1}^5 = t_+^s A_-^+ e^{ik_0^+ x} + t_-^s A_-^- e^{ik_0^- x} \quad (4.25)$$

$$\phi_{B1}^5 = t_+^s e^{ik_0^+ x} + t_-^s e^{ik_0^- x} \quad (4.26)$$

$$\phi_{A2}^5 = t_+^s \rho^+ e^{ik_0^+ x} + t_-^s \rho^- e^{ik_0^- x} \quad (4.27)$$

$$\phi_{B2}^5 = t_+^s \zeta_+^+ e^{ik_0^+ x} + t_-^s \zeta_+^- e^{ik_0^- x} \quad (4.28)$$

Since the potential is zero in regions 1, 3 and 5, we have the relation

$$G_1 M_1(x) = G_3 M_3(x) = G_5 M_5(x) \quad (4.29)$$

We will see how the above results will be used to determine different physical quantities. Specifically we focus on the reflection and transmission probabilities as well as related matters.

4.3 Transmission probabilities and conductance

Implementing the appropriate boundary condition in the context of the transfer matrix approach, one can obtain the transmission and reflection probabilities. Continuity of the spinors at the boundaries gives the components of

the vector C which are given by

$$C_1^s = \begin{pmatrix} \delta_{s,1} \\ r_+^s \\ \delta_{s,-1} \\ r_-^s \end{pmatrix}, \quad C_5^s = \begin{pmatrix} t_+^s \\ 0 \\ t_-^s \\ 0 \end{pmatrix} \quad (4.30)$$

where $\delta_{s,\pm 1}$ is the Kronecker delta symbol. The coefficients in the incident and reflected regions can be linked through the transfer matrix M

$$C_1^s = MC_5^s \quad (4.31)$$

which can be obtained explicitly by applying the continuity at the four boundaries of Figure 4.1

$$G_1 M_1(a) C_1 = G_2 M_2(a) C_2 \quad (4.32)$$

$$G_2 M_2(b) C_2 = G_3 M_3(b) C_3 \quad (4.33)$$

$$G_3 M_3(c) C_3 = G_4 M_4(c) C_4 \quad (4.34)$$

$$G_4 M_4(d) C_4 = G_5 M_5(d) C_5 \quad (4.35)$$

Solving these four equations by taking into account of the relation (4.29), we can obtain the transfer matrix M .

Then we can specify the complex coefficients of the transmission t_\pm^s and reflection r_\pm^s using the transfer matrix M . Since we need the transmission T

and reflection R probabilities and because the velocity of the waves scattered through the two different modes is not the same, it is convenient to use the current density \mathbf{J} to obtain the transmission and reflection probabilities.

$$\mathbf{J} = \nu_F \Psi^\dagger \vec{\alpha} \Psi \quad (4.36)$$

to end up with

$$T = \frac{|\mathbf{J}_{\text{tra}}|}{|\mathbf{J}_{\text{inc}}|}, \quad R = \frac{|\mathbf{J}_{\text{ref}}|}{|\mathbf{J}_{\text{inc}}|} \quad (4.37)$$

where $\vec{\alpha}$ is a 4×4 diagonal matrix, on the diagonal 2 Pauli matrices σ_x . From (4.30) and (4.37), we show that the eight transmission and reflection probabilities are given by [135]

$$T_\pm^s = \frac{k_0^\pm}{k_0^s} |t_\pm^s|^2, \quad R_\pm^s = \frac{k_0^\pm}{k_0^s} |r_\pm^s|^2 \quad (4.38)$$

Using the above four transmission probabilities, the conductance can be calculated as a function of the energy. This can be done through the Landauer-Büttiker formula [108] to write the conductance as

$$\mathbf{G}(E) = G_0 \frac{L_y}{2\pi} \int_{-\infty}^{+\infty} dk_y \sum_{s,n=\pm} T_n^s(E, k_y) \quad (4.39)$$

where L_y is the width of the sample in the y -direction and $G_0 = 4 \frac{e^2}{h}$, the factor 4 is due to the valley and spin degeneracy in graphene.

The obtained results will be numerically analyzed to underline our system

behavior. To do this, we will distinguish different cases in terms of the band tunneling.

4.4 Two band tunneling ($E < \gamma_1$)

Let us analyze two interesting cases related to our energy spectrum. Indeed, at low energies ($E < \gamma_1$), we have just one mode of propagation k_0^+ leading to one transmission T and reflection R channel through the two conduction bands touching at zero energy on the both sides of the double barrier. Whereas at higher energy ($E > \gamma_1$), we have two modes of propagation k_0^+ and k_0^- leading to four transmission T_\pm^\pm and reflection R_\pm^\pm channels, through the four conduction bands. Therefore we consider each case separately and underline their relevant properties.

Barbier [33] investigated the transmission and conductance for single and multiple electrostatic barriers with and without interlayer potential difference and for $E < \gamma_1$, however the geometry dependence of the transmission was not done. In this section, we briefly investigate the resonances resulting from the available states in the well between the two barriers and how they influence by the geometry of the system. For a normal incidence and for $\delta_2 = \delta_4 = 0$ the transmission amplitude is shown in Figure 4.5a for different values of the distance Δ between the barriers. The dashed blue curve is for a single barrier with ($\Delta = 0$) and with width ($b_1 + b_2 = 20 \text{ nm}$), we note that

the transmission is zero and there are no resonances in this regime of energy ($E < U_2 = U_4$). Unlike the case of the single barrier, the double barrier structure has resonances in the above mentioned range of energy. These full transmission peaks can be attributed to the bound electron states in the well region between the barriers. In agreement with [136], the number of these resonances depends on the distance between the barriers. Indeed, for $\Delta = 5 \text{ nm}$ we have one peak in the transmission amplitude, increasing the distance allows more bound states to emerge in the well, and for $\Delta = 10 \text{ nm}$ there are two peaks (green and red curves in Figure 4.5, respectively). Figure 4.5b shows the same results in 4.5a but with different height of the two barriers such that $U_2 = 0.4 \gamma_1$ and $U_4 = 0.6 \gamma_1$. We see that the asymmetric structure of the double barrier reduces those resonances resulting from the bound electrons in the well between the two barriers. For $\delta_2 = \delta_4 = 0.2 \gamma_1$, we show the transmission probability by choosing $U_2 = U_4 = 0.4 \gamma_1$ in Figure 4.5c and for $U_2 = 0.4 \gamma_1$, $U_4 = 0.6 \gamma_1$ in Figure 4.5d. For single barrier, there are no resonant peaks inside the induced gap which is not the case for the double barrier as clarified in Figure 4.5c. Figures 4.6a, 4.6c present a comparison of the density plot of the transmission probability as a function of the transverse wave vector k_y of the incident wave and its energy E between different structure of the double barrier with $U_2 = U_4 = 0.4 \gamma_1$ and $U_2 = 0.4 \gamma_1 < U_4 = 0.6 \gamma_1$, respectively, and for $\delta_2 = \delta_4 = 0$ in both. For non-normal incidence in Figure 4.6a ($k_y \neq 0$) we still have a full transmission, even for energies less than the height of the barriers, which are symmetric in k_y . Those resonances are reduced and even disappeared in Figure 4.6c due

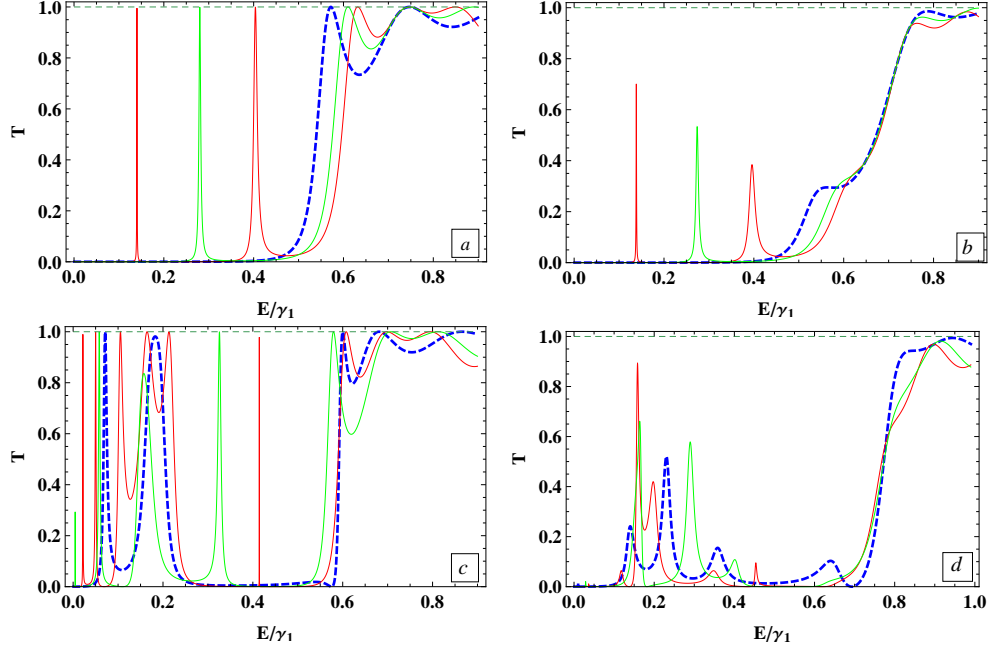


Figure 4.5: Transmission for normal incidence with $b_1 = b_2 = 10 \text{ nm}$, and $\Delta = 0$ (blue dashed), $\Delta = 5 \text{ nm}$ (green), $\Delta = 10 \text{ nm}$ (red). (a) for $U_2 = U_4 = 0.4 \gamma_1$. (b) for $U_2 = 0.4 \gamma_1$ and $U_4 = 0.6 \gamma_1$. (c, d) for the same parameters as in (a, b), respectively, but with $\delta_2 = \delta_4 = 0.2 \gamma_1$.

to the asymmetric structure of the double barrier. In Figures 4.6b, 4.6d we show the density plot of transmission probability, for normal incidence, as a function of Δ and E for the same parameters as in Figure 4.6a and 4.6c, respectively. We note that the number of resonances in Figure 4.6b, due to the bounded electrons in the well between the barriers, increases as long as the distance is increasing. They are very sharp for the low energies and become wider at higher energies. In contrast to Figure 4.6d and as a result of the asymmetric structure of the double barrier these resonances do not exist any more for $E < U_4 = 0.6 \gamma_1$.

It is well-known that introducing an interlayer potential difference induces an

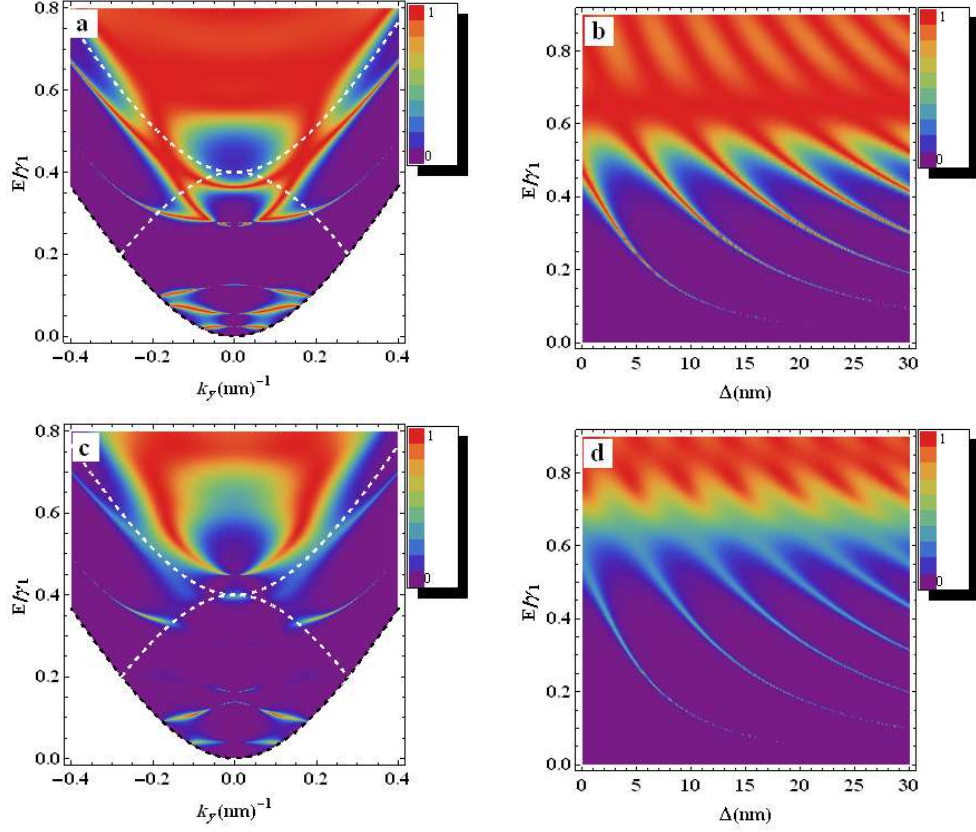


Figure 4.6: Density plot for transmission probability, for $\delta_2 = \delta_4 = 0$, versus: (a) E and ky for $U_2 = U_4 = 0.4 \gamma_1$, and $b_1 = b_2 = \Delta = 10 \text{ nm}$. (b) E and Δ with $ky = 0$ and $b_1 = b_2 = 10 \text{ nm}$. (c) E and ky with $U_2 = 0.4 \gamma_1$, $U_4 = 0.6 \gamma_1$ and $b_1 = b_2 = \Delta = 10 \text{ nm}$. (d) E and Δ with $U_2 = 0.4 \gamma_1$, $U_4 = 0.6 \gamma_1$, $ky = 0$ and $b_1 = b_2 = 10 \text{ nm}$. White and black dashed lines represent the band inside and outside the first barrier, respectively.

energy gap in the energy spectrum in bilayer graphene. It is worth to see how this interlayer potential difference will affect the transmission probability. To do so, we extend the results presented in Figure 4.6 to the case $\delta_2 = \delta_4 = 0.2 \gamma_1$ to get Figure 4.7. In agreement with [33], Figure 4.7a shows a full transmission inside the gap in the energy spectrum, which resulting from the available states in the well between the barriers. In contrast to the single

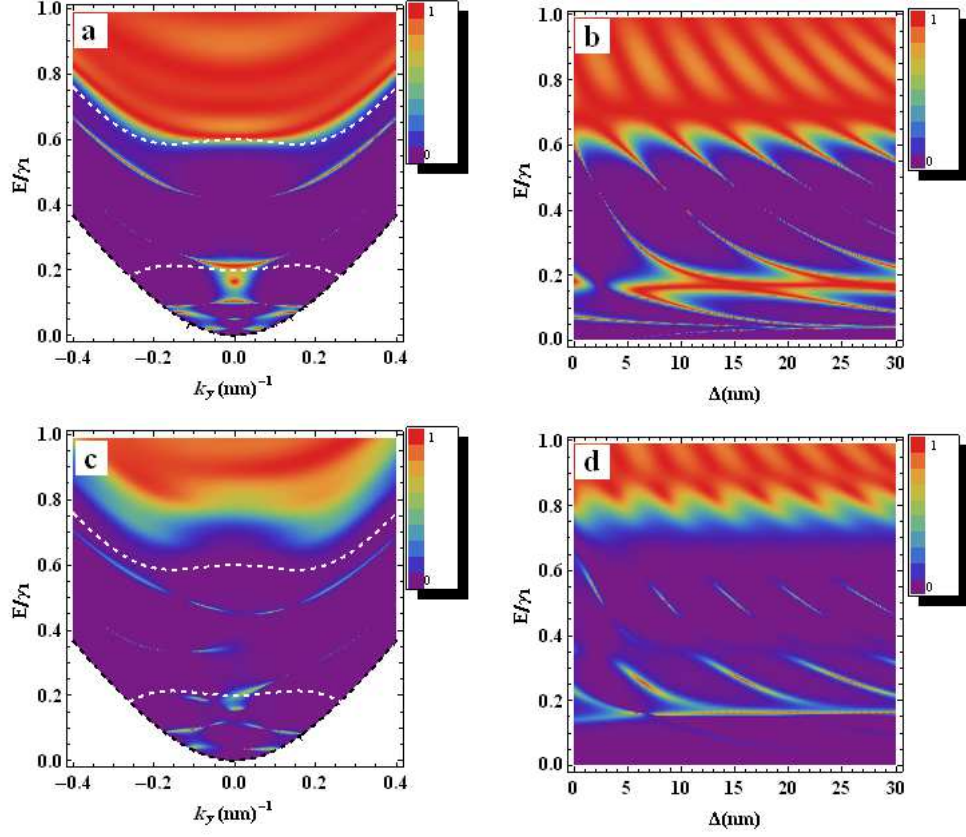


Figure 4.7: Density plot for transmission probability, for $\delta_2 = \delta_4 = 0.2 \gamma_1$, versus: (a) E and k_y for $U_2 = U_4 = 0.4 \gamma_1$, and $b_1 = b_2 = \Delta = 10 \text{ nm}$. (b) E and Δ for the same parameters as in (a) but with $k_y = 0$. (c, d) for the same parameters as in (a, b), respectively, but for $U_2 = 0.4 \gamma_1$, $U_4 = 0.6 \gamma_1$. White and black dashed lines represent the band inside and outside the first barrier, respectively.

barrier case [33, 134], there are full transmission inside the energy gap. In Figure 4.7b, we show the density plot of the transmission probability as a function of E and Δ for fixed thickness of the tow barriers. We note that the resonances resulting from the bound states in the well are highly influenced by the interlayer potential difference where it removes part of them and arises a full transmission at specific value of the energy $E \approx 0.17 \gamma_1$,

which is absent in the case when there is no interlayer potential difference ($\delta_2 = \delta_4 = 0$ in Figure 4.6b). Figures 4.7c,4.7d show the same result as in Figures 4.7a,4.7b, respectively, but with different heights of the barriers $U_2 = 0.4 \gamma_1$ and $U_4 = 0.6 \gamma_1$, which shows a decreasing in the transmission probability as a results of the asymmetric structure of the two barriers.

In Figure 4.8 we observe how these resonances for normal incidence are affected by the parameters of the barriers. In the first row we fixed the thickness of the first barrier $b_1 = 5 \text{ nm}$ and set the height of the two barriers to be the same ($U_2 = U_4 = 0.4 \gamma_1$), then we plot the transmission as a function of Δ and the thickness of the second barrier b_2 as depicted in Figure 4.8a. These resonances occur frequently as Δ increases where b_2 (dashed black line) is equal to b_1 (dashed wight line). Picking up one of these resonances (i.e. at fixed distance between barriers $\Delta = 3.36 \text{ nm}$) and calculating the transmission as a function of b_1 and b_2 as presented in Figure 4.8b, it becomes clear that these resonances occur when ($b_1 = b_2$) for fixed Δ . In the second row, we show the transmission for the same parameters as in the first row but with different heights of the barriers ($U_2 = 0.4 \gamma_1, U_4 = 0.6 \gamma_1$). Full transmission now occur for b_1 (dashed black line) $\neq b_2$ (dashed black line) as shown in Figure 4.8c. It is worth mentioning that for energies less than the strength of the barriers, and for a fixed Δ , full transmission resonances occur always when $S_1 = S_2$, S_1 and S_2 being the areas of the first and second barrier, respectively. Therefore, for fixed b_1 , the value of b_2 where the resonance occur is given by $b_2 = \frac{U_2}{U_4} b_1$ which is superimposed in Figure 4.8b,4.8d

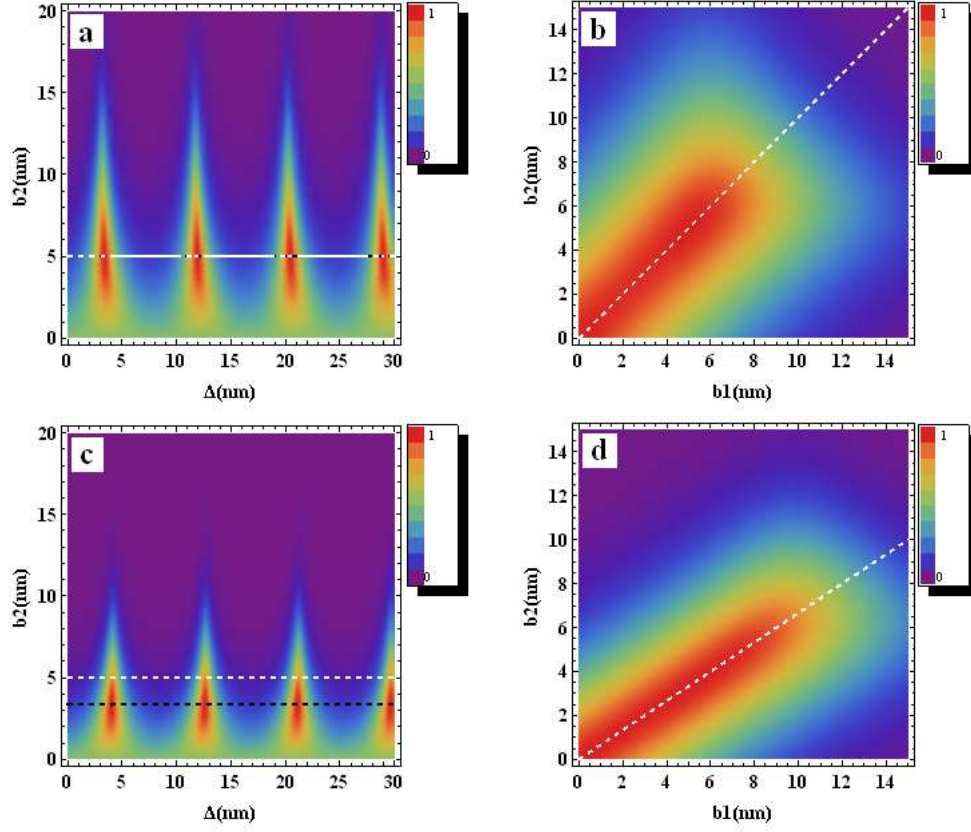


Figure 4.8: Density plot for transmission at normal incidence for $E = \frac{4}{5} U_2$ and $\delta_2 = \delta_4 = 0$. (a) $U_2 = U_4 = 0.4 \gamma_1$, $b_1 = 5 \text{ nm}$. (b) $U_2 = U_4 = 0.4 \gamma_1$, $\Delta = 3.36 \text{ nm}$. (c) $U_2 = 0.4 \gamma_1$, $U_4 = 0.6 \gamma_1$, $b_1 = 5 \text{ nm}$. (d) $U_2 = 0.4 \gamma_1$, $U_4 = 0.6 \gamma_1$, $\Delta = 4 \text{ nm}$. The dashed white and black lines in the left column represent the values of b_1 and b_2 , respectively, where the resonance occur.

(the dashed white line). Moreover, the cloak effect in the double barrier occur at non-normal incidence for some states which is different from the single barrier case [137] that occur always at normal incidence. In Figure 4.4 we extend the results in Figure 4.8 but with interlayer potential difference ($\delta_2 = \delta_4 = 0.1 \gamma_1$) for the same other parameters. As we note the total transmission probability is decreasing and some of the original resonances

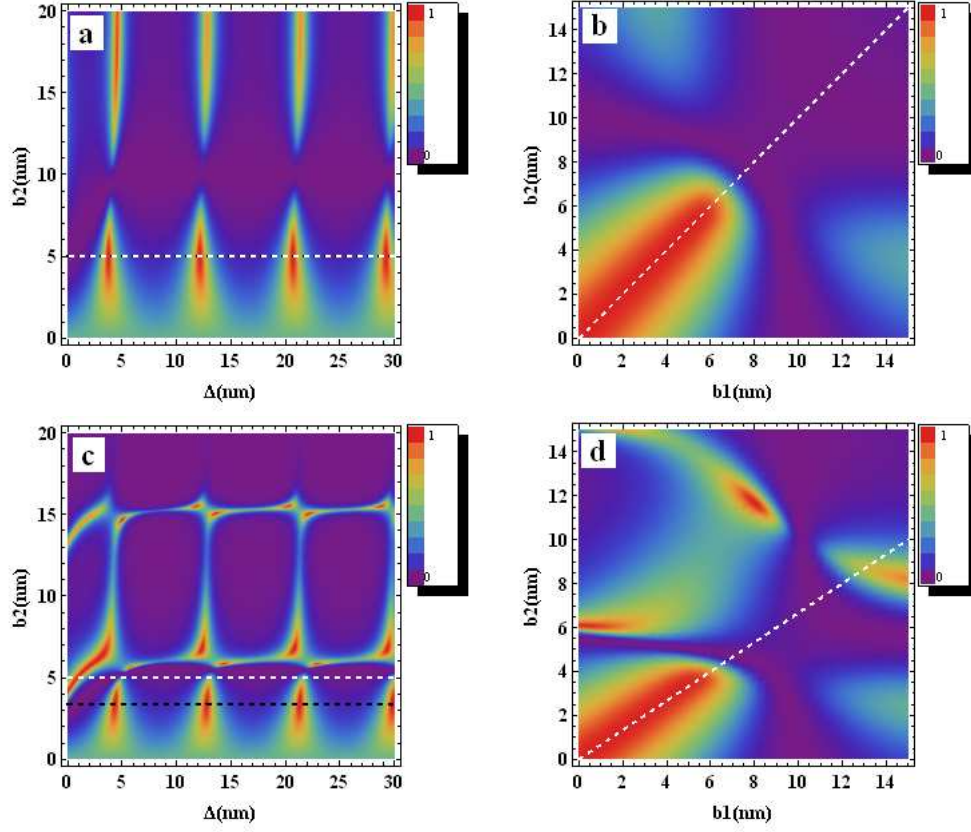


Figure 4.9: Density plot for transmission at normal incidence for $E = \frac{4}{5} U_2$ and $\delta_2 = \delta_4 = 0.1 \gamma_1$. (a) $U_2 = U_4 = 0.4 \gamma_1$, $b_1 = 5 \text{ nm}$. (b) $U_2 = U_4 = 0.4 \gamma_1$, $\Delta = 3.7 \text{ nm}$. (c) $U_2 = 0.4 \gamma_1$, $U_4 = 0.6 \gamma_1$, $b_1 = 5 \text{ nm}$. (d) $U_2 = 0.4 \gamma_1$, $U_4 = 0.6 \gamma_1$, $\Delta = 4.3 \text{ nm}$. The dashed white and black lines in the left column represent the values of b_1 and b_2 , respectively, where the resonance occur.

are splitting as a sequence of the induced energy gap. Let us now see how the transmission probability is affected by the double barrier parameters. In Figures 4.10a, 4.10b we show the density plot of the transmission probability for $U_2 = U_4$, $E < U_2 = U_4$ and different values of Δ , as a function of k_y and the thickness of the two barriers L (i.e. with changing the width of the two barriers simultaneously by setting $b_1 = b_2 = L$). For $\Delta = 10 \text{ nm}$ and

for small L we have a full transmission for wide range of k_y , with increasing L , transmission probability dramatically decreases however, some resonances still show up as depicted in Figure 4.10a. In contrast, for $\Delta = 15 \text{ nm}$ the transmission probability is completely different where the position and number of resonant peaks change as depicted in Figure 4.10b. This stress that the crucial parameters that determine the number of resonant peaks and their position is the width of the well Δ not the thickness of the two barriers b_1 and b_2 [33, 136]. Δ dependence of the transmission probability is shown in Figure 4.10c, we note a full transmission frequently occur for normal incidence. Moreover, after certain value of Δ we start getting a full transmission for specific value of k_y and for all values of Δ . In Figure 4.10d we show how the transmission probability changes with b_2 and k_y for fixed Δ and b_1 . The effect of the interlayer potential difference on the transmission probability with respect to the geometry of the barriers is depicted in Figure 4.11 for the same parameters as in Figure 4.10 but for $\delta_2 = \delta_4 = 0.1 \gamma_1$, we note that most of the resonances disappeared as one can conclude from Figure 4.10 due to the gap in the spectrum resulting from the induced electric field.

4.5 Four band tunneling ($E > \gamma_1$)

For energies larger than γ_1 , the particles can use the two conduction band for propagation which gives rise to four channels of transmission and four for reflection. In Figure 4.12 we present these reflection and transmission

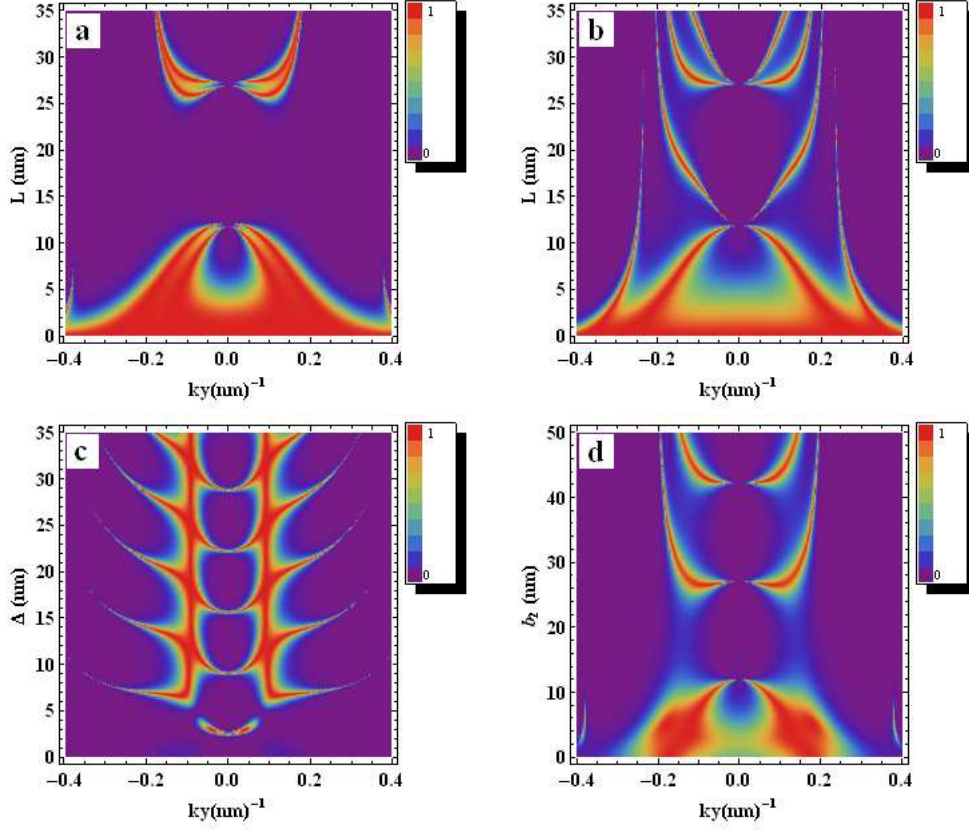


Figure 4.10: Density plot for the transmission probability versus (a, b) k_y and the width of the two barriers ($b_1 = b_2 = L$) for $U_2 = U_4 = 0.6 \gamma_1$, $E = \frac{4}{5} U_4$ and $\Delta = 10 \text{ nm}, 15 \text{ nm}$, respectively. (c) k_y and Δ for the same parameters as in (a) and for $b_1 = b_2 = 10 \text{ nm}$. (d) k_y and b_2 with $b_1 = 5 \text{ nm}$ and $\Delta = 10 \text{ nm}$.

probabilities for a double barrier structure as a function of k_y and E . The potential barriers heights are set to be $U_2 = U_4 = \frac{3}{2} \gamma_1$ and the interlayer potential difference is zero. Different regions are shown up in the spectrum (E, k_y) which appeared as a result of the different propagating modes inside and outside the barriers. The superimposed dashed curves in the density plot in Figure 4.12 indicates the borders between these different regions [134]. In

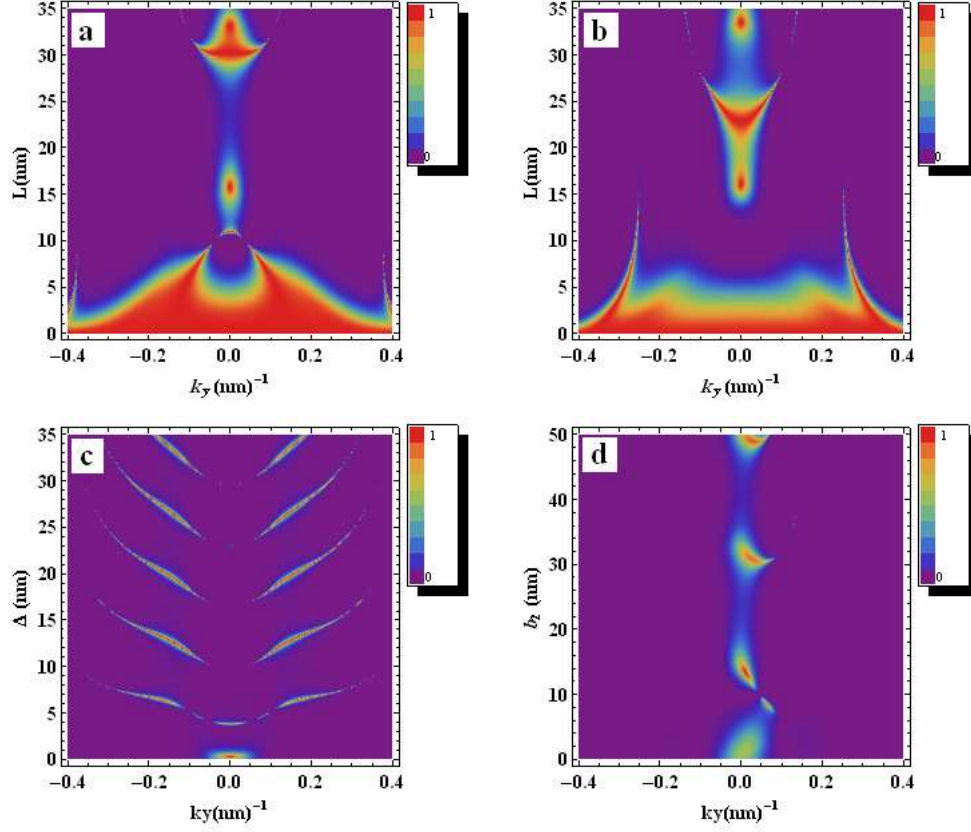


Figure 4.11: Density plot for the transmission probability versus: (a, b) k_y and the width of the two barriers ($b_1 = b_2 = L$) for $U_2 = U_4 = 0.6 \gamma_1$, $E = \frac{4}{5} U_4$, $\delta_2 = \delta_4 = 0.1 \gamma_1$ and $\Delta = 10 \text{ nm}, 15 \text{ nm}$, respectively. (c) k_y and the width of the well Δ for the same parameters as in (a) and for $b_1 = b_2 = 10 \text{ nm}$. (d) k_y and b_2 with $b_1 = 5 \text{ nm}$ and $\Delta = 10 \text{ nm}$.

the double barrier, the cloak effect [137] in T_+^+ and T_-^+ (T_+^-) occurs in the region $U_2 - \gamma_1 < E < U_2$ for nearly normal incidence $k_y \approx 0$ where the two modes k^+ and k^- are decoupled and therefore no scattering occurs between them [134]. However, this effect also exist for some states for non-normal incidence as a result of the available electrons states in the well as mentioned in the previous section. For non-normal incidence the two modes k^+ and

k^- are coupled and hence the electrons can be scattered between them, so that the transmission T_+^+ and T_-^+ (T_+^-) in the same region are not zero for non-normal incidence. For energies less than $U_2 - \gamma_1$ electrons propagate via k^+ mode inside the barriers which give the resonances in T_+^+ in this region. Increasing (decreasing) the area of the barriers or the well between them will increase (decrease) the number of these resonances.

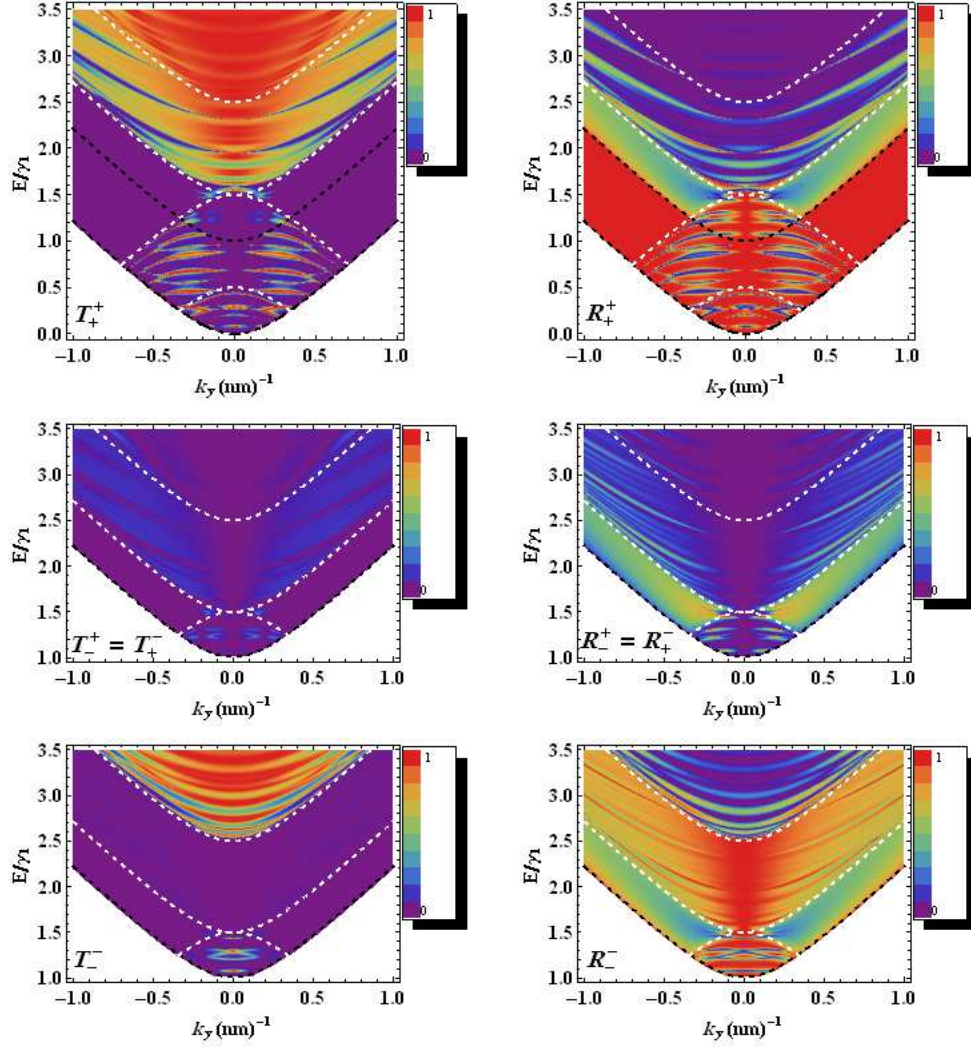


Figure 4.12: Density plot for transmission and reflection probabilities with $U_2 = U_4 = 1.5 \gamma_1$, $b_1 = b_2 = 20 \text{ nm}$ and $\Delta = 10 \text{ nm}$. The dashed white and black lines represent the band inside and outside the barrier, respectively.

For T_-^- electrons propagate via k^- mode which is absent inside the barriers so that the transmission is suppressed in this region and this is equivalent to the cloak effect [134]. The transmission probabilities T_-^+ and T_+^- are the same just when the time reversal symmetry holds (in this case when $\delta_j = 0$, $U_2 = U_4$)

which means that electrons moving in opposite direction (moving from left to right and scattering from $k^+ \rightarrow k^-$ in the vicinity of the first valley or moving from right to left and scattering from $k^- \rightarrow k^+$ in the vicinity of the second valley) are the same because of the valley equivalence [134]. Introducing asymmetric double barrier structure with $U_2 = 1.3 \gamma_1$, $U_4 = 1.5 \gamma_1$ and without interlayer potential difference will break this equivalence symmetry such that $T_-^+ \neq T_+^-$ as depicted in Figure 4.13. In contrast, the reflection probabilities R_-^+ and R_+^- stay the same because the incident electrons return again in an electron states [134]. In addition, the resonant peaks in T_+^+ are less intense comparing to T_+^+ with $U_2 = U_4$ in Figure 4.12. Now let see how the interlayer potential difference will affect the different channels of transmission and reflection. Figure 4.14 reveals the probabilities of the different transmission and reflection channels as a function of k_y and E for $U_2 = U_4 = 1.5 \gamma_1$ and $\delta_2 = \delta_4 = 0.2 \gamma_1$. The general behavior of these different channels resemble the single barrier case [134] with some major differences, such as observing extra resonances in the energy region $0 < E < U_j$ due to these bounded states in the well. In addition, the induced gap does not completely suppressed the transmission in the energy region $U_j \pm \delta_j$ as it the case in the single barrier [134] and this is also attributed to these bounded states. With the interlayer potential difference and different height of the barriers for $U_2 = 1.3 \gamma_1$, $U_4 = 1.5 \gamma_1$ and $\delta_2 = \delta_4 = 0.2 \gamma_1$ we show the different channels of transmission and reflection probabilities in Figure 4.15.

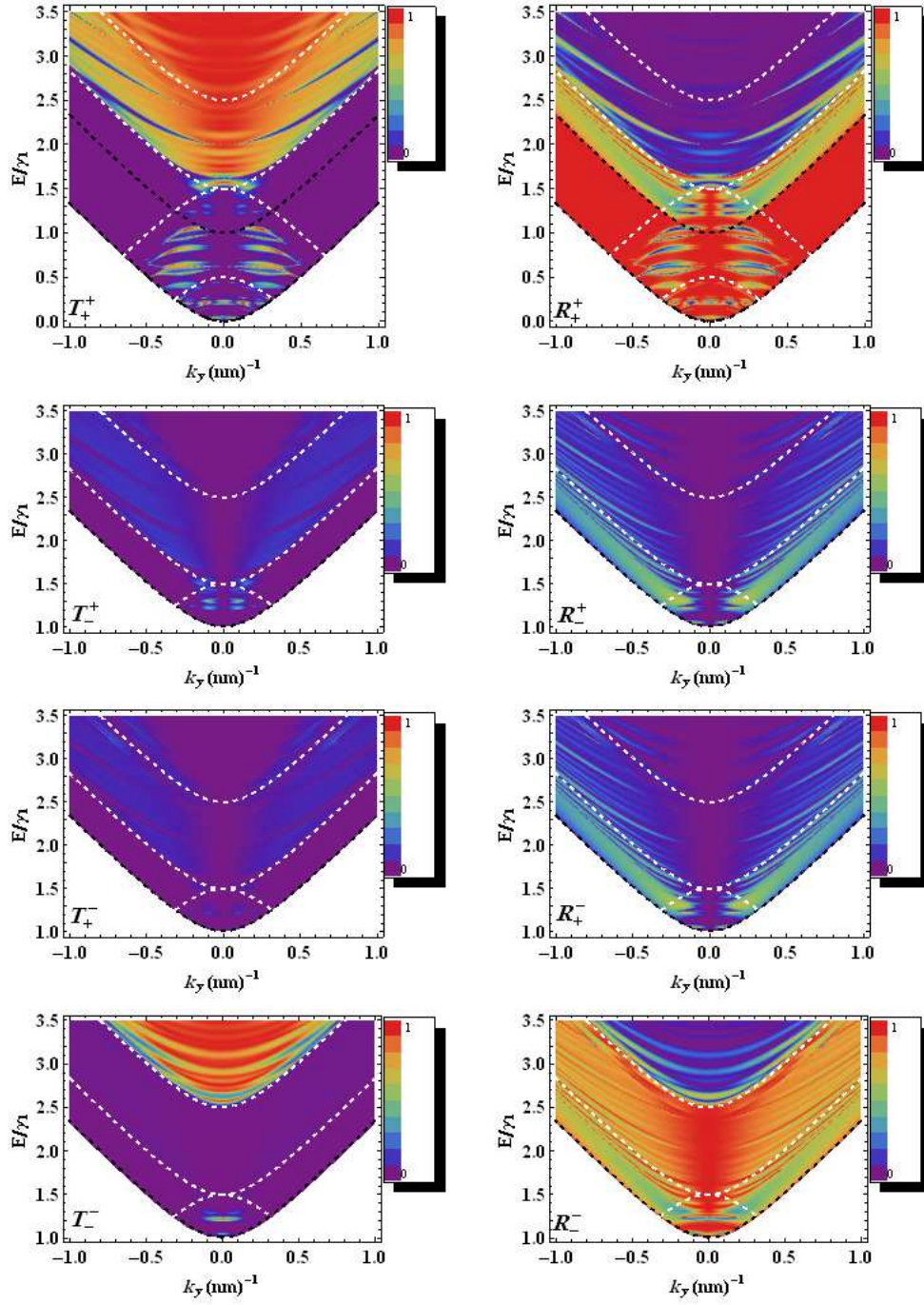


Figure 4.13: Density plot for transmission and reflection probabilities with $U_2 = 1.3 \gamma_1$, $U_4 = 1.5 \gamma_1$, $b_1 = b_2 = 20 \text{ nm}$ and $\Delta = 10 \text{ nm}$. The dashed white and black lines represent the band inside and outside the second barrier, respectively.

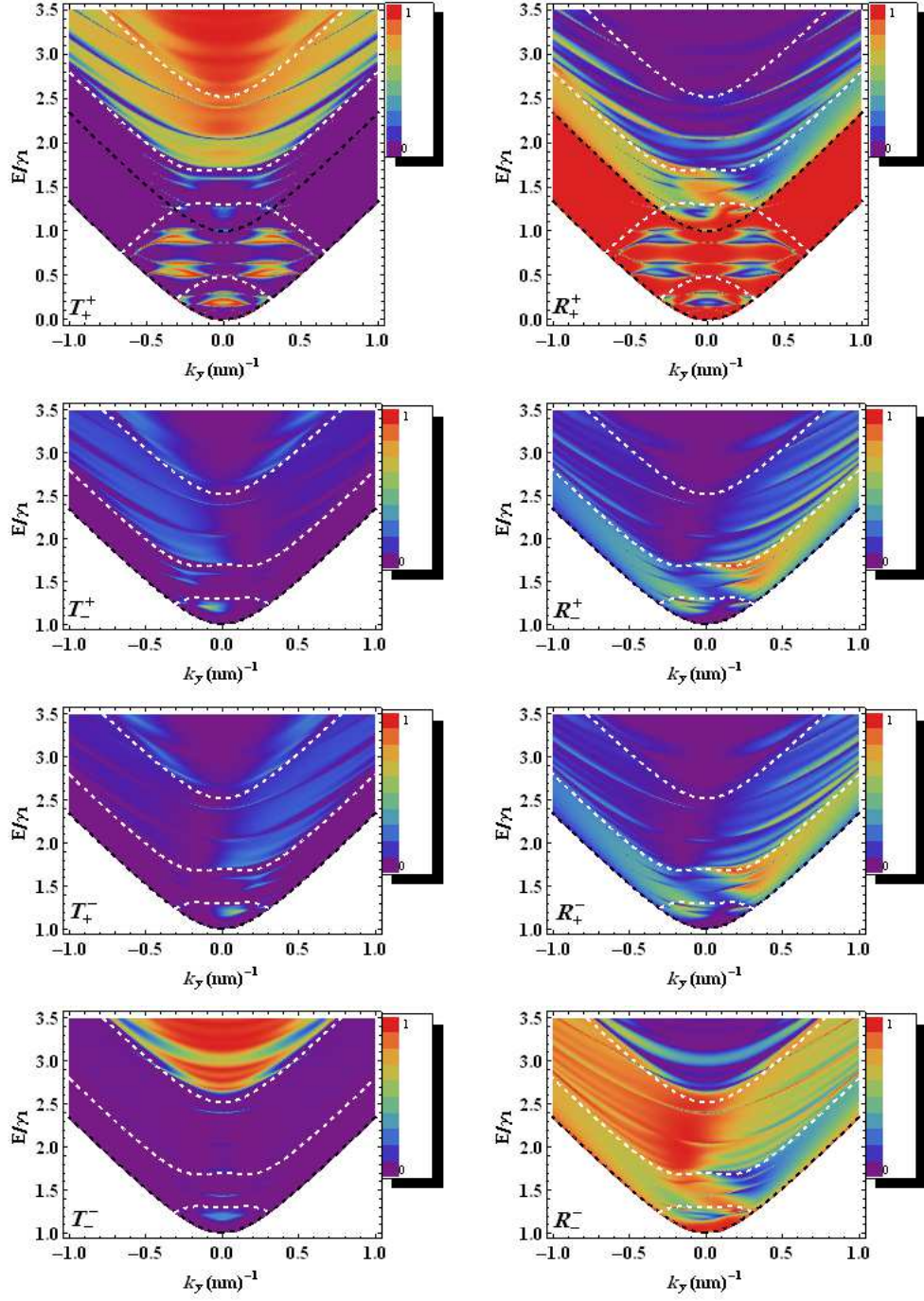


Figure 4.14: Density plot for transmission and reflection probabilities with $U_2 = U_4 = 1.5 \gamma_1$, $\delta_2 = \delta_4 = 0.2 \gamma_1$ and $b_1 = b_2 = \Delta = 10 \text{ nm}$. The dashed white and black lines represent the band inside and outside the second barrier, respectively.

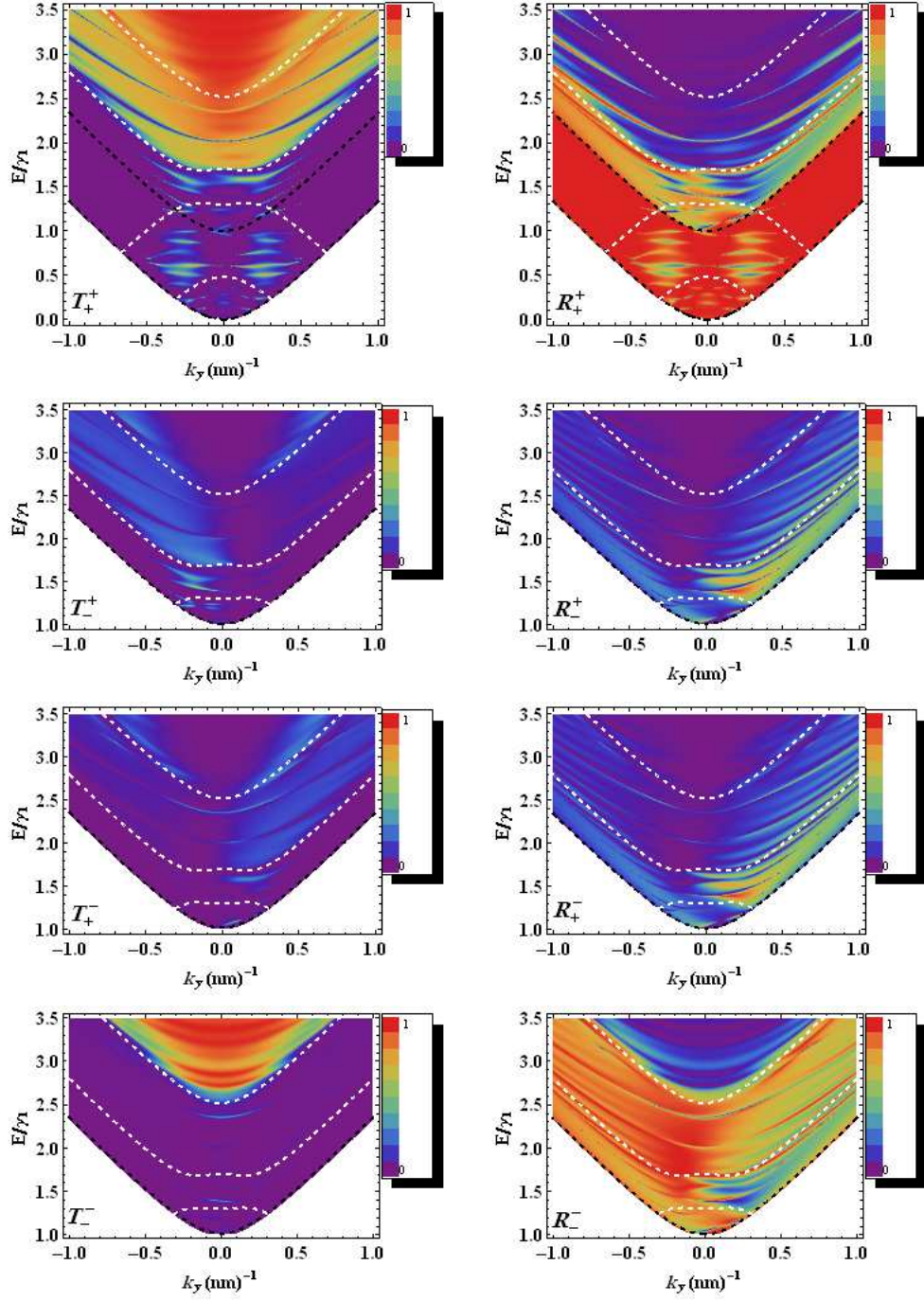


Figure 4.15: Density plot for transmission and reflection probabilities with $U_2 = 1.3 \gamma_1$, $U_4 = 1.5 \gamma_1$, $\delta_2 = \delta_4 = 0.2 \gamma_1$ and $b_1 = b_2 = \Delta = 10 \text{ nm}$. The dashed white and black lines represent the band inside and outside the second barrier, respectively.

In the same manner, the effect of this different height of the barriers is reducing the transmission probabilities. However, we note that it becomes more intense inside the gap and this is because the available states outside the first barrier which are in the same energy zone of the gap on the second barrier.

4.6 Conductance

In Figure 4.16 we show the conductance as a function of the energy E . Figure 4.16a shows the conductance of the double barrier structure for $U_2 = U_4 = 1.5 \gamma_1$, $\delta_2 = \delta_4 = 0$ for $\Delta = 5 \text{ nm}$ (dotted curve) and $\Delta = 10 \text{ nm}$ (solid curve). The peaks in the conductance of the double barrier have extra shoulders as a result of the resonances in the transmission probabilities due to the existence of the bound electron states in the well. These resonances show up as convex curves, which were absent for the single barrier, in T_+^+ in the region $0 < E < U_2 = U_4$ and in T_-^+, T_+^- and T_-^- in the region $\gamma_1 < E < U_2 = U_4$ as depicted in figure 4.12. For energies larger than $U_2 + \gamma_1$ the channel T_-^- is not suppressed (cloaked) any more so that we notice these very pronounced peaks in the conductance in this regime. The inset of Figure 4.16a shows the contribution of each channel to the conductance for $\Delta = 10 \text{ nm}$ in the region $\gamma_1 < E < 2\gamma_1$. For energies between the interlayer coupling and the barriers' height all channels contribute to the conductance, but for energies larger than the barrier's height the contribution of T_-^- is zero due to the cloak

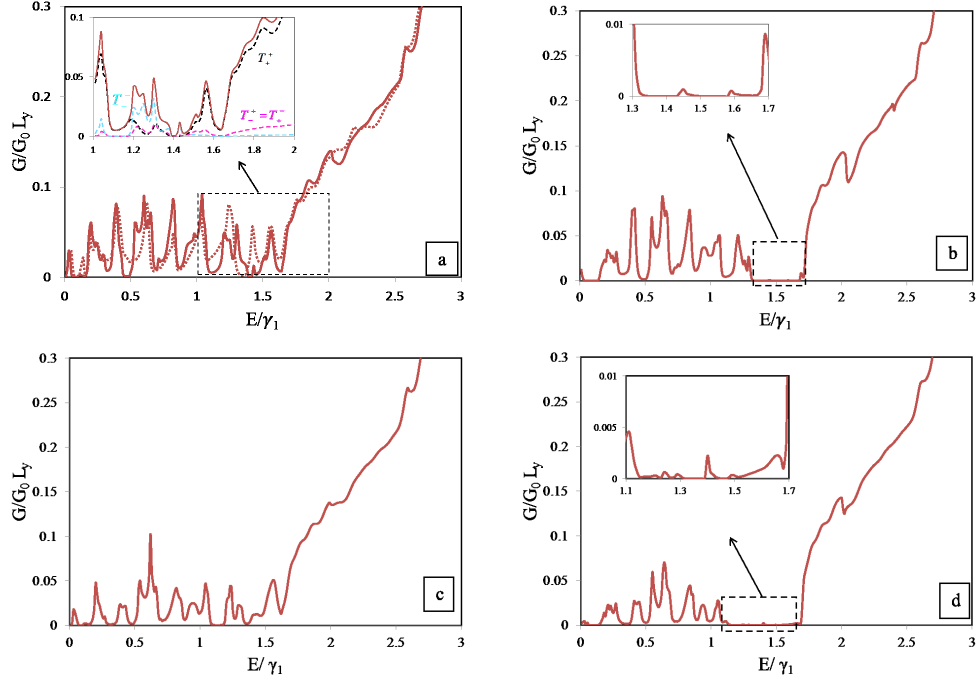


Figure 4.16: Conductance of the double barrier structure as a function of energy for $b_1 = b_2 = 20 \text{ nm}$. (a) $U_2 = U_4 = 1.5 \gamma_1$, $\Delta = 10 \text{ nm}$ (solid), $\Delta = 5 \text{ nm}$ (dotted) and $\delta_2 = \delta_4 = 0$. (b) $U_2 = U_4 = 1.5 \gamma_1$ and $\delta_2 = \delta_4 = 0.2 \gamma_1$. (c) $U_2 = 1.3 \gamma_1$, $U_4 = 1.5 \gamma_1$, $\Delta = 10 \text{ nm}$ and $\delta_2 = \delta_4 = 0$. (d) $U_2 = 1.3 \gamma_1$, $U_4 = 1.5 \gamma_1$, $\Delta = 10 \text{ nm}$ and $\delta_2 = \delta_4 = 0.2 \gamma_1$.

effect which is clarified in the inset of Figure 4.16a. In Figure 4.16b we show the conductance of the double barrier with the interlayer potential difference $\delta_2 = \delta_4 = 0.2 \gamma_1$ and for the same height of the two barriers $U_2 = U_4 = 1.5 \gamma_1$. As a result of the none zero transmission inside the gap (see Figure 4.14) we also have none zero conductance inside the gap as clarified in the inset of Figure 4.16b. In Figure 4.16c we represent the result in Figure 4.16a but with asymmetric double barrier structure such that $U_2 = 1.3 \gamma_1$ and $U_4 = 1.5 \gamma_1$ for $\delta_2 = \delta_4 = 0$, we see that the asymmetric structure of the double barrier

reduces the conductance and even removing some shoulders of the peaks. The effect of the asymmetric double barrier structure together with the interlayer potential difference is presented in Figure 4.16d for $U_2 = 1.3 \gamma_1$, $U_4 = 1.5 \gamma_1$, $\delta_2 = \delta_4 = 0.2 \gamma_1$. Similarly to the previous case, the conductance here also decreases and some of the main peaks are removed as a consequence of this asymmetric structure of the double barriers and the induced gap in the spectrum. Although the interlayer potential difference is the same on the both barriers, the gap in the conductance is not anymore $2 \delta_2 = 2 \delta_4 = 0.4 \gamma_1$ as the case in Figure 4.16c instead it becomes $3 \delta_2 = 3 \delta_4 = 0.6 \gamma_1$ as depicted in the inset of Figure 4.16. Moreover, although at $E = U_2 = U_4 = V$ there are no available states, the conductance is not zero (in the single and double barrier) and this is due to the presence of resonant evanescent modes which are responsible for the pseudo-diffusive transport at the Dirac point [105]. The transmissions coefficients of these evanescent modes are shown in Figure 4.17a,4.17b for a single and double barrier, respectively. At high potential strength ($U_2 = U_4 = V \gg \gamma_1$) and for $\delta_2 = \delta_4 = 0$, the four channels at $E = V$ will give almost identical contributions, $T_+^+ = T_+^- = T_-^+ = T_-^-$, for single and double barrier because the electrons now can not differentiate between the two modes, see Figure 4.17c,4.17d.

The conductance dependence on the double barriers parameters is shown in Figure 4.18. For $E = 1.5 \gamma_1$ and $\delta_2 = \delta_4 = 0$ we show the conductance as a function of the height of the barriers V ($U_2 = U_4 = V$) in Figure 4.18a. In the region $E > V > 0$ the conductance decreases with increasing V , whereas in the

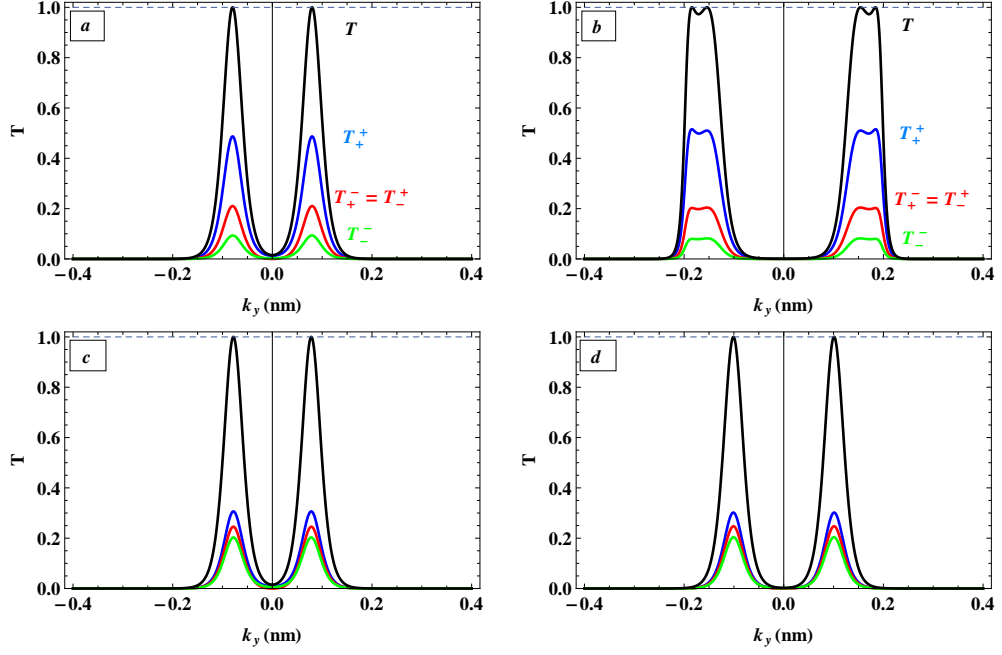


Figure 4.17: The transmissions coefficients around the Dirac point for ($E = V = 1.5 \gamma_1$) and $b_1 = b_2 = 20 \text{ nm}$. (a) single barrier with $\Delta = 0$. (b) double barrier with $\Delta = 10 \text{ nm}$. (c, d) single and double barrier transmission for the same parameters as in (a, b), respectively, but for ($E = V = 5 \gamma_1$). Where $T = \sum_{s,n=\pm} (T_n^s)$

region $V > E$ it increases with increasing V till it reaches a Plato constant value which is an odd behavior. This behavior is attributed to the resonance in the region $E < V$ since the conductance is minimum at the Dirac point (in this case $E = V$) leading to an increase of the conductance on the both sides of the Dirac point ($E > V$ and $E < V$) [105]. In contrast, increasing b_2 for fixed other parameters decreases the conductance as depicted in Figure 4.18b and the number of resonances appearing in the conductance remains the same with increasing b_2 . Finally, in Figure 4.18c we plot the conductance versus Δ . The conductance is seen to oscillate with increasing width of the

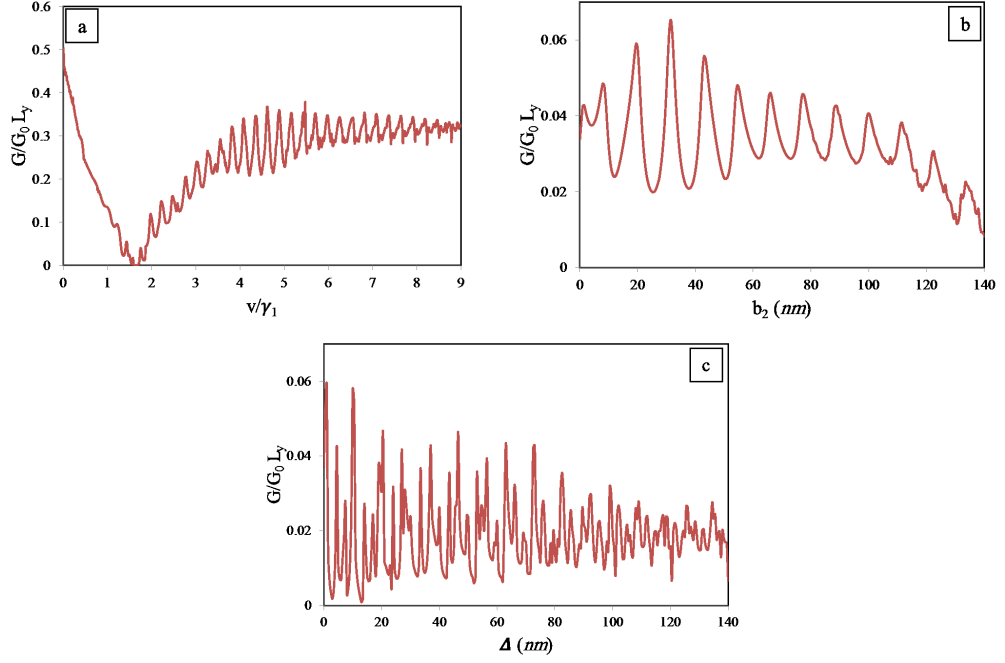


Figure 4.18: The conductance of the double barrier as a function of: (a) barriers's height V ($U_2 = U_4 = V$) for $E = 1.5 \gamma_1$, $b_1 = b_2 = 20 \text{ nm}$ and $\Delta = 10 \text{ nm}$. (b) b_2 for $V = 1.5 \gamma_1$, $E = 1.3 \gamma_1$, $b_1 = 20 \text{ nm}$ and $\Delta = 10 \text{ nm}$. (c) Δ for $V = 1.5 \gamma_1$, $E = 1.3 \gamma_1$ and $b_1 = b_2 = 20 \text{ nm}$.

well and then reaches to a constant asymptotic value.

Chapter 5

CONCLUSION

In conclusion, we have evaluated the reflection and transmission probabilities of electrons through symmetric and asymmetric double barrier potential in a bilayer graphene system. Based on the four band model we found the solution in each potential region and by matching them at the interface of each region and obtained the different transmission and reflection coefficients. Subsequently, the transmission of electrons through symmetric and asymmetric double barrier structure for various barriers parameters was investigated for energy ranges $E < \gamma_1$ and $E > \gamma_1$ where there occurs one and two propagating mode, respectively.

We compared our results with previous work [137] (For $E < \gamma_1$) and showed that the cloak effect may occur for non-normal incidence and exhibits a sequence of the resonances in the transmission in the region $E < V$ due to

bounded electrons in the well between the two barriers. Furthermore, for normal incidence we found that these resonances, which were absent for the single barrier, always occur for fixed energy ($E < U_j$) when $S_1 = S_2$ where S_1, S_2 , that it requires equality of the areas of the first and second barrier. We also found that the most important parameter that control the position and the number of these resonances, in both cases $E < \gamma_1$ or $E > \gamma_1$, is the well width between the tow barriers not the thickness of the barriers in agreement with [33, 136].

Introducing the interlayer potential difference open a gap in the density plot of the transmission probabilities where it is not completely suppressed as it the case in the single barrier [134]. This is a consequence of the bound states in the well between the two barriers. The asymmetric structure of the double potential barrier reduces the transmission probabilities and removes the sharp resonant peaks. We observed that the resulting conductance for the double barrier was different from that of the single barrier. This difference manifests itself through the presence of many extra resonances which are associated with the bound electron states in the well.

The effect of the interlayer potential difference on the transmission probabilities is reflected on the conductance where we obtain a gap with non zero conductance. Moreover, the asymmetric structure of the double barrier reduces the conductance and removes the shoulders of main peaks. Finally, we studied the conductance dependance on the double barrier parameters. The conductance as a function of the height of the barrier showed a region

where it increases with increasing the potential height, this is an odd behavior which can be correlated to the minimum conductance around the Dirac point.

Bibliography

- [1] P. R. Wallace, Phys. Rev. **71**, 622 (1947).
- [2] J. W. McClure, Phys. Rev. **104**, 666671 (1956).
- [3] J. W. McClure, Phys. Rev. **108**, 612 (1957).
- [4] G. W. Semenoff, Phys. Rev. Lett. **53**, 2449 (1984).
- [5] K. S. Novoselov, A. K. Geim, S. V. Morozov, D. Jiang, M. I. Katsnelson, I. V. Grigorieva, S. V. Dubonos, and A. A. Firsov, Nature **438**, 197 (2005).
- [6] Y. Zhang, Y. Tan, H. L. Stormer, and P. Kim, Nature **438**, 201(2005).
- [7] D. P. DiVincenzo, and E. J. Mele, Phys. Rev. B **29**, 1685 (1984).
- [8] F. D. M. Haldane, Phys. Rev. Lett. **61**, 2015 (1988).
- [9] S. Iijima, Nature **354**, 56(1991).
- [10] H. P. Boehm, A. Clauss, U. Hofmann, and G. O. Z. Fischer, Naturforsch. B **17**, 150 (1962).

- [11] A. J. V. Bommel, J. E. Crombeen, and A. V. Tooren, A. V. Surf. Sci. **48**, 463(1975).
- [12] T. Land, T. Michely, R. Behm, J. Hemminger, and G. Comsa, Surf. Sci. **264**, 261(1992).
- [13] H. Itoh, T. Ichinose, C. Oshima, T. Ichinokawa, and T. Aizawa, Surf. Sci. Lett. **254**, L437(1991).
- [14] H. Shioyama, J. Mater. Sci. Lett. **20**, 499(2001).
- [15] K.S. Novoselov, a K. Geim, S. V Morozov, D. Jiang, Y. Zhang, S. V Dubonos, I. V Grigorieva, and a a Firsov, Science **306**, 666 (2004).
- [16] C. Berger, Z. Song, T. Li, X. Li, A. Y. Ogbazghi, R. Feng, Z. Dai, A. N. Marchenkov, E. H. Conrad, P. N. First, and W. A. de Heer, J. Phys. Chem. B **108**, 19912(2004).
- [17] J. C. Meyer, A. K. Geim, M. I. Katsnelson, K. S. Novoselov, T. J. Booth, and S. Roth, Nature (London) **446**, 60 (2007).
- [18] A. K. Geim and K. S. Novoselov, Nature Materials **6**, 183 (2007).
- [19] A.H. Castro Neto, F. Guinea, N.M.R. Peres, K.S. Novoselov, and A.K. Geim, Reviews of Modern Physics **81**, 109 (2009).
- [20] D.S.L. Abergel, V. Apalkov, J. Berashevich, K. Ziegler, and T. Chakraborty, Advances in Physics **59**, 261 (2010).
- [21] N.M.R. Peres, Journal of Physics: Condensed Matter **21**, 323201 (2009).

- [22] A. F. Young, and P. Kim, *Annu. Rev. Condens. Matter Phys.* **2**, 101 (2011).
- [23] D.R. Cooper, B. D’Anjou, N. Ghattamaneni, B. Harack, M. Hilke, A. Horth, N. Majlis, M. Massicotte, L. Vandsburger, E. Whiteway, and V. Yu, *ISRN Condensed Matter Physics* **2012**, 56 (2012).
- [24] C. Lee, X. Wei, J.W. Kysar, and J. Hone, *Science* **321**, 385 (2008).
- [25] O. Leenaerts, B. Partoens, and F.M. Peeters, *Applied Physics Letters* **93**, 193107 (2008).
- [26] K. v. Klitzing, G. Dorda, and M. Pepper, *Phys. Rev. Lett.* **45**, 494 (1980).
- [27] K. S. Novoselov, Z. Jiang, Y. Zhang, S. V. Morozov, H. L. Stormer, U. Zeitler, J. C. Maan, G. S. Boebinger, P. Kim, and A. K. Geim, *Science* **315**, 1379 (2007).
- [28] E. Castro, K. Novoselov, S. Morozov, N. Peres, J. dos Santos, J. Nilsson, F. Guinea, A. Geim, and A. Neto, *Physical Review Letters* **99**, 8 (2007).
- [29] E. McCann, *Physical Review B* **74**, 161403 (2006).
- [30] M.I. Katsnelson, *The European Physical Journal B* **52**, 151 (2006).
- [31] M. Ramezani Masir, P. Vasilopoulos, and F.M. Peeters, *Physical Review B* **82**, 115417 (2010).

- [32] H. Bahlouli, E.B. Choubabi, and A. Jellal, EPL (Europhysics Letters) **95**, 17009 (2011).
- [33] J.M. Pereira, P. Vasilopoulos, and F.M. Peeters, Physical Review B **79**, 155402 (2009).
- [34] M. Barbier, P. Vasilopoulos, and F.M. Peeters, Physical Review B **82**, 235408 (2010).
- [35] M. O. Goerbig, Rev. Mod. Phys. **83**, 1193 (2011).
- [36] H. Boehm, R. Setton, and E. Stumpp, Pure and Applied Chemistry **66**, 1893 (1994).
- [37] R.Z. Khaliullin, H. Eshet, T.D. Khne, J. Behler, and M. Parrinello, Nature Materials **10**, 693 (2011).
- [38] A.C. Neto, N.M. Peres, and F. Guinea, Physics World **19**, 33 (2006).
- [39] N. Savage, Nature **483**, S30 (2012).
- [40] W.A. De Heer, C. Berger, M. Ruan, M. Sprinkle, X. Li, Y. Hu, and B. Zhang, PNAS **108**, 16900 (2011).
- [41] G. Eda, G. Fanchini, and M. Chhowalla, Nat. Nanotechnol **3**, 270 (2008)
- [42] A. Reina, X. Jia, J. Ho, D. Nezich, H. Son, V. Bulovic, M.S. Dresselhaus, and J. Kong, Nano Letters **9**, 30 (2009).
- [43] K.S. Kim, Y. Zhao, H. Jang, S.Y. Lee, J.M. Kim, K.S. Kim, J.-H. Ahn, P. Kim, J.-Y. Choi, and B.H. Hong, Nature **457**, 706 (2009).

- [44] L. Gao, W. Ren, H. Xu, L. Jin, Z. Wang, T. Ma, L.-P. Ma, Z. Zhang, Q. Fu, L.-M. Peng, X. Bao, and H.-M. Cheng, *Nature Communications* **3**, 699 (2012).
- [45] M. Temmen, O. Ochedowski, B.K. Bussmann, M. Schleberger, M. Reichling, and T.R.J. Bollmann, *Beilstein Journal of Nanotechnology* **4**, 625 (2013).
- [46] A.K. Geim and A.H. Macdonald, *Physics Today* **60**, 35 (2007).
- [47] 1 X. Li, C.W. Magnuson, A. Venugopal, R.M. Tromp, J.B. Hannon, E.M. Vogel, L. Colombo, and R.S. Ruoff, *Journal of the American Chemical Society* **133**, 1816 (2011).
- [48] 1 X. Li, W. Cai, J. An, S. Kim, J. Nah, D. Yang, R. Piner, A. Velamakanni, I. Jung, E. Tutuc, S.K. Banerjee, L. Colombo, and R.S. Ruoff, *Science* **324**, 1312 (2009).
- [49] W. Wu, Q. Yu, P. Peng, Z. Liu, J. Bao, and S.-S. Pei, *Nanotechnology* **23**, 035603 (2012).
- [50] H. Kim, I. Songe, C. Park, M. Son, M. Hong, Y. Kim, J.S. Kim, H.-J. Shin, J. Baik, and H.C. Choi, *ACS Nano* **7**, 6575 (2013).
- [51] S. Bae, H. Kim, Y. Lee, X. Xu, J.-S. Park, Y. Zheng, J. Balakrishnan, T. Lei, H.R. Kim, Y. Il Song, Y.-J. Kim, K.S. Kim, B. Ozyilmaz, J.-H. Ahn, B.H. Hong, and S. Iijima, *Nature Nanotechnology* **5**, 574 (2010).

- [52] T.O. Wehling, K.S. Novoselov, S. V Morozov, E.E. Vdovin, M.I. Katsnelson, a K. Geim, and a I. Lichtenstein, Nano Letters **8**, 173 (2008).
- [53] F. Schedin, A. K. Geim, S. V. Morozov, E. W. Hill, P. Blake, M. I. Katsnelson, and K. S. Novoselov, Nature Materials **6**, 652 (2007).
- [54] I. Iezhokin, P. Offermans, S.H. Brongersma, A. J.M. Giesbers, and C.F.J. Flipse, Applied Physics Letters **103**, 053514 (2013).
- [55] S. Mirsky, Scientific American Magazine **305**, 74 (2011).
- [56] F. Bonaccorso, Z. Sun, T. Hasan, and A. C. Ferrari, Nature Photonics **4**, 611 (2010).
- [57] Bullen P and Isele R 2008 German flat panel display forum (DFF) *European Technology: Flat Panel Displays* 6th edn (Germany: VDMA)
- [58] G. Jo, M. Choe, S. Lee, W. Park, Y.H. Kahng, and T. Lee, Nanotechnology **23**, 112001 (2012).
- [59] Y. Wu, Y. Lin, A. a Bol, K. a Jenkins, F. Xia, D.B. Farmer, Y. Zhu, and P. Avouris, Nature **472**, 74 (2011).
- [60] F.Schwierz, Nature Nanotechnology **5**, 487 (2010).
- [61] Y. Lin, C. Dimitrakopoulos, K.A. Jenkins, D.B. Farmer, H. Chiu, A. Grill, and P. Avouris, Science **327**, 662 (2010).

- [62] L. Britnell, R. V Gorbachev, a K. Geim, L. a Ponomarenko, a Mishchenko, M.T. Greenaway, T.M. Fromhold, K.S. Novoselov, and L. Eaves, *Nature Communications* **4**, 1794 (2013).
- [63] W.S. Hwang, P. Zhao, K. Tahy, L.O. Nyakiti, V.D. Wheeler, C.R.E. Jr, D.K. Gaskill, J.A. Robinson, W. Haensch, H.G. Xing, A. Seabaugh, and D. Jena, *arXiv:1310.6823 [cond-mat.mes-hall]* (2013).
- [64] D. Xu, H. Liu, V. Sacksteder, J. Song, H. Jiang, Q. Sun, and X.C. Xie, *Journal of Physics: Condensed Matter Condensed Matter* **25**, 105303 (2013).
- [65] H. Wang, D. Nezich, J. Kong, and T. Palacios, *IEEE Electron Device Letters* **30**, 547 (2009).
- [66] L. Liao, Y.-C. Lin, M. Bao, R. Cheng, J. Bai, Y. Liu, Y. Qu, K.L. Wang, Y. Huang, and X. Duan, *Nature* **467**, 305 (2010).
- [67] L. Liao, J. Bai, R. Cheng, H. Zhou, L. Liu, Y. Liu, and Y. Huang, *Nano Letters* **12**, 2653 (2011).
- [68] M. Barbier, PhD thesis, UNIVERSITEIT ANTWERPEN (2012)
- [69] S. Reich, J. Maultzsch, and C. Thomsen, *Physical Review B* **66**, 035412 (2002).
- [70] C. Bena and G. Montambaux, *New Journal of Physics* **11**, 095003 (2009).

- [71] B. Partoens and F. Peeters, Physical Review B **74**, 075404 (2006).
- [72] M. Jammer, Concepts of Mass in Contemporary Physics and Philosophy (Princeton University Press, 2000).
- [73] K. Seeger, Semiconductor Physics (Springer-Verlag, 1985).
- [74] C. Kittel, Introduction to Solid State Physics (Wiley, 2nd ed., 1986).
- [75] W. Zawadzki and P. Pfeffer, Semicond. Sci. Technol **5**, 179 (1990).
- [76] V. Ariel, A. Fraenkel, E. Finkman, J. Appl. Phys. **71**, 4382 (1992).
- [77] V. Ariel, and A. Natan, (ICEAA), 696 (2013)
- [78] M.I. Katsnelson, K.S. Novoselov, and a. K. Geim, Nature Physics **2**, 620 (2006).
- [79] J.D. Bernal, Proceedings of the Royal Society A: Mathematical, Physical and Engineering Sciences **106**, 749 (1924).
- [80] T. Taychatanapat, K. Watanabe, T. Taniguchi, and P. Jarillo-Herrero, Nature Physics **7**, 621 (2011).
- [81] D. D. L. Chung, J. Mater. Sci. **37**, 1 (2002).
- [82] L. Zhang, Z. Li, D. Basov, M. Fogler, Z. Hao, and M. Martin, Physical Review B **78**, 235408 (2008).
- [83] 1 L.M. Malard, J. Nilsson, D.C. Elias, J.C. Brant, F. Plentz, E.S. Alves, A. H. Castro Neto, and M. A. Pimenta, Physical Review B **76**, 201401(R)(2007).

- [84] M. Freitag, *Nature Physics* **7**, 596 (2011).
- [85] M. Mucha-Kruczyński, *Theory of Bilayer Graphene Spectroscopy* (Springer Berlin Heidelberg, Berlin, Heidelberg, 2013), p. 09.
- [86] J. Nilsson, a. Castro Neto, F. Guinea, and N. Peres, *Physical Review B* **78**, 045405 (2008).
- [87] A.H.C. Neto and N.M.R. Peres, *Physical Review B* **73**, 245426 (2006).
- [88] E. McCann and V. Fal'ko, *Physical Review Letters* **96**, 086805 (2006).
- [89] M. Mucha-Kruczyński, E. McCann, and V.I. Fal'ko, *Semiconductor Science and Technology* **25**, 033001 (2010).
- [90] J. Mañes, F. Guinea, and M. Vozmediano, *Physical Review B* **75**, 155424 (2007).
- [91] E. McCann, D.S.L. Abergel, and V.I. Fal'ko, *Solid State Communications* **143**, 110 (2007).
- [92] J. Cserti, A. Csordás, and G. Dávid, *Physical Review Letters* **99**, 066802 (2007).
- [93] M. Koshino and E. McCann, *Physical Review B* **80**, 165409 (2009).
- [94] B. Wang, C. Zhang, and Z. Ma, *Journal of Physics. Condensed Matter : an Institute of Physics Journal* **24**, 485303 (2012).
- [95] C.-S. Park, *Solid State Communications* **152**, 2018 (2012).

- [96] E. Jung, D. Park, and C.-S. Park, Physical Review B **87**, 115438 (2013).
- [97] T. Ohta, A. Bostwick, T. Seyller, K. Horn, and E. Rotenberg, Science **313**, 951 (2006).
- [98] E. Fradkin, Phys. Rev. B **33**, 3263 (1986).
- [99] K. Ziegler, Phys. Rev. Lett. **80**, 3113 (1998).
- [100] E. V. Gorbar, V. P. Gusynin, V. A. Miransky, and I. A. Shovkovy, Phys. Rev. B **66**, 045108 (2002).
- [101] J. Tworzydło, B. Trauzettel, M. Titov, A. Rycerz, and C. W. J. Beenakker, Phys. Rev. Lett. **96**, 246802 (2006).
- [102] P. M. Ostrovsky, I. V. Gornyi, and A. D. Mirlin, Phys. Rev. B **74**, 235443 (2006).
- [103] M. I. Katsnelson, The European Physical Journal B **57**, 225 (2007).
- [104] J. H. Chen, C. Jang, S. Xiao, M. Ishigami, and M. S. Fuhrer, Nature Nanotechnology **3**, 206 (2008).
- [105] I. Snyman and C. Beenakker, Physical Review B **75**, 045322 (2007).
- [106] R. Danneau, F. Wu, M.F. Craciun, S. Russo, M.Y. Tomi, J. Salmilehto, a. F. Morpurgo, and P.J. Hakonen, Journal of Low Temperature Physics **153**, 374 (2008).

- [107] R. Danneau, F. Wu, M.F. Craciun, S. Russo, M.Y. Tomi, J. Salmilehto, A.F. Morpurgo, and P.J. Hakonen, Solid State Communications 149, 1050 (2009).
- [108] Ya. M. Blanter and M. Büttiker, Physics Reports **336**, (2000).
- [109] C. Beenakker, Reviews of Modern Physics **80**, 1337 (2008).
- [110] L. DiCarlo, J. Williams, Y. Zhang, D. McClure, and C. Marcus, Physical Review Letters **100**, 156801 (2008).
- [111] M.F. Borunda, H. Hennig, and E.J. Heller, Physical Review B **88**, 125415 (2013).
- [112] M.V. Berry, R.J. Mondragon, Proc. R. Soc. Lond. **A 412**, 53 (1987)
- [113] E. Sonin, Physical Review B **79**, 195438 (2009).
- [114] S.V. Kryuchkov, Journal of Modern Physics **03**, 994 (2012).
- [115] L. Britnell, R. V Gorbachev, a K. Geim, L. a Ponomarenko, a Mishchenko, M.T. Greenaway, T.M. Fromhold, K.S. Novoselov, and L. Eaves, Nature Communications **4**, 1794 (2013).
- [116] A.J. Pearce, F. Cavaliere, and E. Mariani, Journal of Physics. Condensed Matter **25**, 375301 (2013).
- [117] H. Brody, Nature (London) 483, S29 (2012).
- [118] O. Klein, Zeitschrift für Physik 53, 157 (1929).

- [119] S.Y. Zhou, D.A. Siegel, A.V. Fedorov, F. El Gabaly, A.K. Schmid, A.H. Castro Neto and A. Lanzara, *Nature Materials* 7, 259 (2007).
- [120] R. Costa Filho, G. Farias, and F. Peeters, *Physical Review B* 76, 193409 (2007).
- [121] Y. Zhang, T.-T. Tang, C. Girit, Z. Hao, M.C. Martin, A. Zettl, M.F. Crommie, Y.R. Shen, and F. Wang, *Nature* 459, 820 (2009).
- [122] S.B. Trickey, F. Mller-Plathe, and G.H.F. Diercksen, *Physical Review B* 45, 4460 (1992).
- [123] E. McCann, D.S.L. Abergel, and V.I. Fal'ko, *The European Physical Journal Special Topics* 148, 91 (2007).
- [124] Z. Li, E. Henriksen, Z. Jiang, Z. Hao, M. Martin, P. Kim, H. Stormer, and D. Basov, *Physical Review Letters* 102, 16 (2009).
- [125] M. Koshino, *New Journal of Physics* 11, 095010 (2009).
- [126] M. Killi, S. Wu, and A. Paramekanti, *Physical Review Letters* 107, 2 (2011).
- [127] S. Das Sarma, S. Adam, E. Hwang, and E. Rossi, *Reviews of Modern Physics* 83, 407 (2011).
- [128] A. Lherbier, S.M.-M. Dubois, X. Declerck, Y.-M. Niquet, S. Roche, and J.-C. Charlier, *Physical Review B* 86, 075402 (2012).

- [129] E. McCann and M. Koshino, Reports on Progress in Physics. Physical Society (Great Britain) 76, 056503 (2013).
- [130] H. Bahlouli, E.B. Choubabi, A. Jellal, and M. Mekkaoui, Journal of Low Temperature Physics 169, 51 (2012).
- [131] A. Jellal, E.B. Choubabi, H. Bahlouli, and A. Aljaafari, Journal of Low Temperature Physics 168, 40 (2012).
- [132] A. El Mouhafid and A. Jellal, Journal of Low Temperature Physics 173, 264 (2013).
- [133] T. Tudorovskiy, K.J. A. Reijnders, and M.I. Katsnelson, Physica Scripta T146, 014010 (2012).
- [134] B. Van Duppen and F.M. Peeters, Physical Review B 87, 205427 (2013).
- [135] B. Van Duppen, S.H.R. Sena, and F.M. Peeters, Physical Review B 87, 195439 (2013).
- [136] C. Bai, and X. Zhang, Physical Review B 76, 075430 (2007).
- [137] N. Gu, M. Rudner, and L. Levitov, Physical Review Letters 107, 156603 (2011).

Vitae



Personal Information

Name: **Hasan Mohammed Hasan Abdullah**
Born: May 6, 1984, Taiz, Yemen
Contact: Phys. Dept., Taiz University, Yemen
Email Address: alshehab211@yahoo.com

Education

Jun- 2014: Master in physics, KFUPM, Saudi Arabia
2003-2007: B.S. Physics, Taiz University, Yemen.

Training and Experience

Jun-2013: International Summer School on bilayer Graphene, Chouaib Doukkali University, El jadida, Morocco
Jun-2012: International Summer School on Graphene, Chouaib Doukkali University, El jadida, Morocco
Nov 2008 –Jul 2010: Instructor in Physics Dept., Faculty of Science, Taiz University, Yemen.
Aug 2007- May 2008: Training course in Electric Department, Swedish Vocational Training Center, Taiz, Yemen
Jun- 2006: Training course in experimental physics, Damascus University, Damascus, Syria

Publication

1. **Hasan M. Abdullah**, Hocine Bahlouli, Abderrahim El Mouhafid, Ahmed Jellal,” Band Tunnelling Through Double Barrier in Bilayer Graphene”, [arXiv:1401.5427v1](https://arxiv.org/abs/1401.5427v1) [cond-mat.mes-hall], 2014.